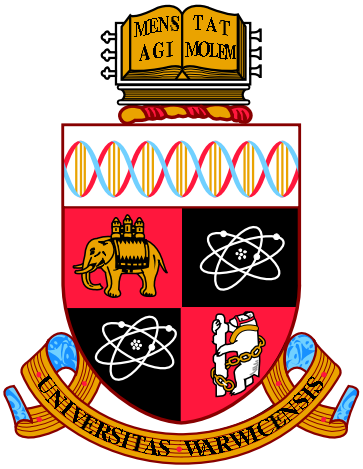

Spatial and temporal analysis of sunspot oscillations

by

Nicky D. Y. Chorley

Thesis

Submitted to the University of Warwick

for the degree of

Doctor of Philosophy

Department of Physics

June 2011

THE UNIVERSITY OF WARWICK

Contents

List of tables

List of figures

Acknowledgments

I would like to thank my supervisor, Dr. Bogdan Hnat for all his support and guidance throughout the last 3.5 years. I am also grateful to Prof. Valery Nakariakov for allowing me the chance to work on solar oscillations. Thanks also go to Andy Inglis for various discussions, both scientific and otherwise. I have also benefited from the other staff and students in CFSA. Warwick University Chess Club provided a much needed distraction from writing up. Finally, thanks to my family and to Megan, for their support and encouragement.

This thesis was typeset with LaTeX 2$_\varepsilon$[1] by the author.

[1] LaTeX 2$_\varepsilon$ is an extension of LaTeX. LaTeX is a collection of macros for TeX. TeX is a trademark of the American Mathematical Society. The style package *warwickthesis* was used.

Declarations

I declare that the work presented in this thesis is my own, except where indicated. I also confirm that this thesis has not been submitted for a degree at another university. Work presented in this thesis has been published in the following peer-reviewed journal articles:

N. Chorley, B. Hnat, V. M. Nakariakov, A. R. Inglis & I. A. Bakunina 2010, *Long period oscillations in sunspots*, A&A, **513**, A27

- A. R. Inglis provided help with EMD, as well as the code to perform it.
- I. A. Bakunina contributed useful discussions.

N. Chorley, C. Foullon, B. Hnat, V. M. Nakariakov & K. Shibasaki 2011, *Period persistence of long period oscillations in sunspots*, A&A, **529**, A123

- C. Foullon was a source of ideas for this work, as well as providing help with access to GOES data and catalogues.
- K. Shibasaki contributed useful discussions.

Abstract

Sunspots are the most conspicuous feature seen on the solar photosphere and are manifestations of the solar magnetic field. Their study, then, may provide us with a greater understanding of the dynamo mechanism thought to be responsible for the generation of this field.

In this thesis, the oscillations of sunspots are studied by making use of observational data from two instruments: the Nobeyama Radioheliograph (NoRH) and the Solar Optical Telescope (SOT) on board the Hinode spacecraft.

First, a study of long period oscillations was undertaken in which two long period peaks ($P > 10$ min) were identified in the power spectra of time series generated from sets of images of 3 sunspots observed with NoRH. In addition, by using the techniques of period, power, correlation and lag mapping, it was found that the power in each of these peaks was concentrated over the umbral regions and that there were two regions of approximately equal size oscillating in anti-phase with each other. It was suggested that these properties could be signatures of a "shallow" sunspot.

A follow-up study was then performed, in which the lifetimes of the long period oscillations were investigated over a period of 9 days. These oscillations were seen to dominate the spectra during this interval and the periods and amplitudes were stable during that time. A simple model of a damped, driven simple harmonic oscillator (in which the driving term was nonlinear) was proposed to explain the generation and support of the oscillations.

Finally, a study of the spatial properties of the 3 minute oscillations was performed by applying the mapping techniques mentioned above to Hinode/SOT data. The distributions of power and lag of maximum correlation coefficient were found to be non-uniform over the sunspots under study and this may be indicative of inhomogeneities of the physical quantities in the structures.

Chapter 1

Introduction

1.1 Basic plasma physics

A plasma is a collection of ions and electrons and since the particles are charged, they are sources of electric fields and can therefore affect the dynamics of other particles. In addition, when particles of opposite charge move with respect to each other, they generate currents, which in turn generate magnetic fields, again changing the particle dynamics.

As an example of such behaviour, one can consider displacing some amount of electrons in a cold plasma, in which all particles initially have no thermal motion and are therefore at rest. The separation between the ions and electrons generates an electric field that acts as a restoring force on the electrons. Since the ions are much heavier than the electrons, they can be treated as fixed. The electrons accelerate towards the equilibrium position and are carried past it by their momentum. Once past the equilibrium position, the electrons feel a decelerating force, since the electric field is now in the opposite direction. The electrons then undergo simple harmonic motion with a frequency known as the plasma frequency, which is given by

$$\omega_{pe} = \left(\frac{n_e e^2}{\varepsilon_0 m} \right)^{\frac{1}{2}}, \tag{1.1}$$

where e is the charge on an electron, ε_0 is the permittivity of free space, m is the electron mass and n_e is the electron number density.

Another important concept in plasma physics is the idea of the Debye length. Again, we consider a cold plasma and now insert a positive point charge. The

electrons are attracted towards the point charge, while the ions are repelled. The electrons surround the point charge and therefore screen it from the rest of the plasma. The Debye length, λ_D is the length at which the electrostatic potential of the point charge is screened, so that it is not felt by the other particles and it is given by

$$\lambda_D = \left(\frac{\varepsilon_0 k_B T}{n_0 e^2} \right)^{\frac{1}{2}}, \tag{1.2}$$

where k_B is Boltzmann's constant, T is the temperature of the plasma and n_0 is the number density of particles. One definition of a plasma is that the plasma "size" should be much greater than λ_D and that the number of particles in a Debye sphere (a sphere of radius λ_D) should be large. On spatial scales much larger than λ_D, the plasma is quasi-neutral, where the ion and electron number densities n_i and n_e are related through

$$Z n_i \approx n_e, \tag{1.3}$$

where Z is the charge number of the ions (i.e. $Z = 1$ for protons).

If a magnetic field is applied to the plasma, the particles are acted upon by the Lorentz force, $\mathbf{F} = q\mathbf{v} \times \mathbf{B}$, where q is the charge, $\mathbf{v}$ is the velocity and $\mathbf{B}$ the magnetic field. The force has no component parallel to either the magnetic field or the particle velocity. As such, particles will travel at a constant velocity along $\mathbf{B}$ and will undergo circular motion around $\mathbf{B}$ and therefore will move in a helix around the magnetic field lines. There are two parameters that describe the circular motion of the particles around the magnetic field lines. The first is the frequency of the motion, which we refer to as the cyclotron frequency, or the gyrofrequency and is given by

$$\omega_{cs} = \frac{qB}{m}, \tag{1.4}$$

where q is the particle charge (i.e. $q = -e$ for an electron and $q = +Ze$ for a positively charged ion and the sign reflects the direction of the gyration), m is the particle mass and s the species (i for an ion and e for an electron). The second parameter is known as the Larmor radius and gives the radius of the circular motion and is given by

$$r_L = \frac{mv_\perp}{qB}, \tag{1.5}$$

where $v_\perp$ is the magnitude of the component of the particle's velocity perpendicular to the magnetic field.

1.2 Magnetohydrodynamics

1.2.1 Introduction and governing equations

The theory of magnetohydrodynamics (MHD) describes plasma behaviour at the macroscopic level. As such, we are not interested in the dynamics of individual particles, but rather their collective behaviour. A description of any system is only valid on certain time and length scales and in a plasma, we know that the electrons and ions gyrate around the magnetic field at their characteristic frequencies. For MHD, the frequencies of interest are $\omega \ll \omega_{ci}$. With regards to the relevant length scales, one is interested in those that encompass many particles. On such scales, the plasma is electrically neutral and one can describe it in terms of bulk parameters, such as mass density and flow velocity. As MHD describes plasma behaviour on large scales, the plasma must be collisional, meaning that characteristic timescales are longer than the collision time and characteristic spatial scales are longer than the mean free path. In addition, characteristic speeds (such as the Alfvén speed) are assumed to be much smaller than the speed of light c and thus all motion is non-relativistic. Below, we show the variation in plasma β with height in the solar atmosphere, which provides a measure of the ratio of the sound speed to the Alfvén speed.

The equations that describe plasma behaviour in this regime are those of hydrodynamics (the Navier-Stokes equations), supplemented by the equations of electrodynamics (Maxwell's equations). The equations are as follows:

$$\frac{\partial \rho}{\partial t} + \nabla \cdot (\rho \mathbf{v}) = 0 \tag{1.6}$$

$$\rho \left[\frac{\partial \mathbf{v}}{\partial t} + (\mathbf{v} \cdot \nabla) \mathbf{v} \right] = \mathbf{J} \times \mathbf{B} - \nabla p \tag{1.7}$$

$$\frac{\partial \mathbf{B}}{\partial t} = \nabla \times (\mathbf{v} \times \mathbf{B}) \tag{1.8}$$

$$\nabla \times \mathbf{B} = \mu_0 \mathbf{J} \tag{1.9}$$

$$\left[\frac{\partial}{\partial t} + (\mathbf{v} \cdot \nabla)\right] \left(\frac{p}{\rho^\gamma}\right) = 0, \tag{1.10}$$

which are known as the equations of continuity, momentum, induction, Ampère and energy, respectively. Here, ρ is the mass density of the plasma, $\mathbf{v}$ the flow velocity, $\mathbf{B}$ the magnetic field strength, p the gas pressure and $\mathbf{J}$ the current density. γ is the ratio of specific heats and μ_0 the permeability of free space. These equations are known as the equations of **ideal** MHD, because they do not include any dissipative effects, such as viscosity, resistivity, thermal conduction or radiation. The energy equation, as presented, represents an adiabatic system, in which there is no heat input or loss. In more complicated cases, where such effects are important, the equation would contain more terms.

If the plasma is incompressible, the velocity field is divergence free. Expanding the second term on the left hand side of the continuity equation gives

$$\frac{\partial \rho}{\partial t} + \rho \left(\nabla \cdot \mathbf{v}\right) + \mathbf{v} \cdot \nabla \rho = 0. \tag{1.11}$$

The first and last terms can be combined in convective derivative notation to give

$$\frac{D\rho}{Dt} = -\rho \left(\nabla \cdot \mathbf{v}\right) \tag{1.12}$$

which tells us that if the mass density does not change with time, then $\nabla \cdot \mathbf{v} = 0$.

In the momentum equation, the Lorentz force term gives rise to two forces. By making use of Ampère's law, this term can be written as

$$\mathbf{J} \times \mathbf{B} = \frac{1}{\mu_0} \left(\nabla \times \mathbf{B}\right) \times \mathbf{B} = \underbrace{-\nabla \left(\frac{B^2}{2\mu_0}\right)}_{pressure} + \underbrace{\frac{1}{\mu_0} \left(\mathbf{B} \cdot \nabla\right) \mathbf{B}}_{tension}. \tag{1.13}$$

In equation 1.13, the magnetic pressure force seeks to drive the plasma away from regions of strong magnetic field and the tension force acts to straighten curved field lines, like the tension in a string.

We define a dimensionless parameter called the plasma β that is simply the ratio of the gas and magnetic pressures, the latter of which is given by

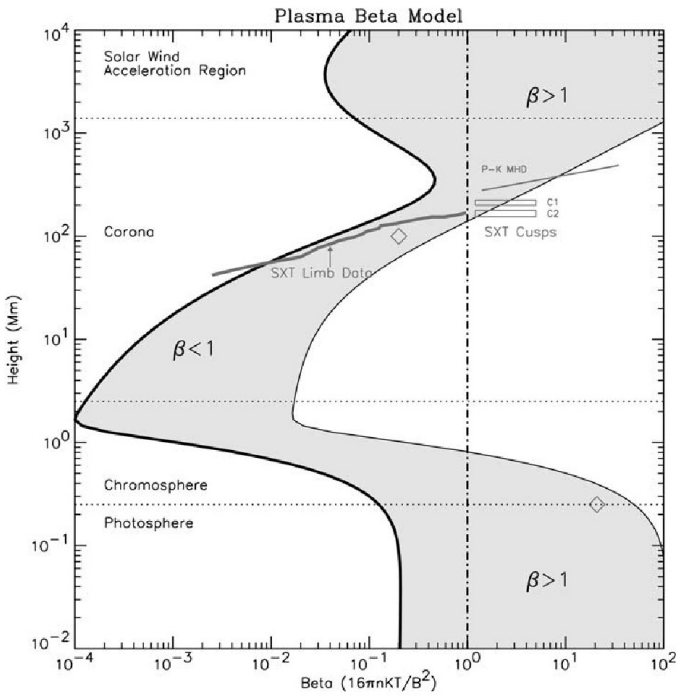

Figure 1.1: A model of the variation in plasma β with height in the atmosphere, from Gary (2001).

$$p_{mag} = \frac{B^2}{2\mu_0}. \tag{1.14}$$

The β is large when the gas pressure dominates the dynamics (such as in the solar photosphere) and small when it is the magnetic field that controls them (as in the solar corona). Figure 1.1 shows the variation in β with height in the solar atmosphere, for field strengths of 100 and 2500 G.

1.2.2 Magnetohydrodynamic waves

If the system described by the equations given in the previous section is perturbed, waves will be generated as the forces on the plasma attempt to restore the equilibrium configuration. Since there is a gas pressure, we indeed have sound waves as in any other fluid, but as described above, there are two more restoring forces in the momentum equation: a magnetic pressure and a magnetic tension. These, in turn, give rise to new wave modes. In the following two sections, we describe the waves

present in a uniform plasma and then in a cylindrical plasma structure, which is relevant for the structures under study in this thesis.

Waves in a uniform plasma

There are three basic kinds of waves in MHD: the Alfvén wave and the fast and slow magnetoacoustic waves. The Alfvén wave is associated with the magnetic tension force and is therefore an incompressible wave, since it does not cause changes in the density. Since the tension force is concerned with the curvature of the field lines, displacements associated with the Alfvén wave are naturally transverse to the field. The dispersion relation for Alfvén waves is given by

$$\omega = k v_A \cos\theta, \tag{1.15}$$

where ω is the frequency, k the wavenumber, v_A the Alfvén speed and θ the angle between the wave vector and the magnetic field. From equation 1.15, we see that the phase velocity of the Alfvén wave is maximum along the magnetic field (with value equal to the Alfvén speed) and zero perpendicular to it. The group velocity is directed along the magnetic field and its value is the Alfvén speed.

If the plasma is compressible, in addition to the Alfvén wave, the fast and slow magnetoacoustic waves are supported. In the former, the restoring force is a combination of the gas and magnetic pressures, while the gas pressure is the sole restoring force for the latter. The slow wave is an anisotropic one and cannot propagate perpendicular to the magnetic field. The fast wave, on the other hand is more or less isotropic. Both the phase and group velocities for the fast wave obtain their maximum values perpendicular to the magnetic field, but the values parallel to the field are close to that maximum. The dispersion relation for fast and slow waves is

$$\omega^2 = \frac{(c_S^2 + v_A^2)k^2}{2}\left[1 \pm \sqrt{1 - \frac{4c_T^2}{(c_S^2 + v_A^2)}\frac{k_\parallel^2}{k^2}}\right], \tag{1.16}$$

with the so-called tube speed, c_T given by

$$c_T = \frac{c_S v_A}{(c_S^2 + v_A^2)^{\frac{1}{2}}} \tag{1.17}$$

and where c_S is the sound speed, k the magnitude of the wave vector and $k_\parallel$ the

magnitude of its component parallel to the magnetic field. Figure 1.2 shows polar plots of the phase and group velocities for the three types of wave discussed here. A more detailed description of the basic wave modes can be found in the book by Goossens (2003).

Waves in cylindrical plasma structures

The structures whose oscillations are studied in this thesis, sunspots, are considered to be composed of either one or many magnetic flux tubes (see section 1.5.1). One usually thinks of a magnetic flux tube as a cylinder of plasma with a certain density, pressure and magnetic field that is embedded in a plasma with different values of those quantities. This structuring of the plasma gives rise to different wave modes than in the case of a uniform plasma and we briefly discuss those in this section. For the cylinder to exist in equilibrium (and considering only straight magnetic field lines), there must be a balance of the total pressures in the perpendicular direction (across the magnetic field and gravity) on either side of the boundary between the cylinder and the external medium, i.e.

$$p_i + \frac{B_i^2}{2\mu_0} = p_o + \frac{B_o^2}{2\mu_0}, \tag{1.18}$$

where p and B denote the values of gas pressure and magnetic field either side of the boundary and the subscripts i and o refer to inside and outside the boundary, respectively.

One can then perturb the equilibrium with harmonic perturbations of the form

$$R(r) \exp\left[i\left(\omega t + m\theta + kz\right)\right], \tag{1.19}$$

where m is the azimuthal wavenumber, k is the wavenumber in the z-direction and ω the frequency of the wave and by doing so, the dispersion relation for the waves can be derived (Edwin & Roberts 1983):

$$\rho_i \left(k^2 v_{Ai}^2 - \omega^2\right) n_o \frac{K_m'\left(n_o a\right)}{K_m\left(n_o a\right)} = \rho_o \left(k^2 v_{Ao}^2 - \omega^2\right) m_i \frac{J_m'\left(m_i a\right)}{J_m\left(m_i a\right)}, \tag{1.20}$$

where J_m and K_m are modified Bessel functions (with primed variables indicating their derivatives), a is the radius of the cylinder and n_o is given by

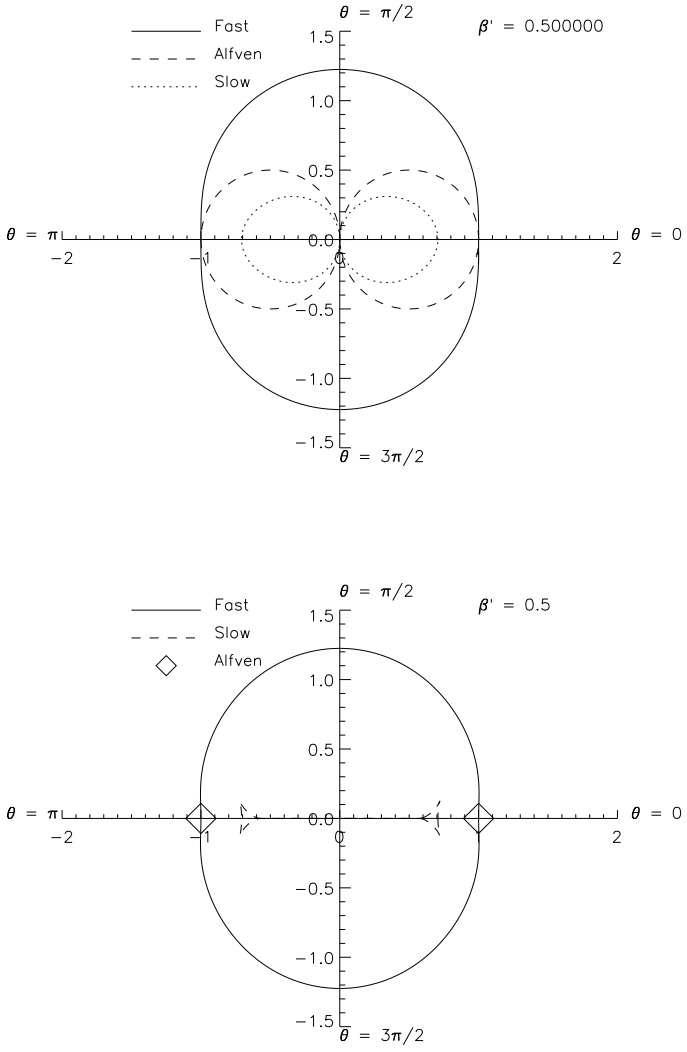

Figure 1.2: Polar plots of the phase (top) and group (bottom) velocities for the three types of MHD waves in a uniform plasma. The magnetic field lies in the positive x direction.

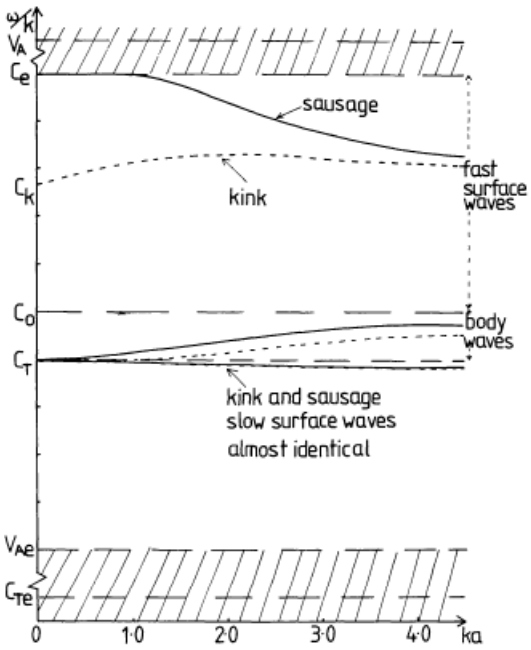

Figure 1.3: Phase speeds as a function of wavenumber for waves in a magnetic cylinder, under photospheric conditions. Figure from Edwin & Roberts (1983).

$$n_o^2 = \frac{\left(k^2 c_o^2 - \omega^2\right)\left(k^2 v_{Ao}^2 - \omega^2\right)}{\left(c_o^2 + v_{Ao}^2\right)\left(k^2 c_{To}^2 - \omega^2\right)}. \tag{1.21}$$

Waves for which the azimuthal wavenumber, $m = 0$ are known as "sausage" modes, for $m = 1$, they are called "kink" modes and those for which $m \geq 2$ are known as "fluting" or "ballooning" modes. Due to periodicity constraints, the value of m can only be an integer. The dispersion relation given in equation 1.20 is for body modes, which are oscillatory inside the tube and evanescent outside it. Two regions of phase speeds exist: $v_{Ai} < v_{ph} < v_{Ao}$ and $c_{Ti} < v_{ph} < c_{so}$, which are known as the fast and slow branches, respectively. Figure 1.3 shows dispersion curves for sausage and kink oscillations under photospheric (high β) conditions.

Wave propagation in a stratified medium

The inclusion of the gravitational force, $-\rho g \hat{\mathbf{z}}$ in the momentum equation affects the dispersion relations for the wave propagation and these effects are considered here. We consider an isothermal atmosphere, in which the density varies as $\exp(-\frac{z}{\Lambda})$,

where Λ is the density scale height. The MHD equations are perturbed, linearised and combined to give a generalised wave equation. We then seek plane wave solutions of the form $\mathbf{v} = \mathbf{v_0} e^{[i(\mathbf{k}\cdot\mathbf{r}-\omega t)]}$.

When there is no magnetic field, we have acoustic-gravity waves, for which the dispersion relation is given by (e.g. Priest 1982)

$$\omega^2 \left(\omega^2 - N_s^2\right) = \left(\omega^2 - N^2 \sin\theta_g'\right) k'^2 c_s^2, \tag{1.22}$$

in which N is called the Brunt-Väisälä frequency, θ_g' is the angle between the wavevector $\mathbf{k'} = \mathbf{k} + \frac{i\gamma g}{2c_s^2}\hat{\mathbf{z}}$ and $\hat{\mathbf{z}}$ and $N_s = \frac{\gamma g}{2c_s}$. If we consider propagation in the vertical direction only, so that $\theta_g' = 0$, the dispersion relation reduces to

$$\omega^2 = k'^2 c_s^2 + N_s^2, \tag{1.23}$$

so we have acoustic waves that have a cut-off at $\omega = N_s$ and therefore any waves below this frequency are evanescent. Since N_s depends on the sound speed, it of course varies with height in the atmosphere. Remembering that the solutions are those for plane waves, we have

$$\mathbf{v} = \mathbf{v_0} \exp\left[i\left(\mathbf{k'} - \frac{i\gamma g}{2c_s^2}\hat{\mathbf{z}}\right)\cdot\mathbf{r} - i\omega t\right] = \mathbf{v_0} \exp\left[i\left(\mathbf{k'}\cdot\mathbf{r} - \omega t\right)\right] \exp\left(\frac{\gamma g z}{2c_s^2}\right), \tag{1.24}$$

which shows that the amplitudes of the waves will increase exponentially with height.

If the magnetic field is then included, plane wave solutions are allowed if $N_s \ll kc_s$, so that the wavelength is a lot smaller than the density scale height. The dispersion relation for the magnetoacoustic-gravity waves is given by

$$\omega^4 - \omega^2 k^2 \left(c_s^2 + v_A^2\right) + k^2 c_s^2 N^2 \sin^2\theta_g + k^4 c_s^2 v_A^2 \cos^2\theta_B = 0, \tag{1.25}$$

where θ_B is the angle between the wavevector and the magnetic field. In the case where $c_s^2 \leq v_A^2$ the dispersion relation is reduced to that for the magnetoacoustic waves in a uniform plasma, meaning that gravity has no effect on the waves. If c_s^2 is much greater than v_A^2, the waves produced are an acoustic wave and a magnetoacoustic-gravity wave, whose dispersion relation is

$$\omega^2 = N^2 \sin^2\theta_g + k^2 v_A^2 \cos^2\theta_B. \tag{1.26}$$

1.3 Regions of the Sun

The Sun is our nearest star and provides light and warmth needed to sustain all life on Earth. In this section, we review the structure of the Sun, starting with the solar interior. A diagrammatic view of the structure described below can be seen in figure 1.4.

Like all stars, the Sun generates its energy in the core, by the process of nuclear fusion. Hydrogen atoms are fused together to produce helium atoms and photons, through a chain of reactions known as the proton-proton chain. The radiation pressure provided by these nuclear reactions is what balances the gravitational force and thus prevents the star from collapsing on itself.

The core is approximately 30% of the solar radius and out to approximately 71% of the radius, the transport of energy is mainly by radiation. From there to the surface, convection is the dominant mode of energy transport. The base of the convection zone is associated with a region known as the tachocline. The Sun rotates at different rates as a function of latitude, but at the tachocline, the rotation rate becomes uniform, similar to the rotation of a solid body. The differential rotation amplifies the magnetic field and turns it from purely poloidal to being toroidal. The maintenance of the magnetic field against decay is performed by the dynamo mechanism. The plasma is an electrically conducting fluid and its motion relative to the existing magnetic field generates electric fields. In turn, the electric fields give rise to currents, which generate magnetic fields through Ampère's law.

This field is thought to be concentrated in magnetic flux tubes, which gradually approach the solar surface due to buoyancy and it appears in the form of spatially localised magnetic elements, in particular sunspots.

The "surface" of the Sun is known as the photosphere and is the region from which most of the solar optical radiation is emitted. Since this layer is above the convection zone, images of the Sun taken at optical wavelengths show granulation patterns. Bright granules with a typical size of 700 km are seen and these are regions of hot material moving upwards. Separating the granules are dark inter-granular lanes, where cool material sinks back down. At times of high solar activity (see the next section), the photosphere is dotted with sunspots, the objects under study in this thesis. The photosphere has an effective temperature of approximately 6000 K.

Above the photosphere lies the chromosphere, which has a much lower density (and therefore a lower intensity of radiation) than the photosphere. The tem-

perature is seen to reach a minimum of approximately 4000 K in the photosphere and then begins to rise steadily in the chromosphere. Due to the low intensity of chromospheric radiation, the region is only visible when the photosphere is eclipsed. Such an eclipse occurred in 1868, which resulted in the discovery of helium, made by Pierre Janssen (see, e.g. Kochhar 1991).

When the electron in a hydrogen atom makes a transition from the $n = 3$ to $n = 2$ energy level, the photons emitted have a wavelength of $\lambda = 656.3$ nm and the emission is known as "Hα". The core of the Hα emission line is formed in the chromosphere and many images from the solar chromosphere are taken at this wavelength. Hα shows features such as solar prominences, as well as a supergranulation pattern. The former are large dense regions of plasma suspended in a magnetic field, while the latter are extensions of the granulation pattern observed in the photosphere. While the granules in the photosphere have typical sizes of 700 km, chromospheric supergranules are observed to have typical sizes of 30 000 km.

Lying above the chromosphere are the transition region and corona. The transition region is a relatively thin layer of the solar atmosphere where the temperature gradient is very steep, until the temperature reaches a value in excess of 10^5 K. The corona is the region of the atmosphere overlying the transition region, where the temperature has reached a value of 1 MK or more. Unlike other regions of the atmosphere, the corona does not have a well defined boundary and thus reaches far into space. The fact that the coronal temperature is so high is still an unresolved problem in solar physics, known as the "coronal heating" problem.

The plasma in the corona is highly ionised and emission is mainly produced by minor, heavy, highly ionised elements (e.g. iron, magnesium and oxygen) in the extreme ultraviolet (EUV) and X-ray regions of the electromagnetic spectrum. In addition, free electrons and protons gyrating around the magnetic field produce gyroresonant emission (at wavelengths of e.g. 1.76 cm). Images of the Sun taken at these wavelengths show that the corona is highly structured; many coronal loops are seen, which trace the magnetic field lines. The plasma β in the corona is low, meaning that the plasma is confined to the field lines. These observations provide motivation for the study of waves in cylindrical structures presented in the preceding section. Perhaps the most prominent structures seen in the corona are the so-called "active regions" (ARs), which show up as bright regions in EUV and X-ray wavelengths. ARs are regions of strong concentrations of magnetic field and in the corona, these regions appear as bundles of loop structures, which trace the magnetic

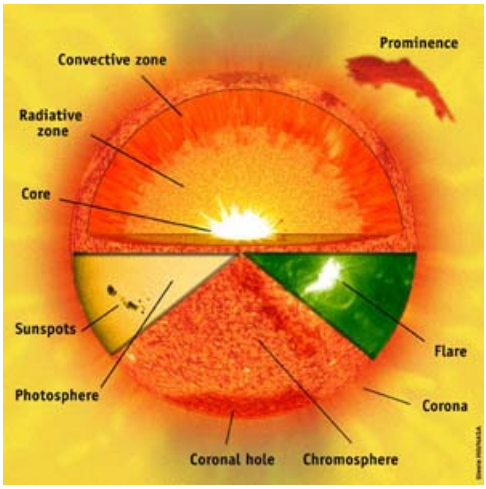

Figure 1.4: A diagram showing the structure of the Sun. Figure courtesy of the SOHO project.

field. Also seen in the corona are features much darker than the surroundings - these are coronal holes where the magnetic field lines are open.

1.4 The solar cycle and solar activity

It is well known that the Sun has a magnetic field (which was discovered by Hale in the 1900s) and it is thought that the field is generated by a dynamo process located at the tachocline. Since the magnetic field lines are frozen into the plasma, the differential rotation causes an initially poloidal field to be converted into a toroidal one. This process takes a period of 11 years (see below) and then the inverse process occurs - a toroidal field is converted back to a poloidal one.

Sunspots are seen as dark features on the solar surface and are the most visible manifestation of magnetic activity on the Sun. In the next section, these features are described in more detail, but here, we describe the solar cycle in general terms.

It was Schwabe in the 1800s who discovered that the number of sunspots observed varies periodically, with an average period of 11 years. At the beginning of each new cycle, new spots appear at high latitudes (at approximately $\pm$ 30°) and over the course of the cycle, spots tend to appear at progressively lower latitudes (so that by the end, new spots are appearing near the equator). If one plots the

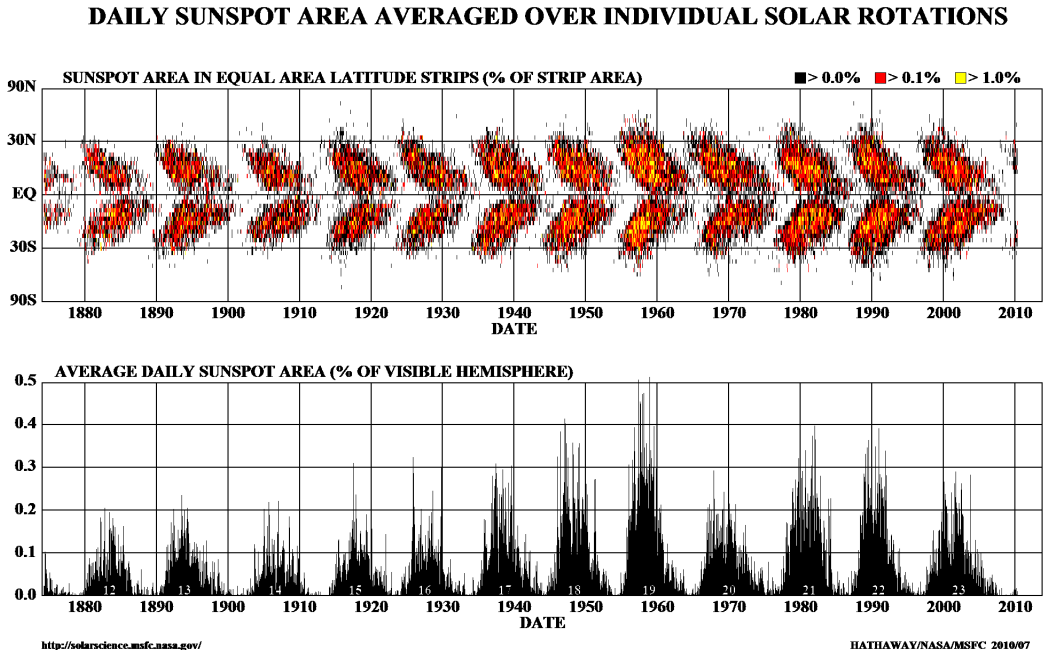

Figure 1.5: The butterfly diagram (top) and average sunspot covered area (bottom) showing the 11 year sunspot cycle periodicity. Figure courtesy of D. Hathaway (NASA/MSFC).

latitudes of new spots as a function of time, a "butterfly diagram" is produced and of course, this has the 11 year periodicity of the cycle. Both the cyclic behaviour of the sunspot number (or sunspot area) and the butterfly diagram can be seen in figure 1.5. The terms "solar maximum" and "solar minimum" are used to refer to periods when there are many and few sunspots, respectively. Between the years 1645 and 1715, the number of sunspots seen was very low and this period is now referred to as the Maunder minimum. Near solar maximum, occurrences of solar flares (large releases of energy often imaged in Hα) and coronal mass ejections are frequent.

Observations of the magnetic polarities in sunspot groups show that in a given hemisphere, most sunspot groups have the same leading polarity (in the sense of solar rotation). In the other hemisphere, the leading polarity is opposite to this. In each new cycle, the leading magnetic polarity in each hemisphere switches and this phenomenon is known as the Hale-Nicholson law and is shown in figure 1.6.

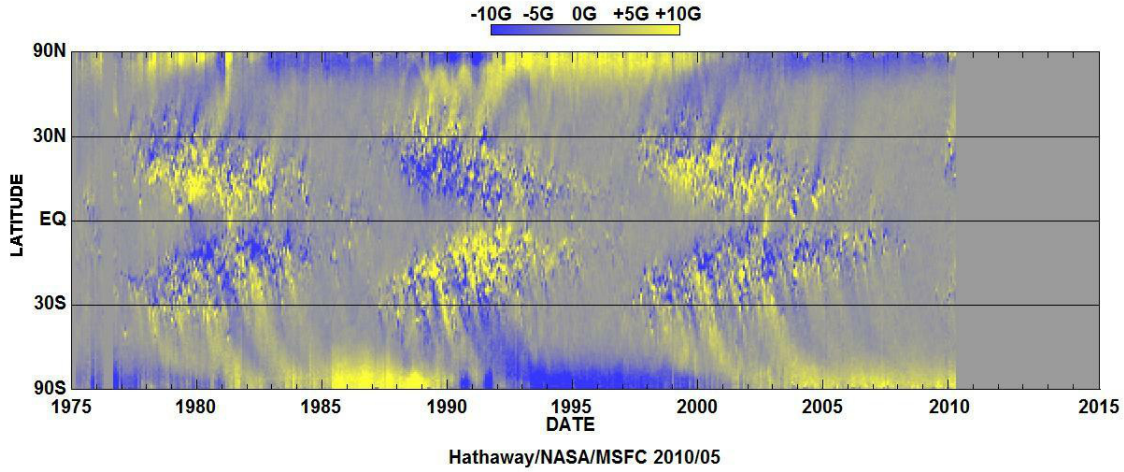

Figure 1.6: Magnetic butterfly diagram, showing the change in magnetic polarity with time. Figure courtesy of D. Hathaway (NASA/MSFC).

Since the leading polarity switches from one cycle to the next, it takes two cycles for it to return to its original polarity. Thus, there is a 22 year solar magnetic cycle.

1.5 Sunspots

1.5.1 General properties and features

As was mentioned previously, sunspots are dark features seen on the solar surface and consist of a dark central region known as the **umbra** that is surrounded by a less dark and filamentary region known as the **penumbra**. In visible light, the penumbra is seen to be composed of alternating bright and dark filaments. Figure 1.7 shows a fairly circular sunspot imaged in an optical wavelength, in which the contrast between the spot and the surrounding photosphere is very apparent. Typically, the umbra radiates in the region of 20-30% of the quiet Sun flux and the penumbra radiates in the region of 75-85% of the quiet Sun flux.

The darkness of a sunspot relative to its surroundings is due to the presence of a strong magnetic field (a typical field strength is $B \sim 2.8$ kG in the photosphere). The magnetic field is able to suppress the convective motions that happen below

the photosphere and since convection is the dominant mechanism for transporting energy in that region of the Sun, there is a thermal energy deficit between the sunspot and the surroundings. Observations of the magnetic field in sunspots have shown that in the umbra, the field is almost purely vertical and when moving radially outwards, the field is seen to become more inclined to the vertical. In other words, the magnetic flux tube diverges with height. In the penumbra, the field has an average inclination of up to 70° to the vertical. Observations have long shown the presence of a horizontal, radial outflow in the penumbra known as the Evershed flow. Since the magnetic field is strong, the flow must be directed along the magnetic field lines. Title et al. (1993) showed that the inclination of the magnetic field was different in the bright and dark filaments; in the latter, the fields are almost horizontal, while in the former, the inclination is around 50°-60°. The Evershed flow was also observed to be confined to the dark filaments. In the chromosphere, the flow is directed inwards and this is known as the inverse Evershed effect.

Schlichenmaier & Schmidt (2000) and other authors have observed that just outside the outer penumbral boundary, (or in some cases within the penumbra) the Evershed flow is directed vertically into the solar surface. Westendorp Plaza et al. (1997) found that some magnetic field lines followed the flow and were thus also directed downwards. As discussed in section 1.2.2 above, the flux tubes must be in pressure balance with their surroundings. Hence, due to the magnetic pressure inside the tubes, the density of the plasma must be lower than in the quiet Sun, meaning that the tubes are buoyant and tend to rise. The mechanism to keep the flux tubes submerged below the surface is known as "magnetic pumping" (Weiss et al. 2004). The magnetic field lines are carried aside by the fluid in the rising and expanding convection granules and are then dragged downwards by the fluid in the inter-granular lanes.

Since the gas pressure in the solar atmosphere decreases with height, so too must the magnetic flux in the sunspot, in order for the structure to remain in pressure balance. Thus, the area of the sunspot's flux tube increases with height.

Sunspots can appear individually, or as part of groups. Sunspot groups, in turn, may be as simple as consisting of two spots of opposite magnetic polarity, or have more complex configurations. Given the complexity of such configurations, it is useful to have a classification scheme. The Zürich and McIntosh (McIntosh 1990) classification schemes classify the complexity of the groups and the Mt. Wilson magnetic classification scheme enables one to identify the complexity of the magnetic

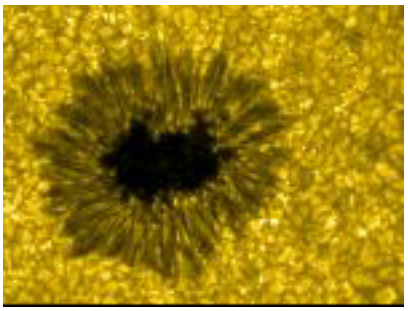

Figure 1.7: The sunspot of active region 10969, taken in the G band ($\lambda = 430.5$ nm) with the Solar Optical Telescope on board the Hinode spacecraft.

field structure in a given group. In the McIntosh classification, for example, there are 3 components, which are determined by properties such as the presence of a penumbra, the maturity of the penumbra and the amount of space between the dominant spots. The magnetic classification identifies, in particular, whether the group consists of two dominant spots of opposite polarity, whether the distribution of polarities is complicated, et cetera. Since sunspots are dynamic features, the classifications for a given group change over the course of its evolution.

There are two models of the structure of a sunspot that are in common use. The simplest model, proposed by Cowling was that of a single magnetic flux tube and is usually referred to as the monolithic model. Modern versions of this model allow the physical variables (such as density and magnetic field strength) to be non-uniform in the tube and so in regions of relatively low field strength, convection is less suppressed.

Parker (1975) proposed a model in which the sunspot was composed of many individual flux tubes, which is usually referred to as the cluster (or spaghetti) model. The tubes are tightly grouped together, but are separated by regions containing no magnetic field. Thus, in these field free regions, the convection is again less suppressed. In either model, then, one would expect to see bright features in the umbra showing signs of the underlying convection. Such features are indeed seen and are called umbral dots.

Another feature observed in sunspots is the so-called Wilson depression, due to a decreased opacity. This in turn means that one is able to see deeper into a sunspot than the quiet Sun and so the structure appears depressed on the surface. The maximum value of the Wilson depression can be as much as 600 km, in the

centre of the umbra (see, e.g. Thomas & Weiss 2008). There are two causes of the decreased opacity. The first is due to the lower temperature than the surroundings, which means there is less photoionisation and so the bound-free opacity is decreased. The other cause is due to the strong magnetic field, which gives rise to a large magnetic pressure. As such, the gas pressure inside the sunspot is small, which in turn means that the density of the plasma there is low. If the density is low, there are fewer particles to absorb the radiation and this again leads to a lower opacity.

1.5.2 Formation and lifetimes

The first stage of the formation of a sunspot involves the emergence of magnetic flux through the solar photosphere. A loop of plasma containing magnetic flux that is buoyant rises through the convection zone and then penetrates the solar surface. Small concentrations of emerged magnetic flux can form pores, which are essentially sunspot umbrae and then the pores coalesce to form larger pores (see, e.g. Vrabec 1974). Zwaan (1978) suggests that this coalescence is due to the emerging magnetic structure forming a "tree". That is, a thick flux tube consists of several thinner tubes.

A penumbra begins to form when the diameter of the pore exceeds a threshold of about 3.5 Mm (Solanki 2003), though in some cases, this threshold can be as large as twice this value (Thomas & Weiss 2008). Leka & Skumanich (1998) found a threshold on the magnetic flux of 1-1.5 $\times 10^{20}$ Mx, above which a partial penumbra begins to form. The penumbra is formed in segments and the first of these usually appear on the side of the sunspot pointing away from the opposite flux concentration in the region. The entire penumbra can be completed on a timescale of a few hours (e.g Schlichenmaier et al. 2010).

It has been found that leading and following sunspots have very different lifetimes. Leading spots are observed to be the most round and stable; their lifetimes can be up to several months. In the case of following spots, their maximum lifetimes can be up to several days. The lifetime of a sunspot has been found to obey the Gnevyshev-Waldmeier rule, which states that the maximum area of the sunspot is proportional to its lifetime, with a constant of proportionality $D_{GW} = 10.89 \pm 0.18$ MSH day^{-1} (though Petrovay & van Driel-Gesztelyi (1997) show that a parabolic decay law exists), where MSH = millionth of a solar hemisphere (area).

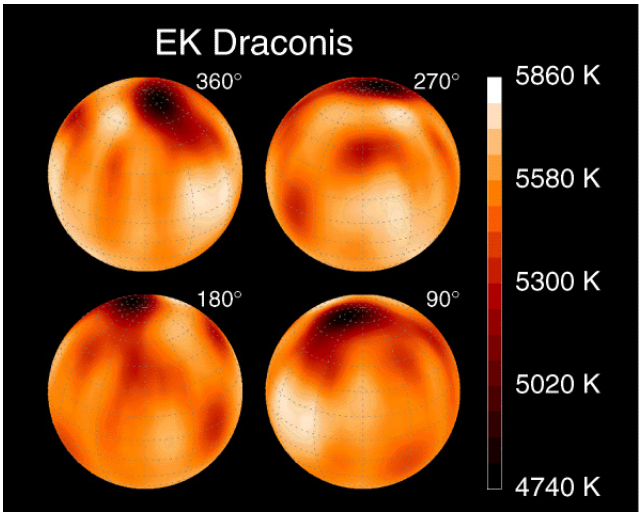

Figure 1.8: Doppler images of the star EK Draconis at different points of its rotation. Figure courtesy of K. G. Strassmeier.

1.5.3 Starspots

Starspots are of obvious interest due to their relation to sunspots. Learning more about spots on stars of different spectral type to the Sun may offer more insight into the dynamo mechanism for generating a stellar magnetic field and how that changes during a star's lifetime. Just as sunspots are regions of intense magnetic field, the same is true for starspots. However, there are some fundamental differences between sunspots and starspots that have been observed so far. The most obvious differences are the size and location of starspots. Figure 1.8 shows images of the (solar-like) star EK Draconis produced using a technique known as Doppler imaging. Near the north pole of the star, a large region of low temperature is seen. These images show that starspots are located at much higher latitudes and cover a larger fraction of the stellar area than their solar counterparts.

Many properties of spotted stars can be found in Strassmeier (2009) and it can be seen there that the majority of these are of different spectral type to the Sun and have short rotation periods, of the order of hours to days. Stars with such short rotation periods (relative to the Sun) are known to be highly magnetically active. Strassmeier (2009) provides a full review of the current state of our knowledge of starspots.

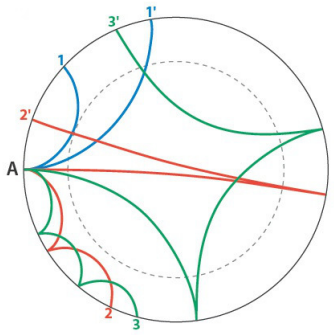

Figure 1.9: Ray paths for several different acoustic oscillations. This image has been taken from Gizon et al. (2010).

1.6 Seismology of the Sun

1.6.1 Helioseismology

The subject of helioseismology involves studying the waves present in the solar interior in order to learn more about its structure and is analogous to the way seismologists on Earth study waves from earthquakes in order to learn about our planet's interior.

There are three types of oscillation mode that are present: p modes, f modes and g modes. The first have the gas pressure gradient as their restoring force and are known as sound waves. These modes have typical periods of 5 minutes and are thought to be generated by turbulent convection below the photosphere. They are standing waves that are trapped in the convection zone; their upper boundary at the photosphere is due to the sharp drop in density and their lower boundary is determined by the increasing temperature with depth into the interior. The sound speed is proportional to the temperature and as it increases, the waves become refracted away from the normal and so return to the surface. Those waves that return to the surface less often (i.e. have a longer horizontal wavelength) probe deeper into the interior. This is shown in figure 1.9 for three different modes, each penetrating to a different depth in the solar interior.

The f and g modes have gravity as their restoring force. The former are restricted to the photosphere and as such are usually referred to as "surface gravity" waves. The g modes, on the other hand, are said to be low frequency modes and

confined to the solar interior, below the convection zone. To date, there has not been a confirmed detection of the solar g modes and a group of solar astronomers known as the Phoebus Group[1]has been set up to detect them.

1.6.2 Coronal seismology

Coronal seismology is a much younger field of solar seismology than helioseismology and major steps forward in the field have been due to the space based observational facilities SOHO (the Solar and Heliospheric Observatory) and TRACE (the Transition Region and Coronal Explorer). As mentioned in section 1.3, the corona is a highly structured region of the solar atmosphere, in which the plasma is arranged in coronal loops.

The major goal of coronal seismology is to determine values of physical parameters in the corona. Measuring the various parameters of the observed MHD waves (Alfvén and the fast and slow magnetoacoustic modes, both propagating and standing) can enable one to determine such parameters. Indeed, two of the successes of coronal seismology have been the first measurement of the magnetic field in a coronal loop by Nakariakov & Ofman (2001) and the discovery of the fine field-aligned filamentation of the closed magnetic field regions by Robbrecht et al. (2001), King et al. (2003) and Van Doorsselaere et al. (2008). A full review of coronal seismology through observations of oscillations has been written by Nakariakov & Verwichte (2005).

1.6.3 Sunspot oscillations

Various kinds of oscillations have been observed in sunspots and here, we review the most common ones. In the late 60s, periodic "umbral flashes" were discovered in the Ca II H and K lines formed in the chromosphere (Beckers & Tallant 1969). The umbral flashes are rapid increases in intensity in the core of the spectral lines in which they're detected and the intensity subsequently decays gradually. The average period of these umbral flashes was found to be about 145 s (Beckers & Tallant 1969).

Soon after the discovery of umbral flashes, oscillations in sunspot umbrae with periods of around 3 minutes were observed in both intensity (Bhatnagar & Tanaka 1972) and vertical velocity (Giovanelli 1972) measurements in Hα. These 3 minute oscillations are the most studied of all kinds of observed sunspot oscillations.

[1] http://www.issi.unibe.ch/teams/GModes/issi.html

Given the strong magnetic field present in sunspots, such oscillations should possibly be modelled as MHD waves. In particular, Centeno et al. (2006) have interpreted these 3 minute oscillations in terms of propagating slow magnetoacoustic waves and De Moortel et al. (2002) observed similar periods in coronal loops above a sunspot and used the same interpretation. The 3 minute oscillations have been observed to have sawtooth-like profiles (see, e.g Brynildsen et al. 1999a) and this is consistent with upward propagating waves, due to the large gradient in temperature through the atmosphere.

Brynildsen et al. (1999b) studied oscillations in lines formed at different heights in the transition region above a sunspot in both intensity and line-of-sight velocity, with the SOHO/SUMER instrument. Their observations showed that the intensity and velocity oscillations were in phase in the umbra and had periods of 3 minutes. In addition, it was found that there was a time delay between the arrival of the wave in two particular lines (N V, $\lambda = 1238$ Å; O V, $\lambda = 629$ Å), with the wave arriving earlier in the line formed at a lower height, suggesting an upward propagating wave. Interestingly, no shocks were observed in the observations. Shibasaki (2001) performed a follow-up study of the same sunspot using the Nobeyama Radioheliograph (see section 1.8.1 below) and detected 3 minute oscillations in his observations of the radio brightness temperature. Using measurements from the work of Brynildsen et al. (1999b), he was able to confirm their hypothesis of the waves being upwardly propagating. He also calculated a value for the temperature minimum in the sunspot umbra, of about 4100 K (see section 3.3 of Shibasaki 2001).

Kobanov & Makarchik (2004) also observed waves in the umbral chromosphere (in Hα) of a sunspot with periods of 2.8 minutes. The waves they observed were seen to propagate radially outwards from the sunspot centre, with a phase velocity of 45-60 km s^{-1}. Interestingly, they inferred that these waves could be related to the umbral flashes mentioned above, given their numerous similarities with that phenomenon (such as period, propagation speed and size). However, it is known that umbral flashes also show brightening in Hα, but the authors did not observe such features in their Hα data. In any case, figure 1.10 shows the line of sight velocity as function of position and time, from Kobanov & Makarchik (2004). Clear "chevron" shaped structures are seen, with the apex of the structure coinciding with the umbral centre. These structures indicate the propagation of the waves.

Even though there have been many studies of the 3 minute oscillations, many of them focus solely on their temporal properties (e.g. periods) and not on their

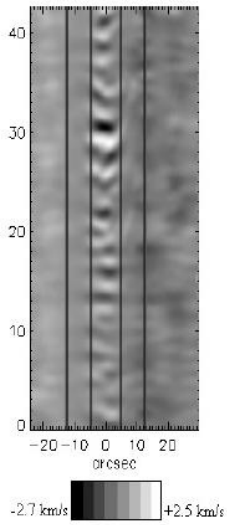

Figure 1.10: Line of sight velocity, in both space and time. Figure courtesy of Kobanov & Makarchik (2004).

spatial properties. This is probably due, in part, to the limited spatial resolution of available instruments. In this thesis, a correlation analysis of the 3 minute oscillations (observed with the Hinode spacecaft; see section 1.8.2) is presented and this represents a new contribution to the field.

Oscillations with periods of 5 minutes have also been observed in photospheric sunspot umbrae (see, e.g. Thomas et al. 1984). Above, it was mentioned that the solar p modes have periods of 5 minutes and since the flux tube of a sunspot is embedded in the convection zone, one would naturally expect the presence of 5 minute oscillations in sunspots. It is thought that the 5 minute umbral oscillations are present due to the p modes constantly hitting the flux tube of the sunspot. However, the amplitudes of 5 minute oscillations in sunspots are observed to have lower amplitudes (by a factor of 2-3) than their quiet Sun counterparts.

Several mechanisms have been proposed to explain the lower amplitude of the 5 minute umbral photospheric oscillations. The p modes are thought to be generated by turbulent convection and it is known that the strong magnetic field in a sunspot partially inhibits this convection. Therefore, one explanation is simply that the p modes are not generated as strongly inside sunspots as they are in the quiet Sun. Recent simulations by Parchevsky & Kosovichev (2007) seem to confirm this;

when sources of acoustic oscillations are suppressed inside a sunspot, the decrease in oscillation amplitude is seen to agree with the observations.

Another mechanism is that the p modes are absorbed by sunspots. Braun et al. (1987) observationally investigated the difference in power of radially incoming and outgoing waves and found that sunspots can absorb up to 50% of the incoming waves at certain horizontal wavenumbers. Spruit & Bogdan (1992) suggested that the observed absorption could be due to the conversion of the incident p modes to slow magnetoacoustic waves. The conversion is said to take place at a layer where the sound and Alfvén speeds are equal.

Given that both 5 minute and 3 minute oscillations are detected in sunspot umbrae (albeit at different heights in the atmosphere), one would naturally ask if there was any connection between them. Both are known to be compressible magnetoacoustic-gravity waves (i.e. magnetoacoustic waves modified by the presence of a gravitational field) and Bogdan & Judge (2006) suggest that the 3 minute oscillations are just the high frequency tail of the broadband 5 minute photospheric oscillations that can propagate into the chromosphere. The idea is that since the atmosphere is not isothermal, the density scale height varies with height and so too does the acoustic cut-off frequency. The maximum value of the acoustic cut-off frequency reaches 5.2-5.5 mHz in the region between the photosphere and low chromosphere (Bogdan & Judge 2006) and this frequency is between the 5 minute (2-5 mHz) and 3 minute (5-8 mHz) bands. Recent simulations by Botha et al. (2011) investigated slow magnetoacoustic waves in the chromospheric cavity between the photosphere and transition region. The authors found that a broadband pulse with frequencies below the acoustic cut-off frequency could generate three minute oscillations inside the cavity. Standing waves were observed, as well as travelling waves that could reach the corona. Kobanov et al. (2011) found evidence for the effect of height inversion in 3 minute oscillations. In 9 out of 11 of their analysed sunspots, the maxima of the 3 min oscillation power in chromospheric signals were situated above the sunspot umbrae and were seen to coincide with minima in 3 min oscillation power in photospheric signals. The authors suggested that the Wilson depression or wave reflection could be the cause of this phenomenon. Lastly, Sych & Nakariakov (2008) showed that the sources of 5 min oscillation in microwave emission from sunspots was situated at the umbra-penumbra boundary.

The last category of short period oscillations to be discussed is those known as running penumbral waves (Zirin & Stein 1972; Giovanelli 1972). These waves are

a chromospheric phenomenon and are usually seen in Hα. They originate near the umbra-penumbra boundary and are observed to propagate radially (in the horizontal direction) over the entire penumbra. At their origin, their propagation speeds can be of the order 15-20 km s^{-1}, but this is seen to decrease monotonically with distance, reaching about 5-7 km s^{-1} at the penumbral boundary. Typical periods of these waves are in the range 200-300 s. Rouppe van der Voort et al. (2003) linked running penumbral waves to umbral flashes, suggesting that they were generated by the same oscillatory process. They suggested that the wavefronts propagate vertically and spread out due to the diverging nature of the sunspot magnetic field.

Various numerical studies of wave propagation in sunspots have been performed. Khomenko & Collados (2006) investigated the properties of oscillations produced by a periodic driver in a realistic magnetic field configuration. While the periods of the driver they used were unrealistic (e.g. 10 s, due to constraints on the size of their computational domain), they found that at the layer where the sound and Alfvén speeds were equal (which is located near the base of the chromosphere), the fast mode is reflected, but the slow mode can propagate into the chromosphere. They found that similar behaviour occurred for waves with different periods generated at different distances from the sunspot centre. They concluded that a large part of the energy returned to the photosphere by the reflection of the fast mode and thus waves are not a good mechanism for transporting energy into the upper atmosphere.

Khomenko et al. (2009) performed 2D MHD simulations in order to study the effects of the magnetic field on waves excited by sources below the photosphere. The authors showed that a source in a region permeated by a magnetic field will excite both fast and slow MHD waves and that the fast waves are analogous to the p-modes generated in the quiet (i.e. non-magnetic) regions of the Sun. They also found that waves with similar speeds to fast waves can propagate across the sunspot and they called those "surface magnetogravity waves". A major part of this study was to investigate the effects of the magnetic field on wave travel times. It was found that the magnetic field can produce travel times of 20-40 s shorter than for the same waves propagating in the quiet Sun. In addition, the magnetic field was observed to introduce a dependence on frequency on the wave travel times. Low frequency waves were found to travel more slowly than high frequency ones and this behaviour was attributed to the increase in Alfvén speed through the atmosphere.

Longer period oscillations

Short period oscillations as discussed above represent the most studied of oscillations in sunspots. Long period ($P > 10$ min) oscillations in sunspots could be connected with large scale reconfiguration of the Sun's magnetic field, or even the leakage of waves (g-modes) from the solar interior. The nature of such oscillations is not understood, though several studies have sought to answer this question. Berton & Rayrole (1985), using photospheric magnetic and velocity data in the neutral iron line $\lambda = 630.2$ nm, first observed torsional oscillations in the umbral magnetic field of a sunspot, with periods of approximately 45 min and suggested that these could be related to magnetohydrodynamic oscillations generated at the top of the solar convection zone. Sunspot penumbrae were also found to oscillate, as reported by Druzhinin et al. (1993), in the Doppler velocity of two spectral lines of photospheric origin (with periods around 60 min). Moreover, optical observations by Nagovitsyna & Nagovitsyn (2002) indicated two kinds of oscillation mode, with periods ranging from 40 to 100 min - one associated with sunspots and the other with pores. Nagovitsyna & Nagovitsyn (2001) also used optical observations to detect quasi-hourly oscillations in magnetic fragments in sunspots, finding that the oscillation had its maximum amplitude in the penumbra and that there was an anisotropy of the oscillation in the azimuthal direction.

More recently, oscillations of the line-of-sight velocity with periods from 60 to 80 minutes have been detected in sunspots (Efremov et al. 2009) in the Doppler shift of lines in the sunspot spectrum formed at different heights. The oscillations were found to be well pronounced at a level of 100-200 km and decreasing rapidly above it. Efremov et al. (2010) detected periods in the range 40-180 min in wavelengths formed between 190 km and 535 km. Periods of 250 and 480 min were found in the line-of-sight magnetograms from space-borne SOHO/MDI data.

There is also observational evidence of long period oscillations in the radio band. For example, 30-60 minute oscillations have been detected in the intensity difference of two solar radio signals recorded at two close frequencies, 9.67 GHz and 9.87 GHz (Kobrin & Korshunov 1972). Oscillation periods of tens and hundreds of minutes have also been seen as modulation of the microwave emission (Gelfreikh et al. 2006).

Finally, it may be noted that long period oscillations have also been observed in coronal structures, which all have the source of their magnetic fields in sunspots.

For example, Foullon et al. (2004, 2009) detected periods of several hours in extreme ultraviolet (EUV) observations of solar filaments (using SOHO/EIT) and Verwichte et al. (2010) studied transverse oscillations in large coronal loops observed with TRACE and SOHO/EIT, with periods between 24 and 180 min. In addition, Wang et al. (2009) observed propagating disturbances in a fan-like coronal loop, with periods of 12 and 25 min and interpreted them as slow magnetoacoustic waves. From their observations, they deduced the inclination of the magnetic field to the line of sight, the propagation speed of the waves and the temperature close to the loop footpoints.

There is little in the way of theoretical work on the subject of long period sunspot oscillations. One current model is the "shallow" sunspot model of Solov'ev & Kirichek (2008), which treats the sunspot as a structure with a small depth (of about 3 Mm). The structure is then able to oscillate like a raft in water, due to being buffeted by the oscillations present in the surrounding convection zone. The waves continuously strike the structure and when the wave frequency is equal to the natural frequency of the structure, it is in resonance and therefore oscillates at that frequency. However, if the system is nonlinear, the resonance can be produced by a combination of frequencies. Here, we review the work of Solov'ev & Kirichek (2008).

The sunspot is modelled as a cylindrical magnetic flux tube below the level of the Wilson depression and contains a straight magnetic field. The tube has a finite depth of a few Mm and below it, there are diverging flows. To describe the magnetic field in the photospheric region, a magnetic scale height is introduced. Figure 1.11 shows the geometry of the shallow sunspot model.

The cylindrical structure is taken to be in pressure balance with the external plasma and the densities inside and outside the tube are assumed to be equal (but varying with height). A model of the convection zone, provided by Spruit (1974) produced using a mixing length formalism and using observational data to constrain parameters was then used to give values of external pressure, temperature and density. Using these, the dependence of the Wilson depression on magnetic field strength, $\zeta(B)$, is found, for a constant internal temperature. To find a more realistic expression for $\zeta(B)$, the authors used the data of Kopp & Rabin (1992) to find an expression for the dependence of the sunspot's temperature on magnetic field strength and used the model presented in Spruit (1974) to find the expression for $\zeta(B)$,

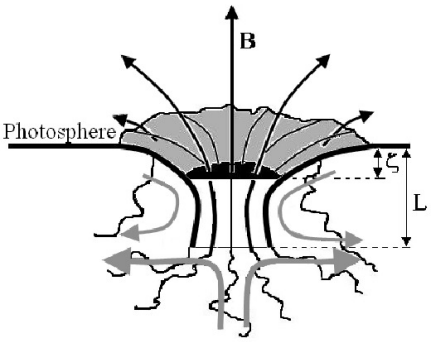

Figure 1.11: The geometry of the shallow sunspot model. Figure courtesy of Solov'ev & Kirichek (2008).

$$\zeta(B) = \frac{0.165(B - B_0)^4}{2 + (B - B_0)^{3.1}}, \tag{1.27}$$

where B_0 is the external magnetic field.

Next, the authors again use the model of Spruit (1974) to find an expression for the density as a function of height, in the uppermost layers of the convection zone,

$$\rho(h) = \rho(0)\left(1 + 2.53h + 1.22h^2 + 3.27h^3\right), \tag{1.28}$$

where the height, h is given in Mm and the photospheric density, $\rho(0) = 3.19 \times 10^{-7}$ g cm^{-3}. The mass in the tube is then given by

$$M(L) = \pi a^2 \int_0^L \rho(h)dh = \rho(0)\pi a^2\left(L + 1.265L^2 + 0.407L^3 + 0.8175L^4\right), \tag{1.29}$$

where a is the radius of the cylinder and L is the height in the photosphere where the flux tube begins to widen (see figure 1.11). This takes into account the mass above the Wilson depression, which appears to sink to the lower boundary of the tube during formation.

The decrease in gravitational potential energy of the system is given by

$$M_f g(L - \zeta), \tag{1.30}$$

where M_f is the mass of gas that sinks from the level of the Wilson depression to depth L. The change in magnetic energy of the system is given by

$$\frac{B^2}{8\pi}\pi a^2(L-\zeta) \tag{1.31}$$

and the two energies are equated for the system to be in equilibrium and a value of $B \approx 2$ kG is found for the equilibrium value of the magnetic field strength. The authors then use this estimate of the magnetic field strength and mass density averaged over the depth to derive the period of a global oscillation of the structure, obtaining a value of $P \approx 90$ min by using the expression

$$\omega = \frac{B}{L\sqrt{4\pi\rho_0}}, \tag{1.32}$$

where B is the magnetic field given above, L is the depth (approximately 3 Mm) and ρ_0 is the mass density averaged over the depth (approximately 3×10^{-6} g cm^{-3}).

In this thesis, two studies of long period oscillations are presented. In the first, we perform both temporal and spatial analysis in order to examine the periods of such oscillations and their spatial coherency. In the second, we make use of a long dataset in order to study the lifetimes of the oscillations during the passage of a sunspot across the solar disk.

1.7 Motivation

The properties of oscillations and waves in any system are dependent on the physical parameters of that system and therefore by studying those waves, we hope to gain insight into the nature of those systems.

The study of sunspots, in particular, is important as those structures are manifestations of the magnetic field. The dynamo mechanism for generating the solar magnetic field is not well understood and by studying oscillatory phenomena in sunspots, we aim to understand the dynamo in more detail. In addition, the magnetic field is observed to permeate all heights in the entire solar atmosphere and therefore connects the layers of the atmosphere, as well as the solar interior. One question that arises concerns the appearance of oscillatory phenomena in different parts of the atmosphere (e.g. long period oscillations in the microwave emission above sunspots and long period oscillations seen in EUV prominences as mentioned in the previous section). Could these be manifestations of the same physical process?

The low frequency oscillations in sunspots are particularly interesting for the following reason. The solar g-modes are known to be low frequency oscillations (see, e.g. Appourchaux et al. 2010), confined to the solar interior. Since the flux tube that forms a sunspot travels through the interior to the surface, perhaps signatures of the g-modes can become trapped in the tube and survive the journey to the surface. It may then be possible to use these as a another probe of the solar interior, in addition to the p-modes.

1.8 Observations

Work presented in this thesis relies on observational data from various instruments. In this section, we briefly describe these instruments and the characteristics of the data used.

1.8.1 Nobeyama Radioheliograph

The Nobeyama Radioheliograph, shown in figure 1.12 (NoRH, Nakajima et al. 1994) is a ground-based radio interferometer, based in Japan and was designed for the study of solar flares and other solar phenomena that occur on short timescales. It consists of 84 antennae that are arranged in a T-shaped configuration and it operates at two fixed frequencies, of 17 and 34 GHz. The instrument produces full disk images of the Sun, with spatial resolutions of 5″ (17 GHz) and 2.5″ (34 GHz) per pixel and a temporal cadence of 1 s (though this may be reduced to 50 ms in some cases). It has been observing the Sun for periods of 8 hr every day since 1992 and has the obvious disadvantage that, since it is ground-based, it cannot observe continuously. NoRH does not directly image the Sun; instead it relies on Fourier reconstruction of correlation signals from antenna pairs.

In radio astronomy, a so-called "dirty image" is obtained by convolving the instrument's "dirty" beam function with the brightness distribution in the sky of the object under observation. The objective, then, is to recover that brightness distribution, using a deconvolution algorithm by using the dirty image and beam. The CLEAN algorithm (Högbom 1974) is the standard for this and repeatedly subtracts the beam function from the brightest element in the dirty image, until either the noise level has been reached or there are no more bright features in the image. This works well on point sources, but not for extended ones. Steer et al. (1984) proposed a modification to deal with extended sources, in which the area of

Figure 1.12: The Nobeyama Radioheliograph. Figure courtesy of NAOJ.

the source is estimated. This is done by finding the peaks in the dirty image and then selecting all points that are above a contour set at a fraction of the peak level. In this work, the Koshix algorithm for NoRH is used for image synthesis (since it is best suited to diffuse sources), which is the application of the Steer algorithm to NoRH images (Koshiishi 2003).

The emission from sunspots observed with NoRH is produced by the gyroresonant mechanism. The electrons in the plasma are acted upon by the Lorentz force and are therefore accelerating about the magnetic field lines and hence, they emit radiation. This radiation is observed when the frequency (which is a low harmonic of the cyclotron frequency, nf_{ce}, where $n = 2, 3$ and $f_{ce} = \frac{\omega_{ce}}{2\pi}$) matches the operating frequency of the instrument. Naturally, the amount of the emission depends on the number density of electrons in the plasma and is also related to the magnetic field strength, through ω_{ce}. The modulation of the emission can therefore occur in two ways. First of all, the plasma may be compressed, in which case the density in the emitting layer varies. Secondly, the magnetic field may vary and the emitting layer is displaced vertically and experiences regions of higher or lower density plasma (due to the gravitational stratification).

1.8.2 Hinode

Hinode, shown in figure 1.13, is a Japanese spacecraft that was launched in 2006 and designed to answer questions about how magnetic fields are generated, transported and dissipated on the Sun. It consists of a suite of three instruments: the

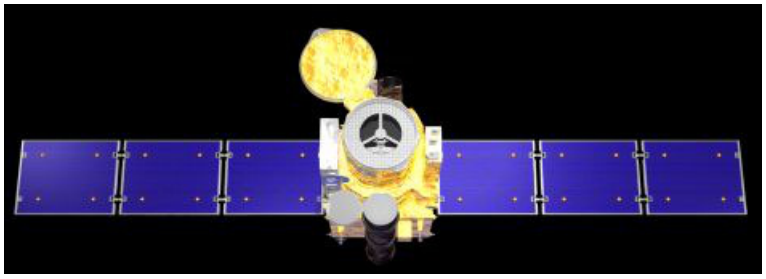

Figure 1.13: The Hinode spacecraft. Figure courtesy of NAOJ.

Solar Optical Telescope (SOT), the X-Ray Telescope (XRT) and the EUV Imaging Spectrometer (EIS), observing the Sun at various wavelengths from the photosphere up to the corona. Of these, only SOT is used in this thesis and that instrument is described next.

The Solar Optical Telescope (Tsuneta et al. 2008) has a primary mirror with a diameter of 50 cm and can produce images in six wavelengths in the range $\lambda =$ 388-669 nm, which cover the photosphere and chromosphere. For these images, a maximum spatial resolution of $0.054''$ per pixel can be achieved, with a maximum temporal cadence of 3.4 s. In addition to direct imaging of solar features, SOT can produce dopplergrams and magnetograms, also in six wavelength bands. The instrument does not produce full disk images, but instead tracks certain features on the disk (e.g. active regions). In addition, due to orbital constraints, it is only possible to achieve uninterrupted observations for a period of around 8 months per year.

1.8.3 Radio and optical emission mechanisms

In this section, we describe the emission mechanisms for the radio and visible light signals observed with NoRH and Hinode/SOT that are used in this thesis and how these are modulated by the MHD wave modes.

Gyroresonance emission

In the highly ionised plasma in the upper regions of the solar atmosphere, emission from electrons may be due to bremsstrahlung, in which the electrons are decelerated due to their interactions with ions. However, when the plasma contains a strong magnetic field (as in regions above sunspots), the electrons are confined to their

Larmor orbits around the field and the dominant emission mechanism (when the electrons are nonrelativistic) is the gyroresonant one.

There are two kinds of electromagnetic waves in the plasma which can interact with the charged particles gyrating around the magnetic field, which have their wave vector perpendicular to the field. The first is the ordinary (O) mode, which gyrates around the magnetic field in the same sense as that of the ions and the other is the extraordinary (X) mode, which gyrates in the sense of the electrons. Therefore, the latter interacts strongly with the electrons, accelerating them and thus producing the emission. Gyroresonant emission is thus strongly polarised in the sense of the X mode (right circularly polarised, in the case of the magnetic field pointing towards the observer) and since radio instruments detect both circular polarisations separately, this is easily tested (e.g. Shibasaki et al. 1994).

If both modes are perfectly circularly polarised, the opacity produced by the gyroresonant emission is given by (White & Kundu 1997)

$$\tau_{x,o}(s,f,\theta) = 0.0133\frac{n_e L_B(\theta)}{f}\frac{s^2}{s!}\left(\frac{s^2\sin^2\theta}{2\mu}\right)^{s-1}\left(1-\sigma|\cos\theta|\right)^2, \tag{1.33}$$

in which $\mu = \frac{m_e c^2}{k_B T}$, n_e is the number density of electrons, L_B is the scale length of the magnetic field, along the line of sight, θ is the angle between $\mathbf{B}$ and the line of sight, s is the harmonic number of the cyclotron frequency and σ is -1 for the X mode and 1 for the O mode. The measured brightness temperature, T_B is found by computing the integral (e.g. Aschwanden 2009, pg. 228)

$$T_B\left(f,\sigma\right) = \int T(z)\exp\left[-\tau_{x,o}(z)\right]\alpha_{x,o}(z)\,dz, \tag{1.34}$$

in which $T(z)$ is the temperature profile of the plasma with height z and $\alpha_{x,o}(z)$ is the absorption coefficient for the X and O modes. The brightness temperature therefore depends on the number density of electrons and the magnetic field strength B (through $L_B = \frac{B}{\nabla B}$). In the cylindrical geometry adopted to model flux tubes associated with sunspots, the slow mode is associated with variations in the plasma density. In principle, the sausage mode may modulate the intensity as well, but this may not be observed if the pixel size is large.

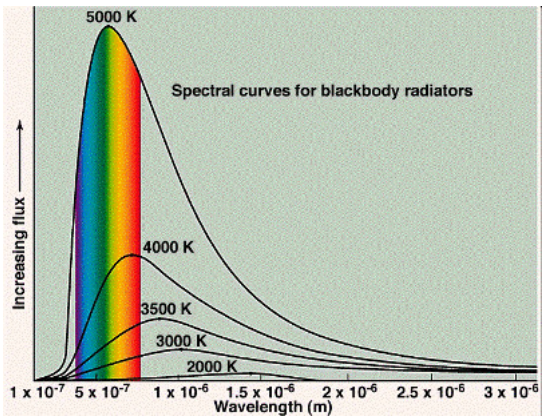

Figure 1.14: The blackbody spectrum for several values of the temperature of the blackbody. Figure courtesy of S. Sobottka, University of Virginia.

Optical emission

In the 1800s, Wollaston conducted an experiment in which he passed light through a prism and observed that instead of having a continuous spectrum of colours, dark lines could be seen at certain wavelengths. These were wavelengths at which the light had been absorbed (hence the intensity was lower) and later came to be known as the Fraunhofer lines.

Earlier on, the theory of blackbody radiation had been developed. A blackbody is one that absorbs all light incident on it and radiates it with a continuous spectrum, whose shape varies with temperature, as shown in figure 1.14. It was thus seen that the solar spectrum deviated from a blackbody and Kirchoff suggested the following: the hot and dense gas of the solar interior produced a continuous spectrum and cooler gas in front of it (i.e. between the Sun and the observer) produced the absorption lines.

With the advent of quantum mechanics, it became possible to understand the nature of the absorption lines. Bohr suggested that electrons bound to atoms had so-called "energy levels" that corresponded to different orbits of the electron around the nucleus. These orbits were ones in which the angular momentum of the electron assumed integer multiples of some fundamental value (i.e. they were quantised). When in one of these levels, the electrons neither emit nor absorb radiation. However, these processes occur when electrons make transitions between levels. In particular, if an incident photon has energy corresponding exactly to

the difference between two levels, an electron can make a transition from the lower level to the higher one. The various elements present in the solar atmosphere have different sets of energy levels and therefore absorption occurs at various wavelengths. In this thesis, two absorption lines are used: Ca II H, at a wavelength of 396.8 nm, which comes from singly ionised calcium and G-band, with a wavelength of 430.5 nm, which is a line in the molecule CH. In higher regions of the solar atmosphere (such as the solar corona), the plasma is hotter and photons can be emitted by an electron making a transition from a higher to a lower energy level. This can be caused by collisions between free particles and atoms, or by electrons becoming bound to the atoms. Since the absorption concerns interactions between photons and atoms, it suggests that it is proportional to the density of the plasma. Therefore, the waves that can modulate the intensity are those that can vary the density. Again, the candidates is the slow mode.

1.9 Structure of the thesis

This thesis is structured in the following way: chapter 2 details the techniques used to analyse the observational data studied in this thesis and chapter 3 begins the original research with a study of long period oscillations with the Nobeyama Radioheliograph. A complementary study on the lifetimes of such long period oscillations is presented in chapter 4. In chapter 5, the focus is shifted to short period oscillations and the investigation focuses on the spatial structure of the 3 minute oscillations. Finally, we summarise the work presented in the thesis and provide some discussion on further work.

Chapter 2

Methods for data analysis

The work presented in this thesis concerns the detection of periodic components in time series and the distribution of the properties of those components in space. Several methods for extracting this information from the data are used and in this chapter, we present them.

2.1 Temporal information

2.1.1 The periodogram

The most basic tool for detecting periodic signals within time series is the power spectrum, which can be obtained by computing the Fourier transform of the time series. The spectrum is given by

$$P(\omega) = \left| \sum_j X(t_j) \exp(-i\omega t_j) \right|^2 = \left[\left(\sum_j X_j \cos \omega t_j \right)^2 + \left(\sum_j X_j \sin \omega t_j \right)^2 \right], \tag{2.1}$$

where X is the time series for which the spectrum is desired and the observation times are usually taken to be evenly spaced. It is evaluated at the natural frequencies, $\omega_n = \frac{2\pi n}{T}$, in which T is the time length of the observations and n is the set of integers between $-\frac{N_0}{2}$ and $\frac{N_0}{2}$, with N_0 the number of data points. For even sampling, the values of $P(\omega)$ are exponentially distributed if the signal is pure Gaussian noise (e.g. Groth 1975). This is important because if the data are noisy, the spectrum will also be noisy and may contain a peak that suggests a periodic signal is

present. The user therefore wants to know the probability that a peak could be produced due to the noise.

Here, we use the Lomb-Scargle periodogram (Scargle 1982), which coincides with the Fourier power spectrum but does not provide any phase information. The idea behind it is to compute the spectrum of a signal in which the times need not be evenly spaced, yet the spectrum retains the simple statistical behaviour alluded to above. It is defined as

$$P_X(\omega) = \frac{1}{2}\left\{\frac{\left[\sum_i X_i \cos\omega\left(t_i-\tau\right)\right]^2}{\sum_i \cos^2\omega\left(t_i-\tau\right)} + \frac{\left[\sum_i X_i \sin\omega\left(t_i-\tau\right)\right]^2}{\sum_i \sin^2\omega\left(t_i-\tau\right)}\right\}, \tag{2.2}$$

where τ is defined by

$$\tan\left(2\omega\tau\right) = \frac{\left(\sum_i \sin 2\omega t_i\right)}{\left(\sum_i \cos 2\omega t_i\right)}. \tag{2.3}$$

The periodogram defined in this way has the exponential distribution of $P_X(\omega)$ for a pure Gaussian noise signal, as in the even sampling case. In addition, equation 2.3 makes the periodogram invariant under a time shift. Letting $Z = P_X(\omega)$ and considering the particular value of Z corresponding to the maximum power in the periodogram, the probability that Z is due to chance is given by

$$P\left\{Z > z\right\} = 1 - \left[1 - \exp\left(-z\right)\right]^N, \tag{2.4}$$

where N is the set of independent frequencies over which Z is the maximum power. We call $P\left\{Z > z\right\}$ the false alarm probability and would like its value to be small, so that we can be confident that the maximum peak is not due to chance. A threshold on the power value z_0 for which the maximum power must exceed can be found from equation 2.4. Letting $p_0 = P\left\{Z > z\right\}$, we have

$$z_0 = -\ln\left[1 - \left(1 - p_0\right)^{\frac{1}{N}}\right]. \tag{2.5}$$

According to Horne & Baliunas (1986), z_0 has to be normalised to the variance of the signal and typically, we choose $p_0 = 0.01$, corresponding to 99% confidence in the presence of the periodicity. Another advantage of the periodogram is that, unlike traditional Fourier analysis, it can be used when the sampling times are unevenly spaced.

2.1.2 Wavelets

The periodogram, while a useful technique, only gives information about which frequencies are important in the time series; it does not give any information about the temporal localisation of the oscillations. The wavelet method is one that allows a time series to be decomposed in both time and frequency. The windowed Fourier transform is an alternative, but the window width must be chosen differently for different spectral components. The wavelet method has the advantage that this is done automatically. The wavelet transform is defined as

$$W_n(s) = \sum_{n'=0}^{N-1} X_{n'} \psi^* \left[\frac{(n'-n)\delta t}{s} \right], \tag{2.6}$$

where n corresponds to a time index and s is the wavelet scale, corresponding to a frequency. It is therefore a convolution of a signal X (which is evenly sampled) with a wavelet function ψ and the idea is that when a feature in the signal matches with the wavelet function, a large contribution to the sum is produced. This transform can be computed over a variety of times and scales and therefore one can see how the amplitude of the features varies with those parameters. The function ψ must have zero mean and be localised in both the time and frequency domains in order to be "admissible" as a wavelet. In this work, the Morlet wavelet is used, which is defined as

$$\psi(\eta) = \pi^{-\frac{1}{4}} e^{i\omega_0 \eta} e^{-\frac{\eta^2}{2}}, \tag{2.7}$$

where η localises the oscillation in time and ω_0 is a dimensionless frequency chosen as $\omega_0 = 6$ to satisfy the admissibility condition. The wavelet is shown in both time and frequency space in figure 2.1.

The wavelet transform is computed over a range of scales and times and then a wavelet power spectrum can be defined as $|W_n(s)|^2$, in an analogous way to the Fourier power spectrum, showing the variation in power with frequency and time. When the wavelet power spectrum is displayed, usually a curve known as the cone of influence is displayed, which displays the region in which edge effects are important. In practice, the Fourier transform is used to compute the wavelet transform of a signal at each scale and this assumes that the data are strictly periodic. In a finite length signal, this is not the case and therefore errors occur at the ends. In order to limit these effects, the signal is usually padded with zeros at the ends before

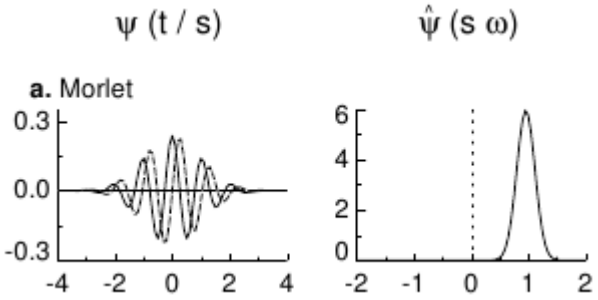

Figure 2.1: The Morlet wavelet in the time domain (left panel. The solid line is the real part and the dashed line the imaginary part) and in the frequency domain (right panel). Figure from Torrence & Compo (1998).

computing the wavelet transform. It is also useful to define the global wavelet spectrum, in which the time average of the power at each frequency is found and can be compared with the periodogram. A more detailed description of wavelets can be found in Torrence & Compo (1998).

2.1.3 Empirical mode decomposition

Fourier analysis, together with other methods based on harmonic decomposition (e.g. the periodogram and wavelets), are not without problems. For example, any large scale trend in the signal must be removed before performing Fourier analysis, otherwise the spectrum will be dominated by the trend. Also, it requires that signals contain strictly periodic components. In real signals, this is rarely the case and oscillatory components can be modulated by non-stationary and nonlinear effects. Wavelets allow us to study non-stationary signals and analyse frequency modulation, but one disadvantage of that method is that the time resolution is limited by the finite width of the wavelet function. Also, these techniques cannot perform well on periodic but significantly anharmonic signals.

Empirical mode decomposition (EMD, Huang et al. 1998) was designed for use with nonlinear and non-stationary signals and assumes that the signal is a sum of intrinsic oscillations (which are usually referred to as intrinsic mode functions, or IMFs) that may have varying amplitude and frequency. As such, it is an excellent method for studying frequency modulation. In addition, it is not necessary to remove a trend component from the data before applying the technique - being an adaptive

filter, EMD effectively removes the trend. The intrinsic mode functions found do not need to be harmonic oscillations, which allows the technique to be used to investigate the anharmonicity of oscillations in a signal. Applications of EMD in solar physics can be found in Komm et al. (2001), Terradas et al. (2004) and Nakariakov et al. (2010).

The IMFs are found for a signal, $X(t)$, by a sifting process. First, the local maxima are identified and are connected with a cubic spline. This is repeated for the local minima and the mean of the envelope created by the connected maxima and minima, $m(t)$, is found. This mean is subtracted from the signal to give

$$h_1(t) = X(t) - m(t), \tag{2.8}$$

where $h_1(t)$ will be an IMF, provided that it satisfies the following two conditions:

1. The number of extrema and number of zero crossings must differ by at most one.

2. The mean of the upper and lower envelopes must be zero at all times.

The first condition means that the IMFs contain a narrow range of frequencies and the second means that the oscillations have zero mean. Once the mean has been subtracted from the original signal, the residual signal, $h_1(t)$ is used as input to the EMD procedure and the process is repeated until all IMFs are found. Huang et al. (1998) proposed the Hilbert spectrum for the visualisation of these components, but in this thesis, we make use of the standard wavelet power spectrum, because it is easier to interpret than the Hilbert spectrum.

2.1.4 The Hilbert transform

The Hilbert transform is designed to produce a phase shift of $\frac{\pi}{2}$ in a periodic signal. For example, if $\mathcal{H}$ denotes the Hilbert transform, then

$$\mathcal{H}\left(\cos\omega_0 t\right) = \sin\omega_0 t. \tag{2.9}$$

It is implemented as a multiplication in the frequency domain, so that the Fourier representation of equation 2.9 is given by

$$\frac{1}{2}\left[\delta(\omega-\omega_0)+\delta(\omega+\omega_0)\right]H(\omega) = \frac{1}{2i}\left[\delta(\omega-\omega_0)-\delta(\omega+\omega_0)\right], \tag{2.10}$$

where $\delta(\omega)$ is the Dirac delta function and the terms involving $\delta(\omega)$ on the left and right hand sides are the Fourier transforms of $\cos\omega_0 t$ and $\sin\omega_0 t$, respectively. By the convolution theorem, multiplication in the frequency domain is a convolution in the time domain. It follows, then, that the Hilbert transform of a signal $x(t)$, $\mathcal{H}[x(t)]$ is a convolution of $x(t)$ with a function $h(t)$:

$$\mathcal{H}[x(t)] = \int_{-\infty}^{\infty} x(t-s)\,h(s)\,ds = \int_{-\infty}^{\infty} x(s)\,h(t-s)\,ds, \tag{2.11}$$

where $h(t)$ is the inverse Fourier transform of $H(\omega)$. The function $H(\omega)$ is given by

$$H(\omega) = \begin{cases} -i, & \omega > 0 \\ 0, & \omega = 0 \\ i, & \omega < 0 \end{cases} \tag{2.12}$$

and it can be shown that $h(t) = \frac{1}{\pi t}$. The final form of equation 2.11 is then

$$\mathcal{H}[x(t)] = P\,\frac{1}{\pi}\int_{-\infty}^{\infty} \frac{x(s)}{t-s}\,ds, \tag{2.13}$$

where P denotes the Cauchy principal value. Equation 2.13 is the "forward" Hilbert transform and to obtain $x(t)$, $\mathcal{H}[x(t)]$ must be convolved with $-h(t)$. Unlike the Fourier transform, the Hilbert transform of a signal is also in the time domain. In addition, since integration is a linear operation, if a signal contains several periodic components, each of them will be phase shifted by $\frac{\pi}{2}$.

2.2 Spatial information

The data from the observational instruments used in this thesis come in the form of two dimensional images, showing the distribution of intensity in space. Two main kinds of techniques are used for extracting spatial information from the images.

2.2.1 Mapping

To investigate the spatial distribution of the oscillations seen in the sunspots, the method of periodmapping, developed by Nakariakov & King (2007), is used. This method has been applied to flaring data from NoRH by Inglis et al. (2008), who used the technique to deduce coherency of quasi-periodic pulsations in different segments of a flaring loop.

For each pixel in the datacube, we generate the time series (by simply taking the values for that pixel along the time dimension of the datacube) and calculate the power spectrum. The frequency of the highest peak in the spectrum is then assigned to this pixel in the periodmap. The periodmap is then a 2D map of frequencies corresponding to the dominant frequencies for each pixel in the images. Nakariakov & King (2007) used the traditional Fourier spectrum to determine the frequency assigned to each pixel in the periodmap. In this thesis, we use the global wavelet spectrum instead, since it is smoother than the Fourier spectrum. In addition, we also make use of power, correlation and lag maps. The first are 2D maps of the maximum global wavelet power in a prescribed frequency range for the corresponding pixel time series, the second show the maximum correlation coefficient, $C_{xy}(\tau)$ (for a given lag, τ) of the time series of each pixel with one particular pixel chosen as a reference pixel and the third show the time lag at which the correlation coefficient was maximal, over a given range of lags. The correlation coefficient is given by

$$C_{xy}(\tau) = \frac{1}{\sigma_x \sigma_y} \sum_{i=0}^{N-\tau-1} (x_{i+\tau} - \mu_x)(y_i - \mu_y), \tag{2.14}$$

where N is the number of points in the signal and μ_j and σ_j are the means and standard deviations of the signals (with $j = x, y$), respectively. The power maps allow us to see in which pixels the oscillations are strongest and the correlation and lag maps show how in phase oscillations in a particular frequency band are over the region.

2.2.2 Otsu thresholding

Sometimes, it may be necessary to select a region of interest (ROI) in an image automatically and the Otsu thresholding method (see, e.g. Otsu 1979; Gonzalez & Woods 2008) is one that allows this. This is used in chapter 3 below, where the sunspot region is seen to vary in size between images.

The idea, first of all, is to apply a threshold, T, to the images such that any pixels with an intensity, $I < T$ will be classed as the background and those for which $I \geq T$ are classified as the ROI. One first of all constructs the normalised histogram of the image, in which each element is the probability, p_I of finding that particular intensity in the image and p_I is given by

$$p_I = \frac{n_I}{N}, \tag{2.15}$$

where n_I is the number of pixels with intensity I and N is the total number of pixels in the image. The distribution should be bimodal, with one mode corresponding to pixels in the background and the other to pixels in the ROI. The objective is then to choose a threshold on the intensity that lies between the two modes. One computes the between-class variance for all intensity levels i,

$$\sigma_b^2(i) = p_B p_R \left(\mu_B - \mu_R\right)^2, \tag{2.16}$$

where p_B and p_R are the probabilities of the background and ROI classes occurring in the image and μ_B and μ_R are the means of the pixels in those classes. Then the threshold T is chosen as the value of i which maximises σ_b. It can be seen that $\sigma_b(i)$ depends on the difference between the class means for the given intensity. When the class means are further apart, $\sigma_b(i)$ is larger, showing that it is a measure of the separability of the classes. Another parameter, the separability parameter, $\eta(i)$ is given by

$$\eta(i) = \frac{\sigma_b^2(i)}{\sigma^2}, \tag{2.17}$$

where σ^2 is the variance of the image. $\eta(i)$ is used as a measure of how good the chosen threshold is, since maximising $\eta(i)$ is equivalent to maximising $\sigma_b(i)$.

The IDL routines used for the periodogram, periodmapping and empirical mode decomposition were written by J. Wilms, V. M. Nakariakov and D. Stone, respectively. The routine to perform Otsu thresholding was written by the author of this thesis, using the algorithm given in Gonzalez & Woods (2008).

Chapter 3

Long period oscillations in sunspots

3.1 Introduction

Oscillatory processes observed in sunspots have attracted attention for several decades (for a comprehensive review, see, e.g. Bogdan 2000). Such oscillations are usually placed into one of four categories: (a) umbral chromospheric oscillations with a period of 3 minutes, thought to be slow magnetoacoustic waves (e.g. Zhugzhda 2008; Botha et al. 2011); (b) umbral photospheric oscillations with a period of 5 minutes, which may be a response to driving by the well known 5 minute photospheric acoustic oscillations (Thomas et al. 1984); (c) long period oscillations (of the order of hours) (e.g. Efremov et al. 2007; Goldvarg et al. 2005); (d) ultra-long period (torque or torsional) oscillations of sunspot umbrae, with periods of several days (Gopasyuk 2004).

So far, most of the work on sunspot oscillations has been focused on the first two, short period categories above. However, long period sunspot oscillations are interesting for a number of reasons, in particular because of their possible association with the eigenmodes of the sunspot magnetic flux tube, the dynamical processes in the solar interior, including the generation and transfer of the magnetic field, and the possible role these oscillations play in solar coronal dynamics. For example, Sych et al. (2009) observed 3 minute quasi-periodic pulsations in flares near a sunspot and suggested that the energy in the 3 minute sunspot oscillations could leak along the loops associated with the active region and periodically trigger solar flares.

Table 3.1: Summary of data analysis.

	AR10105	AR10330	AR10673
Start date	10-Sep-2002 22:45	08-Apr-2003 22:45	21-Sep-2004 22:45
End date	11-Sep-2002 06:29	09-Apr-2003 06:29	22-Sep-2004 06:44
Start location	(-570, -212)″	(-170, 215)″	(115, -340)″
Field of view size	35″ × 35″	40″ × 40″	35″ × 35″
Cadence	10 s	10 s	10 s

In this chapter, we study long period sunspot oscillations in the microwave emission, utilising both time and spatial information. The chapter is organised as follows: in section 3.2, we present the data used; section 3.3 details our analysis (subsections 3.3.1 to 3.3.4 describe the analysis of time signals from the sunspots, while subsections 3.3.5 and 3.3.6 describe the analysis of time signals from the quiet Sun and spatial analysis, respectively) and in section 3.4, we present an attempt at investigating the oscillations in optical wavelengths (with Hinode/SOT) and microwave emission. Finally, in section 3.5, we discuss and interpret our results.

3.2 Observations

We analysed three sunspots that were observed for periods of about 8 hours with the Nobeyama Radioheliograph (NoRH, see section 1.5.1), at a frequency of 17 GHz. The sunspots were the leading sunspots of active region AR10330 (08 April 2003 22:45 - 09 April 2003 06:29), active region AR10105 (10 September 2002 22:45 - 11 September 2002 06:44) and of active region AR10673 (21 September 2004 22:45 - 22 September 2004 06:44). All three sunspots were part of bipolar groups that had different McIntosh classifications (McIntosh 1990): AR10330: Cko, AR10105: Fki and AR10673: Dho.

Figure 3.1 shows white light images of active regions AR10105, AR10330 (obtained with SOHO/MDI) and AR10673 (obtained with the Big Bear Solar Observatory). Table 3.1 summarises the observational details for these sunspots. As described in section 1.8.1, the measured emission is likely to be generated by the gyroresonant mechanism.

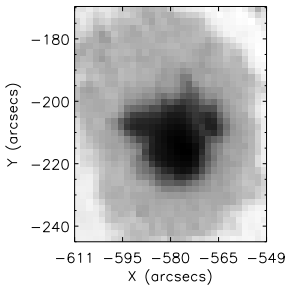

(a) MDI image of AR10105.

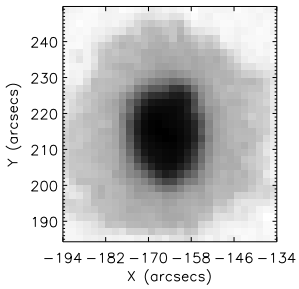

(b) MDI image of AR10330.

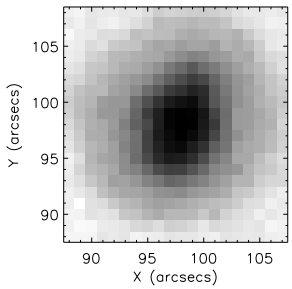

(c) BBSO image of AR10673.

Figure 3.1: White light images of the sunspots studied in this chapter.

3.2.1 Data generation

Partial disk images, measuring the radio brightness temperature were obtained from NoRH for the 3 considered sunspots and time series were generated from these by integrating the signal over the field of view (FOV). Figure 3.2 shows the time series of the emission intensity from the analysed sunspots. The mean brightness is not influenced by the changing beam shape throughout the day, so this was not taken into account when generating the time series.

Since the observation periods were quite long, it was necessary to track the sunspots through their passage across the solar disk. First, the sunspots were matched with their active region numbers by obtaining a full disk image for the start of the observing period and then adding the active region numbers to the image using SolarSoft's NOAA active region database and its associated routines (`get_nar` and `oplot_nar`). The AR numbers found were solely to identify the sunspots studied and were not used in any other way (e.g. to determine their positions on the solar disk). The centre of the radio sunspot was then found (see Table 3.1) at the start of the observing period, as the position of the maximum of the microwave emission. These coordinates were converted to heliographic longitude and latitude and the change in longitude in one time step (i.e. 10 seconds) due to differential rotation was found for the given latitude. The position at the next time step was given by $(\lambda, \theta + \Delta\theta)$, where λ is the latitude, θ is the original longitude and $\Delta\theta$ is the change in longitude. The new coordinates were then converted back to arcseconds. Images were then synthesised using the position as the centre of the field of view. The size of the field of view was chosen so as to minimise the amount of quiet Sun in the images. Since there were no off-limb flares during the observations, any possible jitter of the radio image was neglected.

3.3 Analysis

3.3.1 Trend removal and filtering

It is evident from figure 3.2 that there is a large scale trend in all the datasets due to the motion of the Sun across the sky during the observing period, long period (e.g. daily variation of the Earth's ionosphere) and other ultra-long period processes. To remove the trend, we fitted a 4th order polynomial to the data and then subtracted it from the original signal. Following this, we filtered out any oscillations with 3

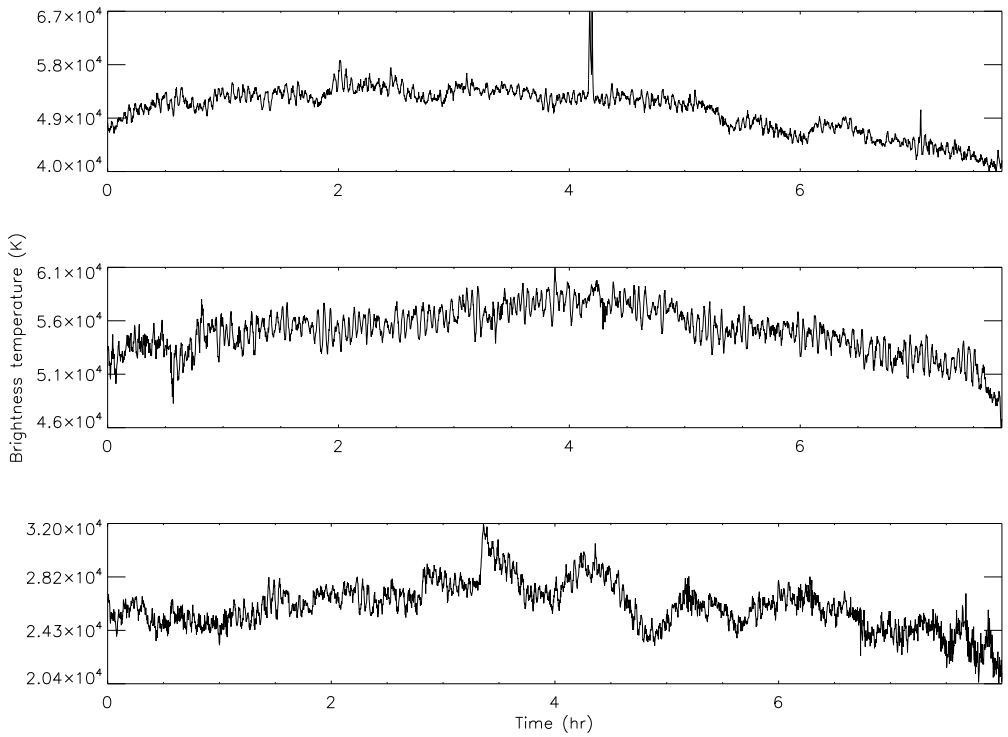

Figure 3.2: Original time series of microwave intensity generated from partial disk radio images for AR10105 (top), AR10330 (middle) and AR10673 (bottom), as observed by the Nobeyama Radioheliograph, at a frequency of 17 GHz.

periods or fewer ($P \geq 145$ min) from the Fourier spectrum of the signal.

Also evident in the time series for AR10105 is a large spike, which is perhaps artificial or a short flare. Since we were only interested in the long period oscillations in the data, the spike was removed. This was done by finding the mean of 5 points to the left of the region and then replacing the points in the region with this mean.

3.3.2 Period analysis

In order to investigate the various frequencies present in the datasets, we employed both the periodogram technique and wavelet analysis[1], as described in chapter 2. Figure 3.3 shows the Lomb-Scargle periodograms and wavelet power spectra computed from the detrended data. We see that in all three periodograms, there is power above the 99% significance level (calculated according to Horne & Baliunas 1986) around frequencies of 5-6 mHz, corresponding to the well-known 3 minute chromospheric umbral oscillations. There are several low frequency peaks in all the datasets and for AR10105 and AR10673, there is significantly more power in the low frequency oscillations than in the 3 minute oscillations.

For the wavelet analysis, the Morlet wavelet was chosen, because of its good performance in the study of oscillatory signals. The 99% significance level has been estimated using the subroutine provided by Torrence & Compo (1998). In figure 3.3, we have only shown power that is above this level. In addition to computing the wavelet power spectrum for each time signal, the global wavelet spectrum was also computed and these are shown in figure 3.3, overlaid on the periodograms. These spectra show that AR10105 and AR10330 have two low frequency peaks and possibly that the same is true of AR10673, but the two peaks blend together and are not resolved clearly. In the wavelet spectrum for AR10330, the region of highest power is seen to be outside the cone of influence. This appears to be associated with a relatively large drop in brightness temperature in the signal, which is perhaps artificial.

All three applied techniques (periodogram, wavelet and global wavelet) show the presence of coinciding spectral peaks, corresponding to the 3-min oscillations and longer period peaks (18-80 min). The 3-min peaks have the same spectral position. The long periods we find have different ranges for each sunspot and are as follows: AR10105: $P_1 = 57 \pm 12$ min, $P_2 = 31 \pm 6$ min; AR10330: $P_1 = 88^{+16}_{-21}$ min,

[1]The software used for wavelet analysis was provided by C. Torrence and G. P. Compo and can be found at http://paos.colorado.edu/research/wavelets.

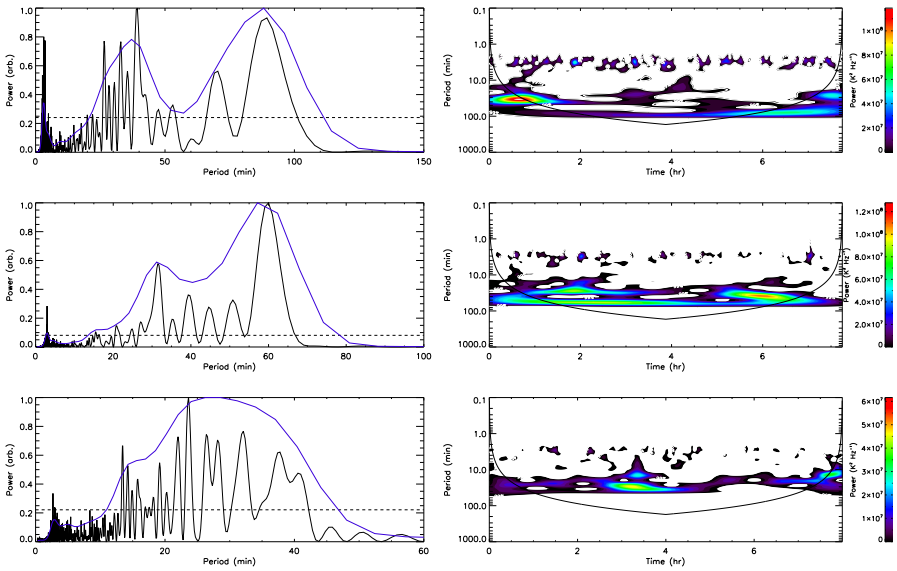

Figure 3.3: The Scargle periodograms and Morlet wavelet power spectra for AR10330 (top row), AR10105 (middle row) and AR10673 (bottom row) time series. The left panels show the periodograms (thin lines) and global wavelet spectra (thick lines). The dashed lines indicate the 99% significance level for the periodograms.

$P_2 = 37^{+8}_{-11}$ min; AR10673: $P_1 = 27 \pm 16$ min, $P_2 = 16 \pm 4$ min. The errors have been calculated by using the width of the peaks at half their maximum spectral amplitude.

3.3.3 Significance testing

We would like to calculate the probability that the highest peak in our power spectrum is due to the presence of harmonic oscillations, i.e. not due to chance. Two methods for estimating this probability are used. First of all, as described in section 2.1.1, we can compute the power threshold for a given false alarm probability, above which we are confident of the presence of the oscillations. In figure 3.3, the false alarm probability chosen was $p_0 = 0.01$ and according to the estimation of the corresponding power threshold, the long period sunspot oscillations are statistically significant.

Also, we make use of a significance test based on Fisher's method of randomisation (see, e.g. Linnell Nemec & Nemec 1985) in order to confirm our results

from the periodogram analysis. The main reason for doing this is that the test is distribution independent, whereas other techniques implicitly assume a certain model for the statistical distribution.

Suppose first that the signal does not contain a periodic component. Then, the measurements $I(t_1), I(t_2), \ldots, I(t_n)$ are independent of the observation times (the t_i). If that is the case, there are $n!$ permutations of the signal, where n is the number of measurements. Typically, n is large and as such, it is impractical to perform all $n!$ permutations. Due to this limitation, we choose to perform $m \ll n!$ such permutations and usually choose $m \geq 100$. When these permutations are performed, the power spectra of the randomised signals are computed and we count the number of times the largest peak in these power spectra have amplitudes greater than, or equal to, the largest peak in the original spectrum.

The probability, p, of the highest peak in the spectrum occuring by chance is then given by

$$p = \frac{m_p}{m}, \tag{3.1}$$

where m_p is the number of times a peak in the spectrum of a randomised signal was found to have an amplitude greater or equal to that of the highest peak in the spectrum of the original signal. The detection probability is then given by $(1 - p)$. It should be noted that both p and $(1 - p)$ are only estimates of the true probabilities and this is due to the limitation on the number of permutations that can be performed.

The noise model used was white noise. A signal containing a only a sinusoidal component (shown in figure 3.4 top panel) was permutated 1000 times and each time, the power spectrum was computed. The average spectrum is shown in the bottom panel of figure 3.4 and is flat, like that from a white noise process.

The Fisher randomisation method was applied to all three datasets with $m = 200$. We performed m random permutations 1000 times for each dataset (i.e. 1000 random sets of 200 permutations were performed) and for all 1000 experiments, the estimated value of p was found to be less than 0.1%, i.e. there was almost no chance that the detected periods corresponding to the highest spectral peaks (i.e. 88 min for AR10330, 57 min for AR10105 and 27 min for AR10673) occurred due to chance.

To establish the significance of the other spectral peaks, the time series were

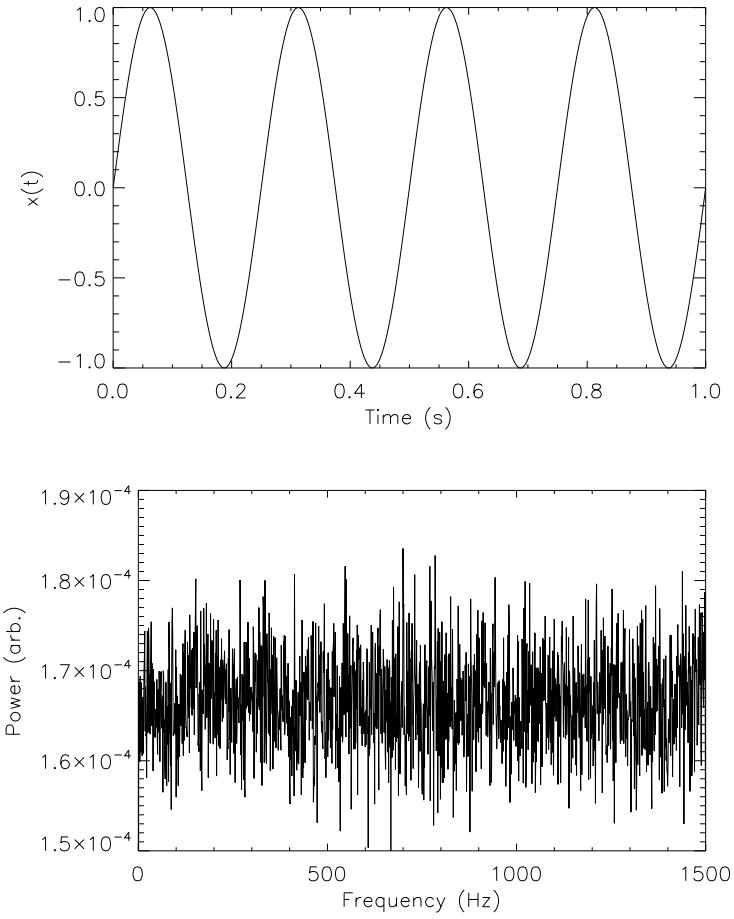

Figure 3.4: Top: the harmonic signal that was permutated 1000 times. Bottom: the average power spectrum computed from 1000 permutations of the signal in the top panel.

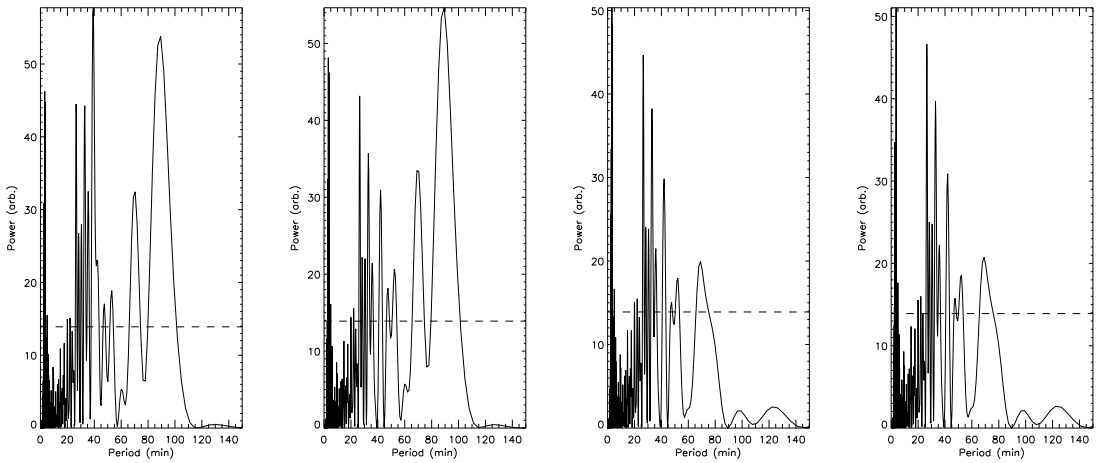

Figure 3.5: The original periodogram for AR10330 (left panel), along with the first three iterations of the process to remove the highest spectral peak (from left to right). The dashed horizontal lines show the 99% significance levels.

filtered iteratively to remove the highest peak. The filtering was performed in the time domain, by computing

$$I'(t) = I(t) - (d_0 + d_1 \sin \omega t + d_2 \cos \omega t)\,, \tag{3.2}$$

where ω corresponds to the angular frequency of the highest peak and the d_i were computed as described in Ferraz-Mello (1981). This process was continued until there were no peaks above the 99% significance level in the periodogram. The original periodogram and the first three iterations of this process are shown in figure 3.5 for AR10330.

3.3.4 Application of empirical mode decomposition

The EMD method was described in section 2.1.3 above and here, it is used to confirm our results derived from the other methods. The technique was applied to all three datasets, after filtering the signals to contain only frequencies in the range 0-8 mHz, to include the 3 minute oscillations and remove high frequency noise. The filtering was performed on the Fourier transform of the signal (rather than the periodogram), since filtering of both phase and amplitude spectra are needed and the filter was a boxcar function. For AR10673, 12 components were found and 10 components were

found for both AR10105 and AR10330.

Figure 3.6 shows the three longest period intrinsic modes found by the EMD for AR10105, two of which are oscillatory and the third is the trend component. Also shown is the global wavelet spectrum for the two oscillatory components. The two oscillatory components are the most significant components (i.e. they have the largest amplitudes, besides the daily trend) and wavelet power spectra were computed for them. It is clear that the periods are persistent throughout the observations and remain stable. Also, EMD analysis shows that the intrinsic modes of the analysed signals are quasi-monochromatic and harmonic. The amplitudes of the oscillatory components are seen to decrease around local noon (near $t = 4$ hr), but this cannot be explained by a change in the beam shape, which does not affect the mean brightness temperature.

These features coincide with those found in the significant components of the other signals, which is consistent with the previous results. The global wavelet spectrum in the bottom right of figure 3.6 shows the same periodicities as those shown in figure 3.3. The noise in NoRH has not been taken into account in this study. To study it, one could investigate the signals from sky (i.e. off-Sun) pixels in the images, since there are no sources of 17 GHz radiation there.

3.3.5 Quiet Sun signals

As a final test to determine whether the long period oscillations seen in the sunspot time series were real, we investigated the same time variations of the signals of the quiet Sun. One region, with a starting location of (-170, -500)″, which did not contain any bright microwave features, was studied for the same observation period as for AR10330 and with the same time cadence.

The signals for AR10330 and the quiet Sun region were filtered to contain only long period spectral components. A gaussian filter was used for both signals, with a bandpass of 0.35-0.60 mHz, keeping typical long periods of interest. The two filtered signals are shown in figure 3.7. The amplitude of the oscillations in the quiet Sun is seen to be an order of magnitude smaller than those in the sunspot and we conclude that the oscillations of the quiet Sun in this narrowband frequency interval are not significant.

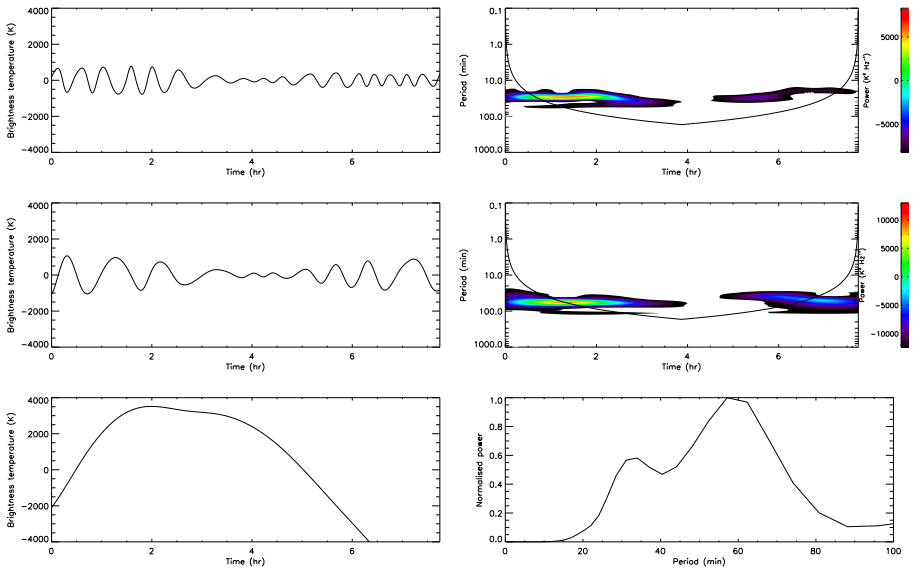

Figure 3.6: Three components derived by the empirical mode decomposition method for the signal from AR10105. The wavelet power spectra are shown for the first two of these components. The third component (bottom left) is the trend component. Bottom right: the global wavelet spectrum of the two oscillatory components displayed.

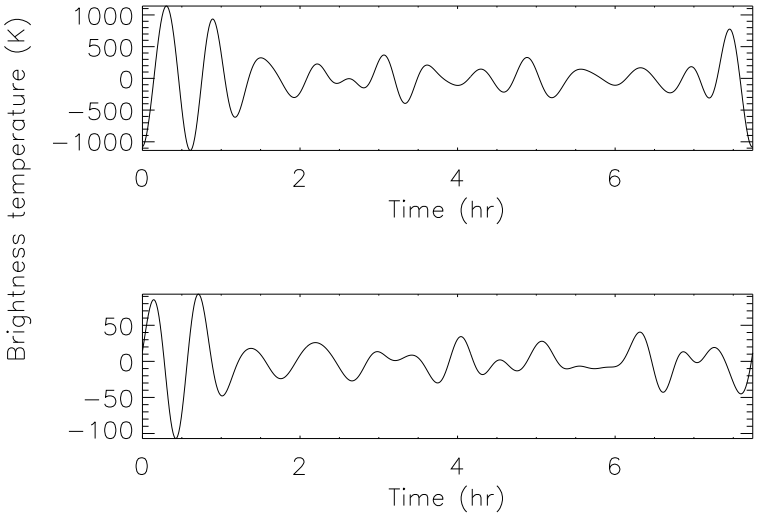

Figure 3.7: Time series for AR10330 (top) and a quiet Sun region (bottom), after narrowband filtering to contain only long period oscillations ($f \approx 0.35$-0.60 mHz).

3.3.6 Spatial structure of the oscillations

Since the data used in this work were three dimensional (two spatial dimensions, plus time), we were interested in investigating the coherency of the oscillations in space and to do this, we made use of the mapping techniques described in section 2.2.1.

For active regions AR10105 and AR10330, we first took images with a larger field of view than the ones used for generating the FOV-integrated time series studied in sections 3.3.1 to 3.3.4. The images for both datasets were 20 × 20 pixels and all the other parameters (starting centre, start and end times, time cadence) were the same as those for the smaller images. Signals of all pixels outside the sunspot radio source region were suppressed by setting their values to 0 over all time. The choice of which pixels constituted the source region was made by setting a threshold on the intensity in the first image of the datacube - any pixels with values less than the threshold were suppressed. The threshold values used were as follows: AR10330: 2×10^4 K, AR10105: 2.5×10^4 K. These thresholds were simply chosen by eye to include as little quiet Sun as possible. After suppressing pixels outside the source region, the time series for each pixel in the datacubes were subjected to the same detrending and filtering procedure as was used for the FOV-integrated time series

described in section 3.3.1.

The global wavelet spectra in figure 3.3 show that there are two distinct low frequency peaks present for AR10105 and AR10330. It was thus decided to produce period, power, correlation and lag maps for each of these peaks independently, so the datacubes were filtered to contain the peaks separately. The frequency ranges used were: AR10105: $\Delta f_1 = 0.417$-0.833 mHz, $\Delta f_2 = 0.206$-0.417 mHz; AR10330: $\Delta f_1 = 0.292$-0.833 mHz, $\Delta f_2 = 0.133$-0.292 mHz. For the correlation maps, the reference pixel was chosen as the one with the highest global wavelet power and for each frequency range, we produced a correlation map showing the maximum value of the correlation coefficient, over the range of lags $-\frac{1}{2}P$ to $\frac{1}{2}P$, where P is the period of the maximum power in the global wavelet spectrum for the given frequency range. The values of P used were: AR10105: $P_1 = 31$ min, $P_2 = 57$ min; AR10330: $P_1 = 37$ min, $P_2 = 88$ min. In addition, we produced lag maps, showing the lag at which the correlation coefficient of the signal of the current pixel with the signal of the reference pixel was maximal over the same range of lags.

The period, power, correlation and lag maps are shown in figures 3.8, 3.9, 3.10 and 3.11, respectively and it is quite evident that besides frequency range Δf_1 for AR10105, the highest power for the coherent oscillations is localised in the centre of the radio source. However, it is also clear that the individual pixels with the highest power are usually offset, with respect to the centre. For the correlation and lag maps, we have only shown pixels for which $C_{xy}(\tau) \geq 0.3$ to suppress the effects of noise. The correlation and lag maps for AR10105 and AR10330 show that for both frequency ranges, there are regions that oscillate in phase with the master pixels, but also regions that oscillate in anti-phase with them. However, for AR10330, this is not so pronounced in Δf_1. The regions of coherent oscillation are seen to be relatively large, of about 25 pixels. In all examples, the transition between the regions oscillating in phase and those oscillating in anti-phase appears to be sharp.

For frequency range Δf_1 of AR10105, the largest region of coherent oscillation can be seen towards the left-hand side of the lag map in figure 3.11 (top row, left image). The master pixel is located in this region and as such, we expect (and indeed see) that this large region oscillates in phase (or coherently). A region of almost equal size that oscillates also coherently, but in anti-phase with the first region is seen towards the right of this image. This region is made up of pixels for which the maximum correlation was found at the time lag of plus or minus about half

period - these lags are of course almost equivalent when dealing with the maximum correlation value. The lag map for frequency range Δf_2 of AR10105 shows a region of in-phase oscillation through the middle of the sunspot and this is in between two regions that oscillate in anti-phase with the master pixel.

The lag map for frequency range Δf_1 of AR10330 (bottom row of figure 3.11, left image) shows a region of about a quarter of the sunspot size, that oscillates in anti-phase with the master pixel region and is located in the south-west portion of the sunspot. Two regions of coherent oscillation that oscillate in anti-phase with each other are most clearly seen in the lag map for frequency range Δf_2 of AR10330 (bottom row, right image of figure 3.11). These regions are each about half of the size of the sunspot and are aligned with the sunspot's "tilt" with respect to the vertical. The region oscillating in phase with the master pixel is seen in the northern part of the sunspot and the anti-phase region seen in the southern part.

In figure 3.12, we period, power, correlation and lag maps are shown for AR10673. The data were filtered to keep the broad spectral peak in the range Δf = 0.340-1.50 mHz and the threshold used to select only sunspot pixels was 2.0×10^4 K. The highest spectral power here is not seen to be concentrated over the umbral regions and the lag map shows a region of anti-phase oscillation in between two regions of in-phase oscillation.

In figures 3.13 and 3.14, we show the correlation and corresponding lag maps in which only pixels where $C_{xy}(\tau) \geq 0.6$ are coloured, for comparison with those shown in figures 3.10 and 3.11, respectively.

3.4 A multi-wavelength study

Above, we saw that it was possible to detect the presence of long period sunspot oscillations with the Nobeyama Radioheliograph. However, a study at a single wavelength is inherently limited in its usefulness - it is not possible to learn about the same oscillations in other parts of the solar atmosphere. Here, an attempt is made to investigate the same range of periodicities as above, but making use of two instruments and several wavelengths.

Recently, Felipe et al. (2010) performed a similar study using observations obtained in photospheric (Si I, λ = 10,827 Å) and chromospheric (Ca II H and He I, λ = 10,830 Å) lines. The measurements of the Doppler shifts of these lines showed that waves with frequencies below 4 mHz were standing, while those with

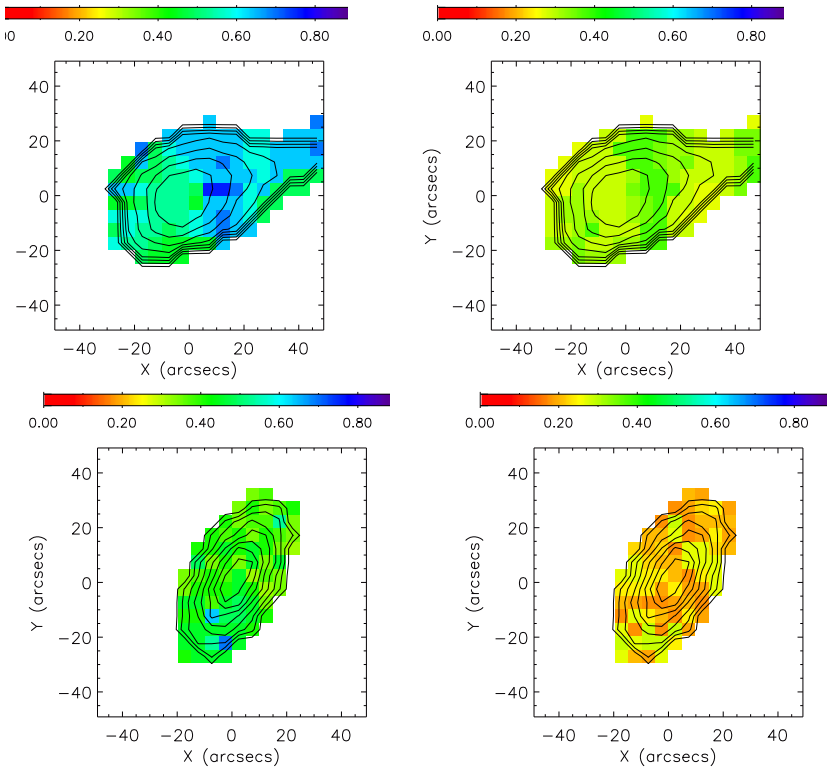

Figure 3.8: The periodmaps for the two separate frequency ranges for AR10105 (top row. Left: Δf_1 = 0.417-0.833 mHz, right: Δf_2 = 0.206-0.417 mHz) and AR10330 (bottom row. Left: Δf_1 = 0.292-0.833 mHz, right: Δf_2 = 0.133-0.292 mHz). The contours show the position of the radio source over the sunspot from the first image in the datacube. Frequencies are normalised to the maximum in each range.

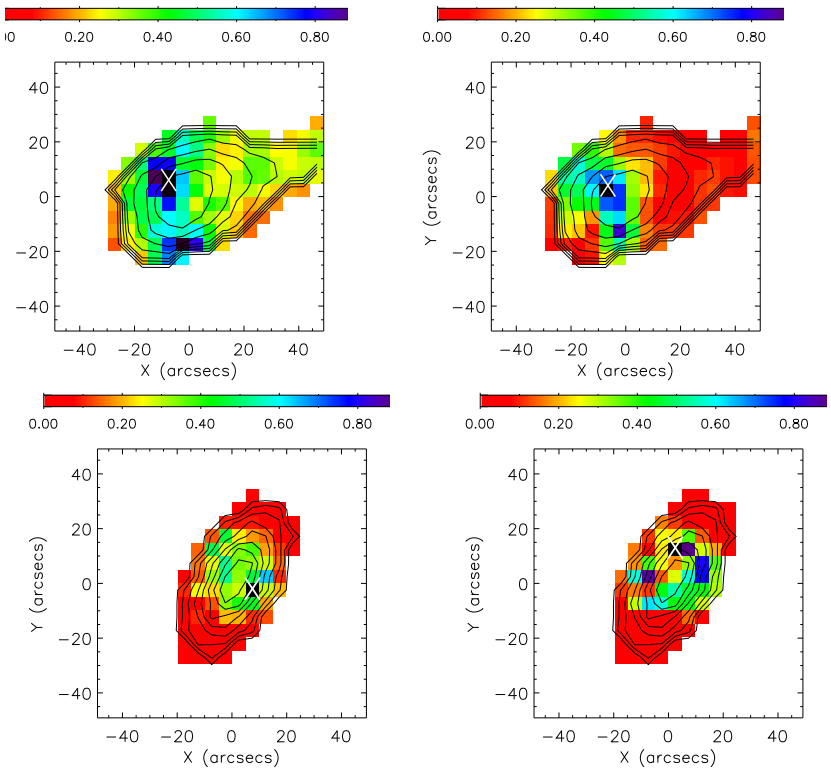

Figure 3.9: Power maps normalised to the maximum power in the map. The layout is the same as that in figure 3.8. The crosses show the location of the reference pixel used for cross-correlation.

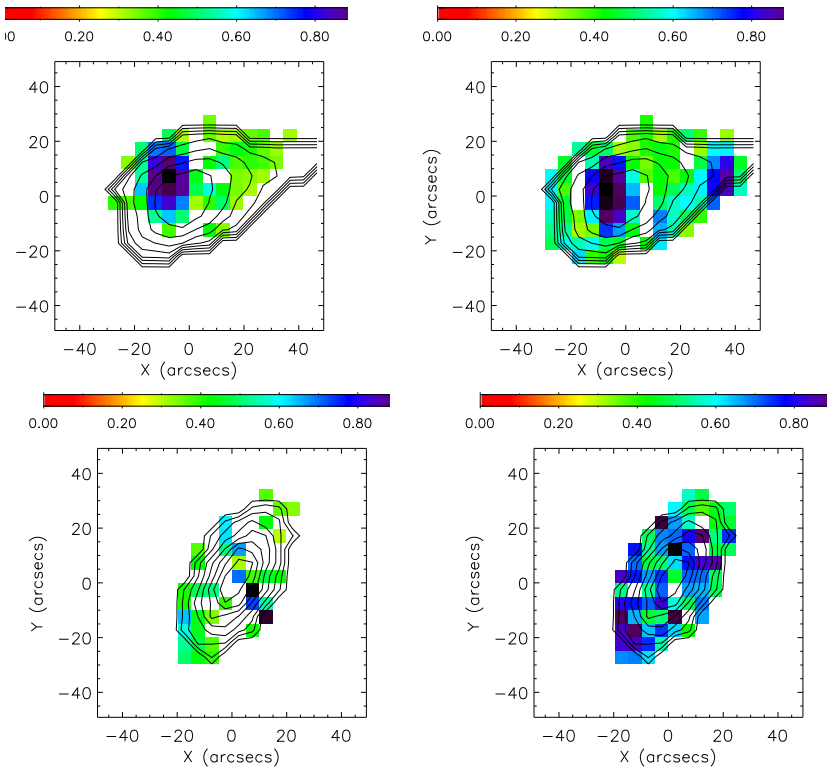

Figure 3.10: Correlation maps showing the maximum value of the correlation coefficient for the two frequency ranges for each sunspot. The correlation coefficient has been computed over the range of lags $\tau = [-\frac{1}{2}P, \frac{1}{2}P]$ where P is the period of the maximum power in the global wavelet spectrum for the given frequency range. The values of P used were: AR10105: $P_1 = 31$ min (left), $P_2 = 57$ min (right); AR10330: $P_1 = 37$ min (left), $P_2 = 88$ min (right). Only pixels for which the correlation coefficient, $C_{xy}(\tau)$, is above a threshold of 0.3 are coloured.

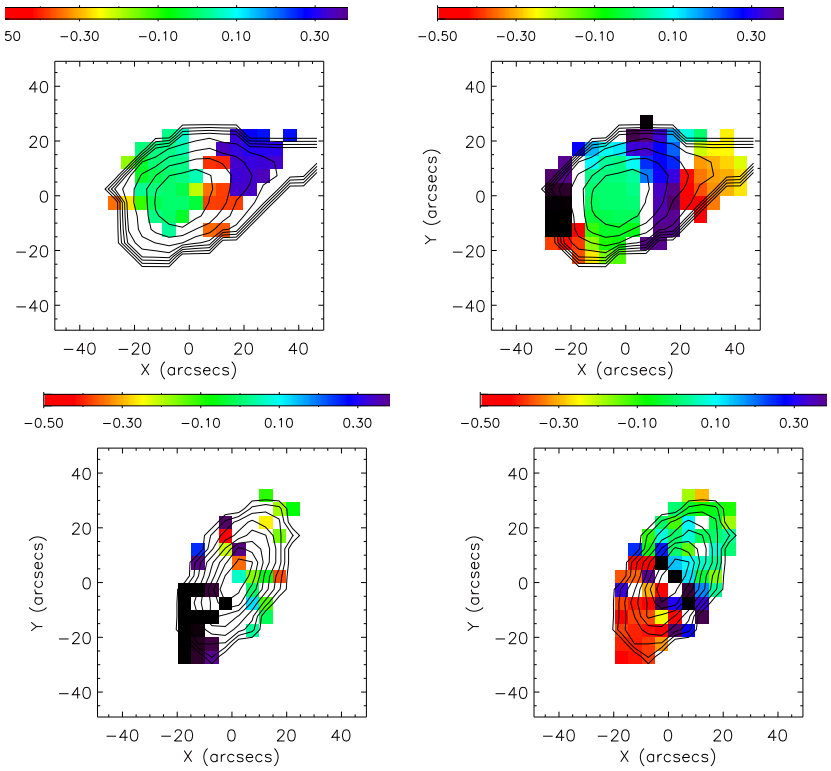

Figure 3.11: The lag maps, corresponding to the correlation maps in figure 3.10, showing the lag at which the correlation coefficient was maximal. Lags have been normalised to the values of P given in figure 3.10.

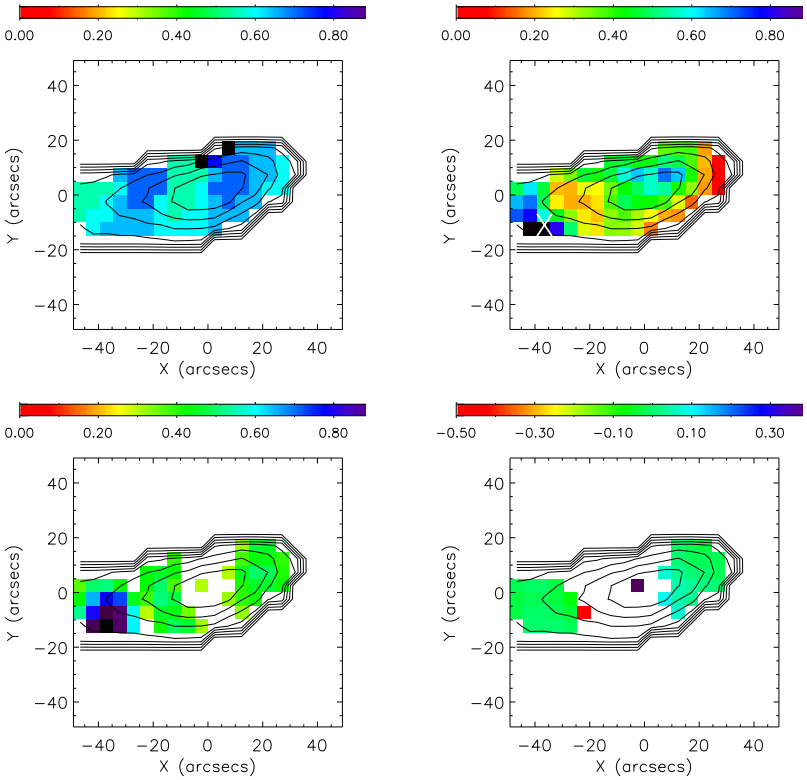

Figure 3.12: Top row: the period (left) and amplitude (right) maps for AR10673 after filtering to keep frequencies in the range Δf = 0.340-1.50 mHz. Frequencies in the periodmap have been normalised to the maximum value in the map (corresponding to the highest frequency in the range) and amplitudes are normalised to the highest amplitude in the map. The cross in the amplitude map shows the location of the reference pixel used for cross-correlation. Bottom row: the correlation (left) and lag (right) maps. Lags have been normalised to P = 27 min.

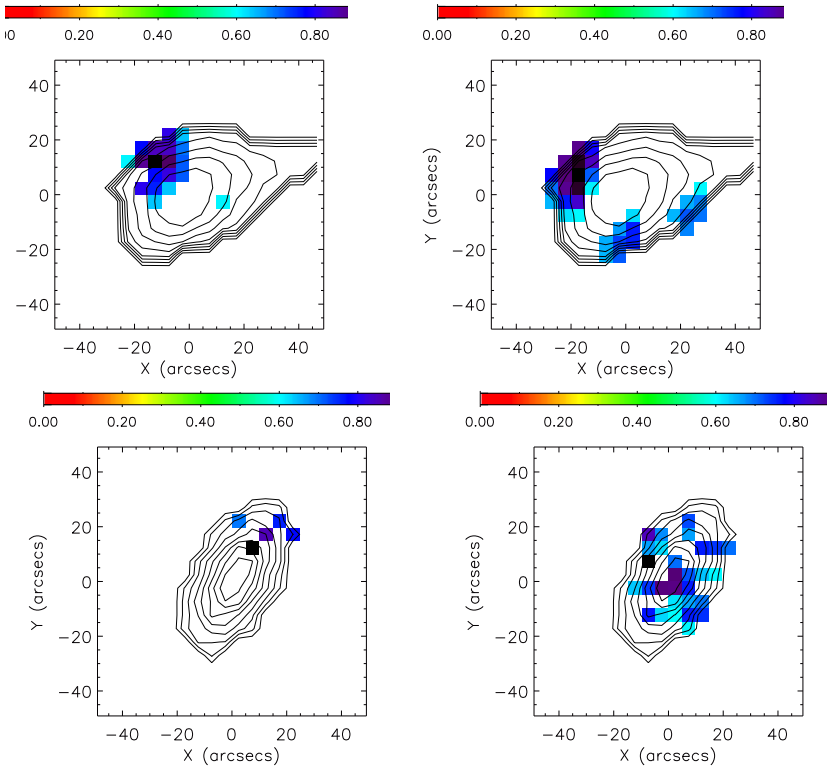

Figure 3.13: The same as figure 3.10, but only pixels for which $C_{xy}(\tau) \geq 0.6$ are coloured.

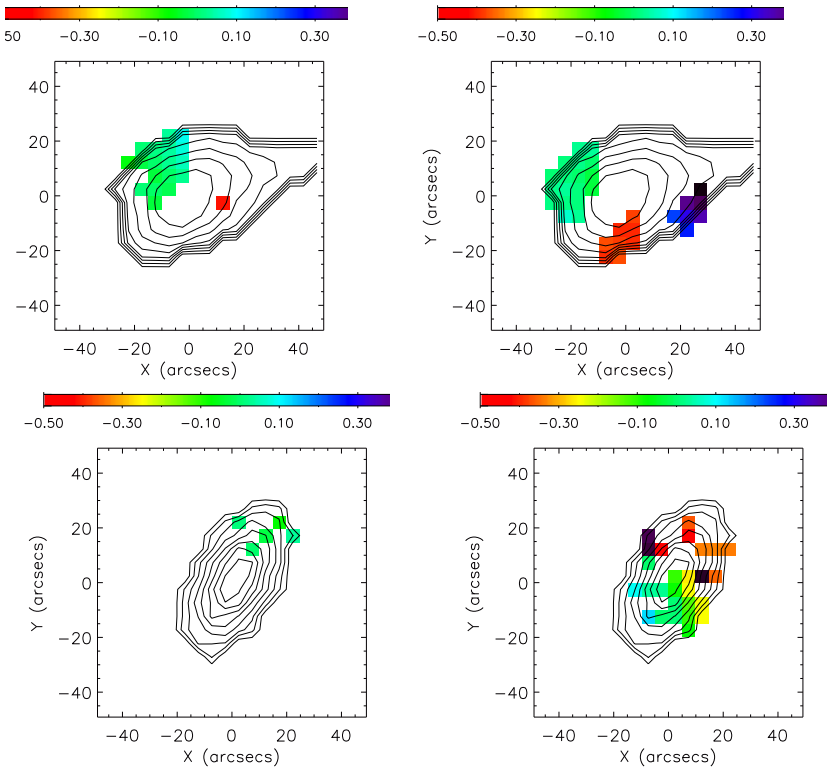

Figure 3.14: The lag maps corresponding to the 0.6 thresholded correlation maps shown in figure 3.13.

frequencies above that value were propagating. The propagating waves were seen to form shocks in the chromosphere and were identified as slow magnetoacoustic waves.

3.4.1 Observations

The sunspot of AR10923 was observed with the Solar Optical Telescope (SOT) on the Hinode spacecraft (Tsuneta et al. 2008) for a period of approximately 5 hr, beginning 11 November 2006 22:00 and ending 12 November 2006 02:58, in two wavelengths: G-band ($\lambda = 430.5$ nm, photosphere) and Ca II H ($\lambda = 396.8$ nm, low chromosphere). The cadence for both wavelengths was about 6 min and the pixel size was $0.109''$. In addition, the same region was observed with the Nobeyama Radioheliograph for a period of 7.25 hr, beginning 11 November 2006 22:45 and ending 12 November 2006 06:00, with a cadence of 10 s. At the beginning of the observations, the active region was located at a position of (-533, -120)$''$, relative to disk centre. Figure 3.15 shows the first images from the datacubes for each wavelength.

The original images from Hinode/SOT were 2048 $\times$ 1024 pixels, but were cropped to 851 $\times$ 901 pixels, to minimise the amount of quiet Sun present. The images from NoRH were chosen to be 22 $\times$ 14 pixels, for the same reason. However, during the 8 hr observations, the size of the radio source appeared to change. This meant that at times, the images included a significant proportion of quiet Sun pixels. A solution to this problem is described in the next section.

3.4.2 Analysis

The SOT data were prepared for analysis by calibrating them with the `fg_prep` routine, to remove any spikes caused by cosmic rays or the Van Allen belts. In addition, the calibration procedure also corrects camera readout problems and removes the dark current. Following the calibration, time series were generated from the SOT data by taking the mean of each image in the datacubes.

As mentioned previously, the size of the active region in the radio band appeared to change significantly during the observation period. As such, we first applied Otsu thresholding as described in chapter 2 to each image in the NoRH datacube to select only the region of interest.

The intensities of the images were scaled to lie in the range 0-255 and the

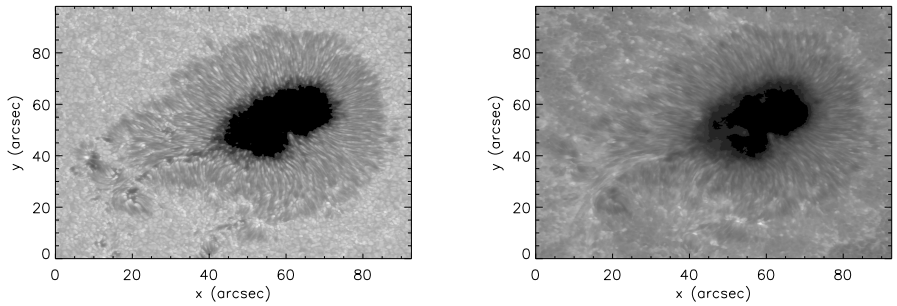

(a) G-band.

(b) Ca II H.

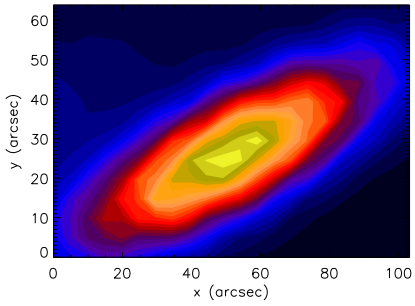

(c) NoRH.

Figure 3.15: Images of AR10923 in each of the wavelengths used in this study.

method was applied as described above. Figure 3.16 shows the first image in the datacube, along with the ROI selected using Otsu's method, showing that the method works well. The maximum value of the separability measure was $\eta = 0.76$. Following this, a time series was generated from the NoRH images, in the same way as for the SOT data.

Figure 3.17 shows the original time series for all three wavelengths. In the signal generated from the Nobeyama images, several flares are present and these were artificially removed by interpolation with cubic splines. In addition, the signal was filtered to remove frequencies $f \leq 1.04 \times 10^{-4}$ Hz, to remove any oscillations lasting less than 3 periods. Trends were removed from all three time series by subtracting 4th order polynomial fits to them.

For all three signals, we performed Lomb-Scargle periodogram analysis (Scargle 1982) and for the NoRH signal, we also performed wavelet analysis using the

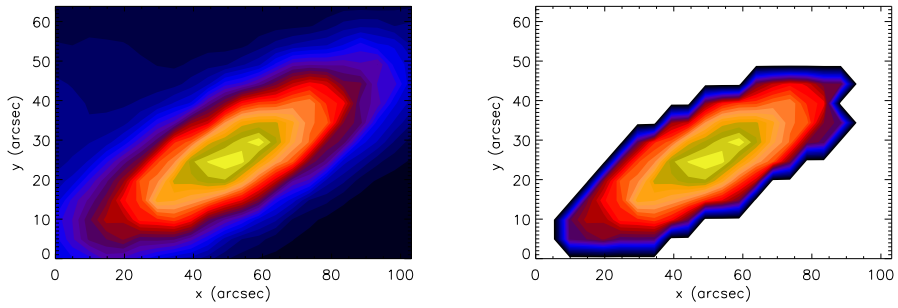

(a) Before. (b) After.

Figure 3.16: The Otsu thresholding method used to select only pixels in the region of interest, as applied to the first image in the datacube of NoRH images of AR10923.

Morlet wavelet (see, e.g Torrence & Compo 1998). It was not possible to perform wavelet analysis for the Hinode/SOT signals, due to their irregular time cadence. In figures 3.18, 3.19 and 3.20, we show the final time series after detrending (and filtering in the case of the NoRH signal) and their spectra for the G-band, Ca II H and NoRH observations, respectively. In the final time series from Hinode/SOT, clear oscillatory signatures are seen. The periodogram analysis revealed periods of $P = 91.27^{+23}_{-10}$ min (G-band) and $P = 80.21^{+21}_{-7}$ min (Ca II H). The difference in periods seen at the two different wavelengths could be due to a change in physical parameters (e.g. density, temperature, etc) in the two different layers of the solar atmosphere. The most likely cause, however, is observational noise, since the spectral peaks are clearly seen to overlap. For the NoRH signal, a peak in the spectrum is not seen around $f \approx 5.5$ mHz (3 mins), which could be due to the directionality of the gyroresonant emission. The magnetic field of the sunspot may not be aligned with the line of sight and the 3 min oscillations are longitudinal ones, meaning that their intensity would be decreased in that case.

The periodogram shows a large peak at a period of $P = 128^{+26}_{-21}$ min. In the wavelet power spectrum, this periodicity is seen to last throughout the 7.25 hr observations and also seen are some bursts of 5 min oscillation.

Spatial analysis was attempted for both SOT wavelengths. The datacubes were first interpolated to a regular time cadence of exactly 6 min and each pixel time series was detrended with a 4th order polynomial. To select only sunspot pixels, thresholds of 850 DN s^{-1} (G-band) and 270 DN s^{-1} (Ca II H) were used.

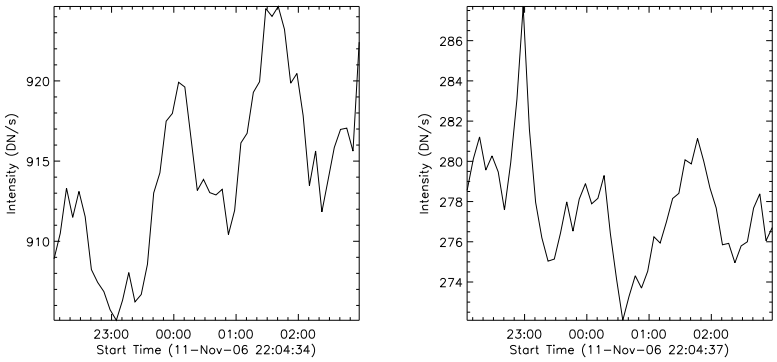

(a) G-band. (b) Ca II H.

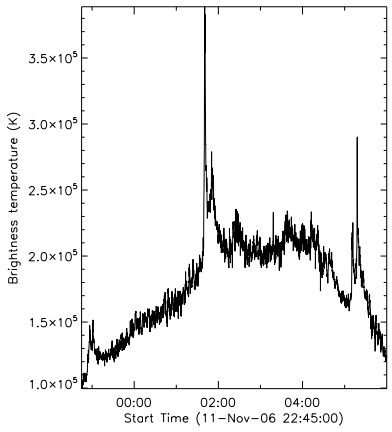

(c) NoRH.

Figure 3.17: Original time series produced from images.

The datacubes were then spectrally filtered to keep the dominant long period peaks found in the spectra of the spatially integrated signals. Boxcar functions were used to select only frequencies in the range Δf = 0.107-0.237 mHz (G-band) and Δf = 0.133-0.256 mHz (Ca II H). The results of this analysis are shown in figures 3.21 and 3.22 for the G-band and Ca II H data, respectively. The amplitude maps show suppressions of power within the umbra, as would be expected since the intensity of the emission is lower there. In addition, both the amplitude and lag maps show filamentary structures in the radial direction of the sunspot, aligned with the penumbral filaments.

The Hinode spacecraft is known to have an orbital period of approximately 98 min. Since the periodicities observed in the Ca II H and G-band data are close to this value, they could be artificial. To test this, signals from quiet Sun regions were investigated in both channels. Figure 3.23 shows the first image in the G-band datacube, showing the regions studied (the regions in Ca II H were the same, so the image is not shown). Figure 3.24 and figure 3.25. It can be seen that in the G-band, only the regions to the right of the sunspot (and towards solar centre) have significant spectral peaks close to the periodicities found in the sunspot signal and these peaks are seen to be broad. In the Ca II H data, there appear to be peaks in the spectra close to those in the sunspot signal, but these are always below the significance level. The lack of significant spectral peaks in all quiet Sun regions suggests that the oscillations in the sunspot signal may not be due to satellite orbital effects.

3.5 Discussion

In this chapter, we have presented the study of long period oscillations in two parts. In the first part, we analysed three eight-hour datasets of the microwave emission generated over three different sunspots, recorded with the Nobeyama Radioheliograph at 17 GHz. The main findings of this part are as follows:

1. Significant long period ($P \approx$ 16-88 min) oscillatory components are present in the time signals of all three analysed sunspots.

2. In each of the spectra of the sunspots, there are at least two such components. In general, these components are found to have higher power than the three minute oscillations. The periodicities are: AR10105: $P_1 = 57 \pm 12$ min,

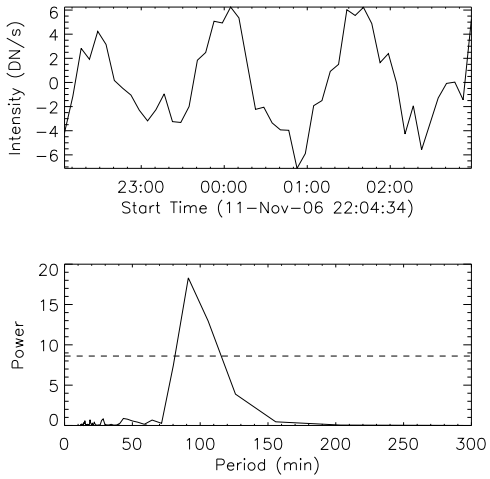

Figure 3.18: Top panel: final G-band time series after detrending. Bottom panel: Scargle periodogram computed from the final signal. The dashed horizontal line indicates the 99% significance level.

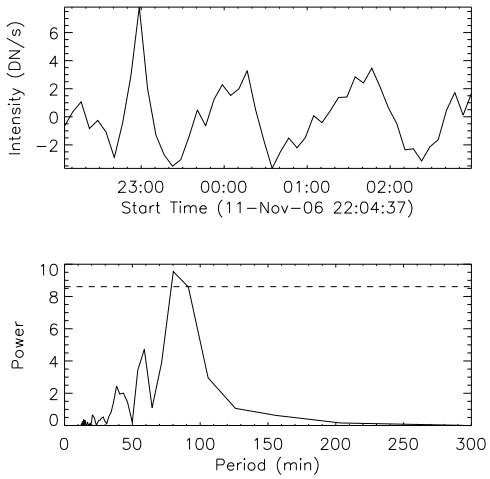

Figure 3.19: Top panel: final Ca II H time series after detrending. Bottom panel: Scargle periodogram computed from the final signal.

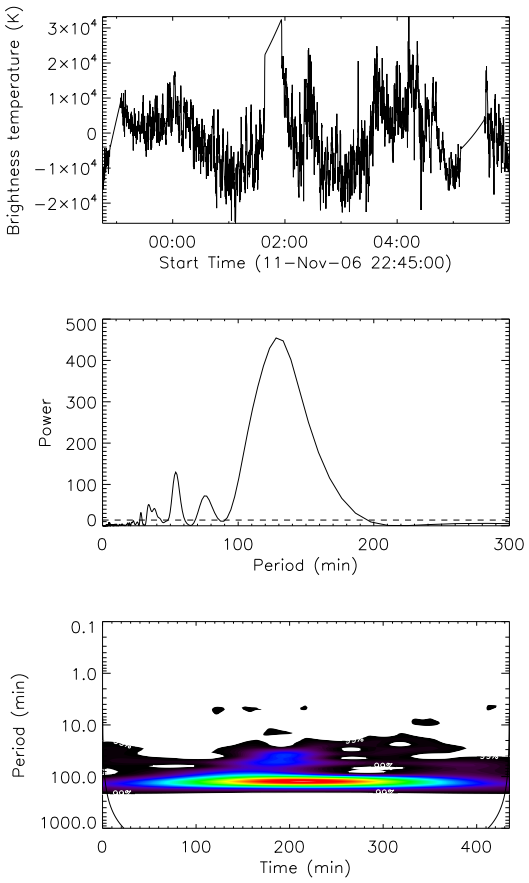

Figure 3.20: Top panel: final NoRH time series after detrending. Middle panel: Scargle periodogram computed from the final signal. Bottom panel: Morlet wavelet power spectrum computed from the final signal.

$P_2 = 31 \pm 6$ min; AR10330: $P_1 = 88^{+16}_{-21}$ min, $P_2 = 37^{+8}_{-11}$ min; AR10673: $P_1 = 27 \pm 16$ min, $P_2 = 16 \pm 4$ min.

3. The periodicities stay constant during the observing intervals, without any significant drift.

4. The spatial distribution of the oscillations shows, in general, (for both frequency ranges of AR10330 ($\Delta f_1 = 0.292$-0.833 mHz, $\Delta f_2 = 0.133$-0.292 mHz) and for frequency range $\Delta f_2 = 0.206$-0.417 mHz of AR10105) regions of enhanced power in the umbral regions.

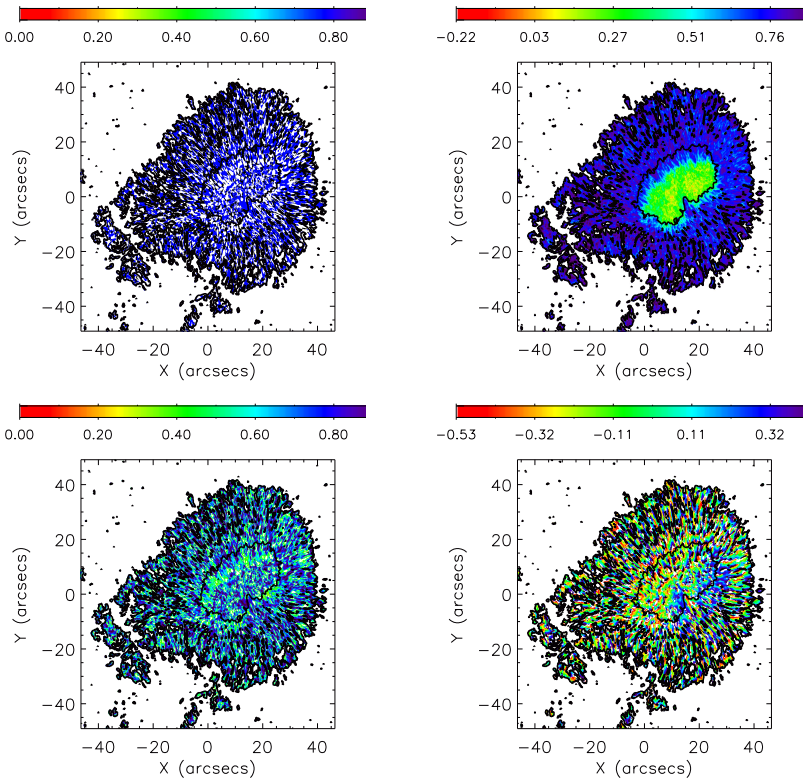

Figure 3.21: Top row: the period (left) and amplitude (right) maps for AR10923 from the G-band data, after filtering to keep frequencies in the range $\Delta f = 0.107$-0.237 mHz. Frequencies in the periodmap have been normalised to the maximum value in the map and amplitudes are displayed on a logarithmic scale. Bottom row: the correlation (left) and lag (right) maps. Lags have been normalised to $P = 45.5$ min.

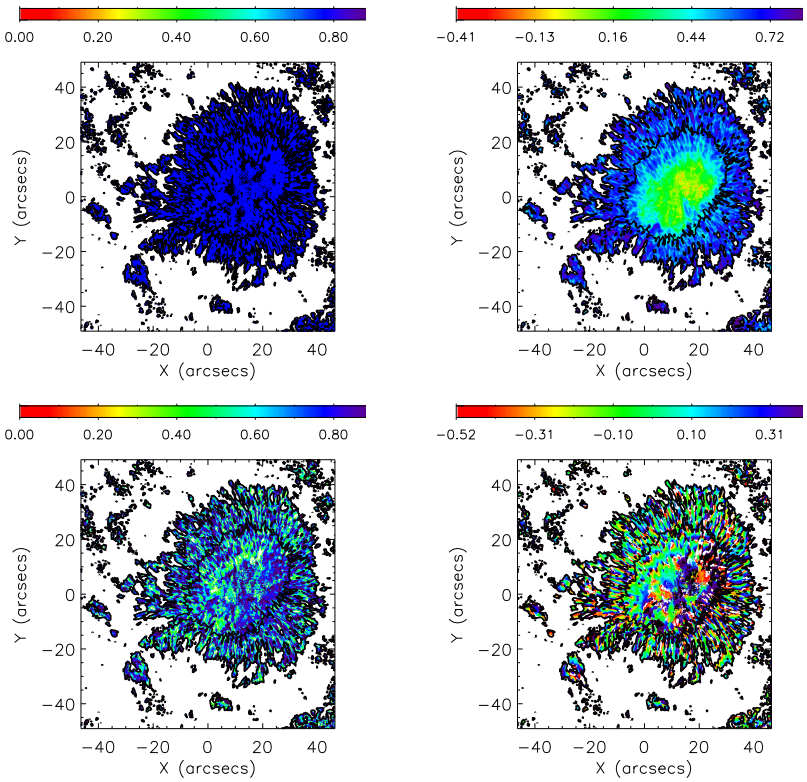

Figure 3.22: Top row: the period (left) and amplitude (right) maps for AR10923 from the Ca II H data, after filtering to keep frequencies in the range $\Delta f = 0.133$-0.256 mHz. Frequencies in the periodmap have been normalised to the maximum value in the map and amplitudes are displayed on a logarithmic scale. Bottom row: the correlation (left) and lag (right) maps. Lags have been normalised to $P = 40$ min.

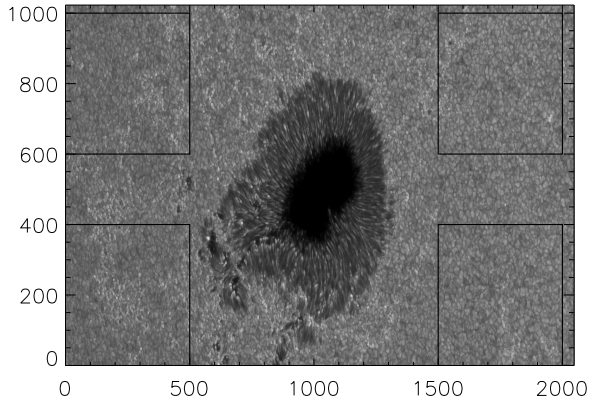

Figure 3.23: The first image in the G-band datacube showing the regions of quiet Sun studied to test for the artificial nature of the periodicity. The solar limb is towards the left of the image.

5. There are regions of the sunspots that coherently oscillate both in phase and in anti-phase with the chosen master pixel. The typical size of the coherently oscillating regions is about 25 pixels. For frequency ranges $\Delta f_1 = 0.417$-0.833 mHz of AR10105 and Δf_2 of AR10330, there are two regions of almost equal size that oscillate in anti-phase with each other. For frequency range Δf_2 of AR10105, a region of in-phase oscillation (with the master pixel) is found in the centre of the sunspot and is surrounded by regions oscillating in anti-phase. A sharp spatial transition between the different regions of coherent oscillation is seen in all cases.

In the second part, we attempted the study of the oscillations in a single sunspot, but made use of optical observations (in Ca II H and G-band, using Hinode/SOT) as well as microwave data. The periods found were as follows: Ca II H: 80.21^{+21}_{-7} min; G-band: 91.27^{+23}_{-10} min and microwave: 128^{+26}_{-21} min. Above, shorter periods (in the range $P \approx$ 16-60 min) were observed with NoRH and the periodogram generated from the Ca II signal shows the possible presence of peaks around 40 and 60 min. Wavelet analysis for the microwave data again revealed the presence of the oscillation throughout the observation period. The lack of significant spectral peaks close to these periodicities in quiet Sun regions in the optical wavelengths may suggest that

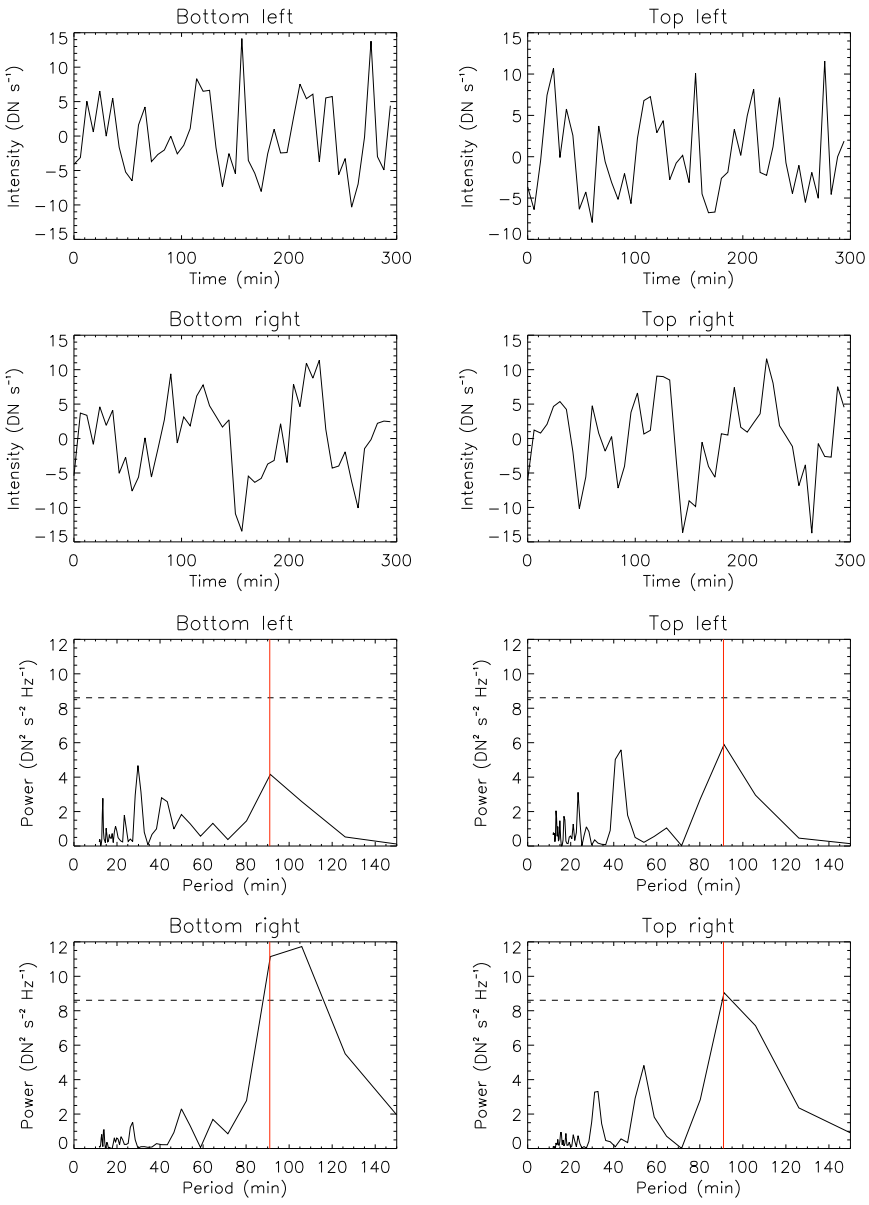

Figure 3.24: Top two rows: the time series from the quiet Sun regions (G-band). Bottom two rows: the Scargle periodograms for the time series in the top two rows. The dashed lines show the 99% significance levels and the red lines mark the 91 min period that was found in the sunspot signal.

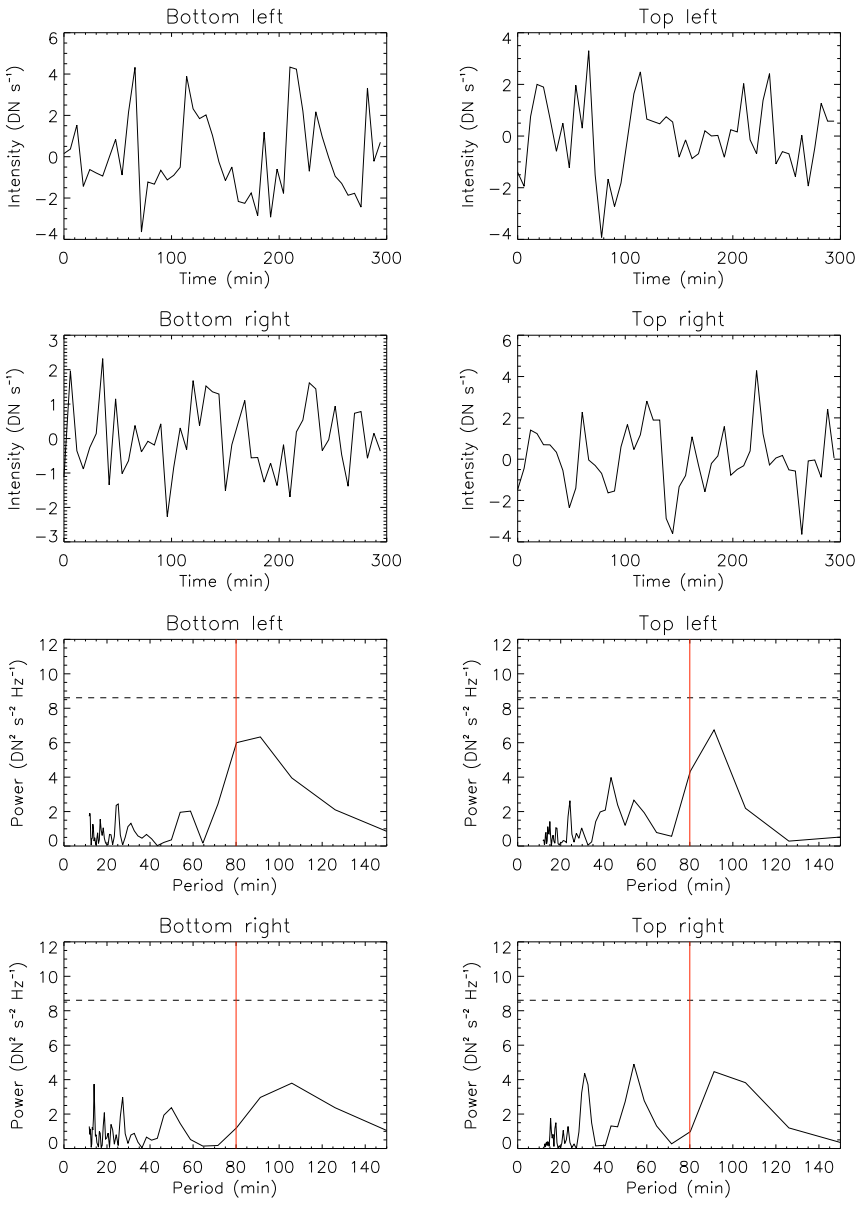

Figure 3.25: Top two rows: the time series from the quiet Sun regions (Ca II H). Bottom two rows: the Scargle periodograms for the time series in the top two rows. The dashed lines show the 99% significance levels and the red lines mark the 80 min period that was found in the sunspot signal.

the oscillations are not artificial.

The nature of the detected long period oscillations in sunspots is still not revealed. In the following, we discuss possible options. The observed periodicities are close to the periods of candidate spectral peaks associated with g-modes: e.g. 22-26 min and about 75 min (García et al. 2008) and the sunspot magnetic flux tubes can operate as waveguides, channelling signals of g-modes from deeper regions. This is just a hypothesis, as flux tubes are known to act as waveguides (see, e.g. Nakariakov & Verwichte 2005). Thus, one possible interpretation of the observed periodicities is their association with the leakage of g-modes, but this scenario requires a solid theoretical foundation. Also, the observed anti-phase oscillations in different parts of the sunspots do not seem to support this interpretation.

The observed patterns of fluctuations are also consistent with the shallow sunspot model of Solov'ev & Kirichek (2008). In this model a cylindrical magnetic flux tube has a finite depth of $L \sim 3$ Mm below the solar surface, where it terminates. The flow around the structure and close to its boundary is mainly vertically downwards for depths smaller than L, and becomes a mostly horizontal flow below the depth L (Zhao et al. 2001). For such a configuration, radially structured fluctuations (that is fluctuations with a certain azimuthal symmetry) could be excited at the bottom of the flux tube and propagate vertically to generate patterns, such as these observed in figure 3.10. It has been shown, using the variational principle, that the periods of such oscillations vary from 40-200 minutes (Solov'ev & Kirichek 2008), in agreement with periods detected in this work.

Chapter 4

Period persistence of long period oscillations in sunspots

4.1 Introduction

Sunspots are the most visible manifestation of the solar magnetic field in lower regions of the solar atmosphere and are interesting features to study as they may provide clues about the nature of the mechanism for generating the magnetic field, the solar dynamo. Associated with them may be filaments - dark, cool structures which lie along the magnetic polarity inversion line in the region. In this chapter, we study 9 successive observation intervals of one of the sunspots studied in chapter 3 in order to investigate the lifetime of the long period oscillations.

One reason to study the lifetimes of long period oscillations is that as explained previously, their nature has not been determined. If we are able to show whether they are transient or long-lived, we can perhaps connect their existence to other phenomena in sunspots that occur on short or long timescales, respectively. Another reason is that they may have potential for inferring the properties of the sunspots in which they're found. Sunspot groups are evolving features (for example, their magnetic classification can change over their lifetimes) and the properties of long-lived oscillations (e.g. their periods) may therefore be sensitive to changes that occur. Thirdly, changes in the properties of the oscillations may be linked with activity in the active region and may offer some potential for forecasting of those events. A study of this kind concerning 3 minute oscillations was performed by Sych et al. (2009).

The chapter is organised in the following way: section 4.2 presents the observations and preprocessing of the data and in section 4.3, we detail our analysis and results and in section 4.4, we discuss our results and propose a simple model for the generation of the observed oscillations. In sections 4.5 and 4.6, we carry out some simple investigations to determine whether the proposed model is a viable mechanism for the observed oscillations. Finally, in section 4.7, we present some conclusions.

4.2 Observations

The sunspot of NOAA AR10330 was observed over intervals of approximately 7.25 hours on 9 successive days with NoRH, beginning on 06 April 2003 and ending on 15 April 2003. The observations began at 22:45 UT on each day and ended at around 06:30 UT the following day. At the beginning of the observation period, the region was located at a position of $(-572, 199)''$, relative to disk centre. For convenience, throughout this chapter, we refer to observations on each date (e.g. time series) by a number corresponding to their position in the sequence of 9 days (i.e. 1 for 06 April, 2 for 07 April, etc).

Figure 4.1 shows the region in white light (from SOHO/MDI) and microwave on 09 April 2003 and Hα (from the Yunnan Astronomical Observatory) on 10 April 2003. The Hα image shows evidence of a dark filament associated with the region, located north-west of the main region. This region has been studied by Sainz Dalda & Martínez Pillet (2005) and Zhang et al. (2007), who investigated moving magnetic features and their relation to penumbral filaments and evolution of the parent sunspot. The studies of both groups used data in the interval 09 April 2003 14:00 UT - 10 April 2003 00:50 UT. In addition, the observations used in this chapter include those used in chapter 3 (08 April 2003 22:45 UT - 09 April 2003 06:30 UT).

Sequences of images were obtained for each date from NoRH at a frequency of 17 GHz. The emission is generated by the gyroresonant mechanism, where a low harmonic of the cyclotron frequency is equal to the frequency of the instrument (Shibasaki et al. 1994; Vourlidas et al. 2006). The images were of size 8×8 pixels, with a spatial resolution of $5''$ per pixel (corresponding to a distance of about 0.73 Mm) and the time cadence was 10 s. This was a restricted field of view to minimise the contribution from the quiet Sun. Due to the long intervals of observation, the solar rotation had to be taken into account. The process for doing this was previously

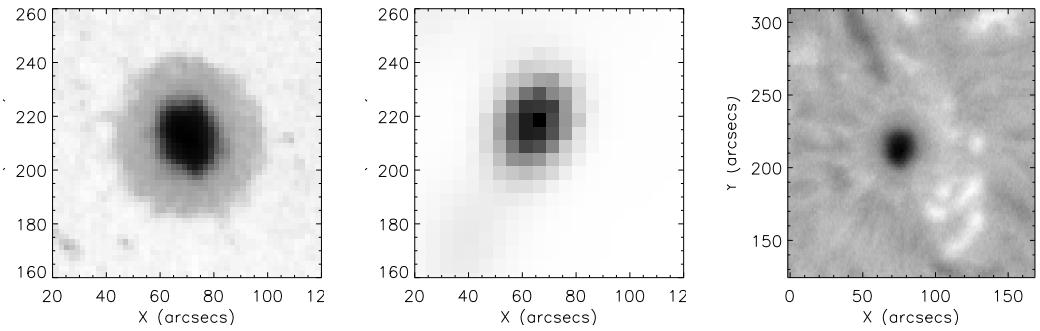

Figure 4.1: Images of AR10330 in white light (left) and microwave (17 GHz, centre) taken at 23:59 UT on 09 April 2003 and in Hα (right), taken at 01:03 UT on 10 April 2003. The microwave image is displayed in reverse intensity scaling.

described in section 3.2.1.

From each daily set of images, we generated a time series by computing the mean brightness temperature, T_B, of each image. Present in each time series was a large scale trend mainly due to the change in effective area of the instrument as the Sun passed overhead during the course of the local day. The change in effective area of NoRH (as seen by the Sun) is due to the change in elevation and azimuthal angle of the Sun over the course of the 8 hr observations. At the start and end of the observations, the Sun is low in the sky and the projected shape of the interferometer's collecting area (as seen by the Sun) is elliptical. As the Sun moves towards the zenith, the projected area becomes circular. This is similar to the formation of a shadow. The trend present in the signals is the manifestation of this effect; the area seen by the Sun is smaller at the ends of the observation, so the amount of radiation collected is reduced. The form of the trend is sensitive to this effect, as well as to changes in the radio source and it is therefore not possible to create a general curve to fit. In addition the path of the Sun across the sky varies between days.

The trend was removed by fitting a 4th order polynomial and spectrally filtering the time series to remove oscillations with 3 cycles or fewer ($P \geq 145$ min). Figure 4.2 shows the resulting detrended time series.

Most of the time series generated in this way contained large increases in T_B, that were most likely to be flares and several instrumental glitches. All such features were identified and then removed from the time series by interpolation with a cubic

spline. To identify the flares, we set a threshold on T_B of 8.5×10^4 K for most time series (except for days 5 and 9, for which values of 6.5×10^4 K were used). For the amplitude study described in section 4.3 below, we did not remove the spikes in the signals.

4.3 Analysis

We computed Fourier power spectra, Lomb-Scargle periodograms (Scargle 1982) and global wavelet spectra (see, e.g. Torrence & Compo 1998) for each detrended and interpolated time series in order to investigate the long period oscillations. Figure 4.3 shows the spectra obtained by each of these methods, for each of the 9 time series. It can be seen that long period oscillations in the range $P = 50$-120 min are present in all time series and that there are, in general, two long period peaks in the spectra.

Figure 4.4 presents information related to the solar activity and an analysis of the dominant periods, in order to determine whether any events in the region could have been responsible for changes in the observed period.

We obtained the full disk flux observed by the GOES spacecraft and identified flares and CMEs that occurred in AR10330, as well as in other regions, during our observation period. This is shown in panel (a) and it is clear that the Sun was quite active during the entire 9 days of observations, as evidenced by the large number of peaks in the GOES flux. However, it can also be seen that there were two events in the region during the observations: a filament disappearance (beginning after 08 April 2003 00:45 UT and ending before 08 April 2003 13:02 UT) and a C class flare that occurred on 13 April 2003 at 08:45 UT. These events are indicated by dashed vertical lines.

In panel (b), we show the original time series generated from the sets of NoRH images. Large increases in brightness temperature can be seen, which do not appear to coincide with peaks in the GOES flux. The reason for this could be that small events (relative to the full disk flux) in the region do not necessarily appear in the full disk GOES flux, but can cause large local brightenings due to the restricted field of view. It can also be seen that there is a trend in the mean intensities in the signals over the 9 days of observations. For the first 7 of those days, the trend is roughly symmetric about the interval between signals 3 and 4, when the sunspot crosses the central meridian. In addition, the mean intensity is seen to decrease for

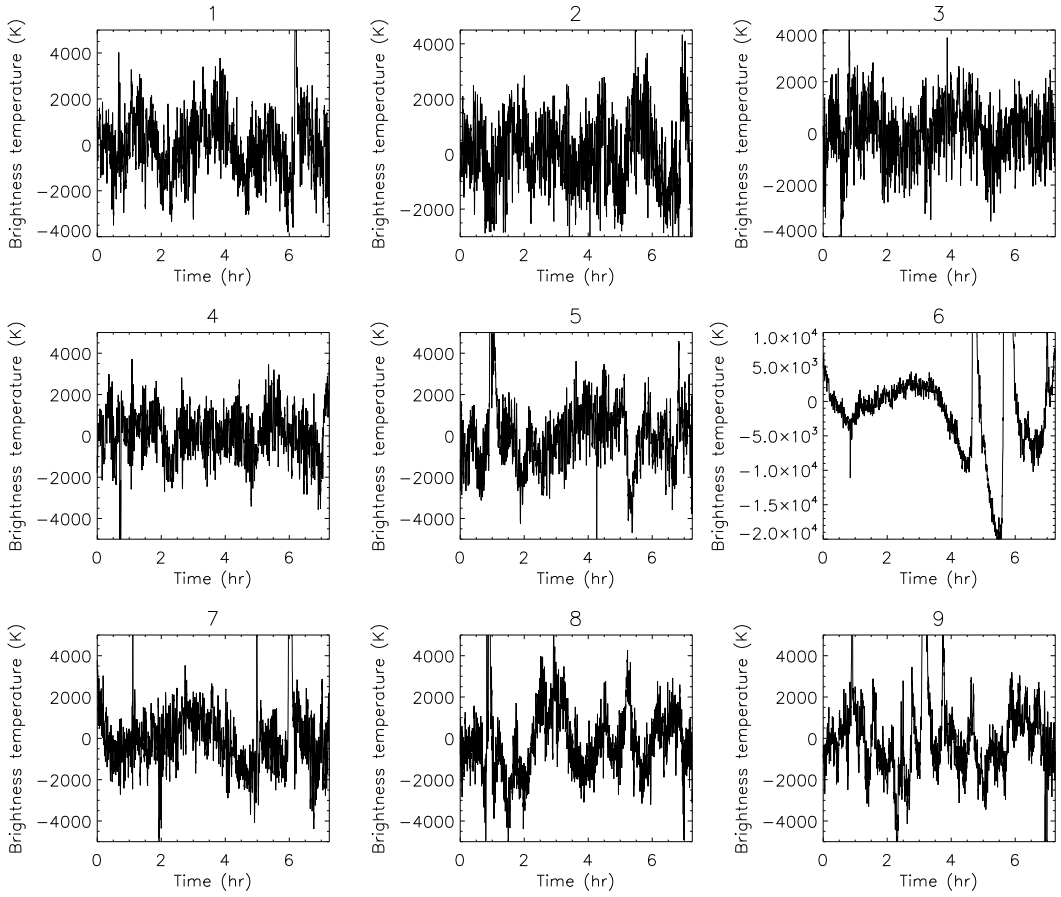

Figure 4.2: Time series of microwave intensity generated from sequences of images of AR10330 obtained with NoRH. The signals have been detrended with a 4th order polynomial. The title for each signal gives the day number in the sequence of the 9 days of observation.

signals 8 and 9, which is attributed to the sunspot being positioned close to the limb on those days and both of these points are suggestive of a projection effect.

In panel (c), we show the dominant periods (i.e. the periods corresponding to the highest spectral peak) in the range P = 50-120 min and all three methods gave similar values (within the error bars of the global wavelet), except in the last case. It can also be seen that the dominant period remained quite stable over the course of the observations. The dominant period appears to reach a local minimum in signal 7 before the flare in the region and is seen to rise after it. This decrease in period could be associated with changes in magnetic configuration that may or may not lead to a flare.

In panel (d), the power of each of the 5 long period Fourier components in the range P = 50-150 min is shown for each of the 9 days. The signals were first filtered to contain only periods in this range, using a boxcar function as the filter. The first feature of note is the large rise in power in all 5 components for signal 6. This is artificial since the time series contains large peaks (see figure 4.2) that are of a finite width and as such, the detrending procedure introduces an artificial oscillation whose period is close to those of interest. The amplitudes for all components over the days excluding day 6 do not appear to vary by a large amount.

We also attempted to investigate the change in phase of the long period oscillations over the 9 days of observations in the following way. For each of the 5 Fourier components in the range P = 50-150 min range (after filtering), we found the phase for each of the 9 signals. Naturally, one is interested in the phase of the oscillation at some common reference point, here chosen as the beginning of the observations (06 April 2003 22:45 UT). In order to obtain Fourier phases with respect to this common reference, we made use of the time delay relation of the Fourier transform $\mathcal{F}$, of a signal $I(t)$,

$$\mathcal{F}\left[I\left(t-t_0\right)\right] = \mathcal{F}\left[I\left(t\right)\right] e^{-i2\pi f t_0}, \tag{4.1}$$

where t_0 is the time delay and f the frequency. Equation (4.1) tells us that a time delay is seen as a phase shift in the Fourier transform. In order to obtain the phase of the oscillation at the beginning of the observations, we divided $\mathcal{F}\left[I\left(t-t_0\right)\right]$ by $e^{-i2\pi f t_0}$ to give $\mathcal{F}\left[I\left(t\right)\right]$ and then found the phase from the real and imaginary parts of the relevant component. Figure 4.5 shows a polar plot of the phases for each of the 5 components, on each of the 9 days. The phases for different components are

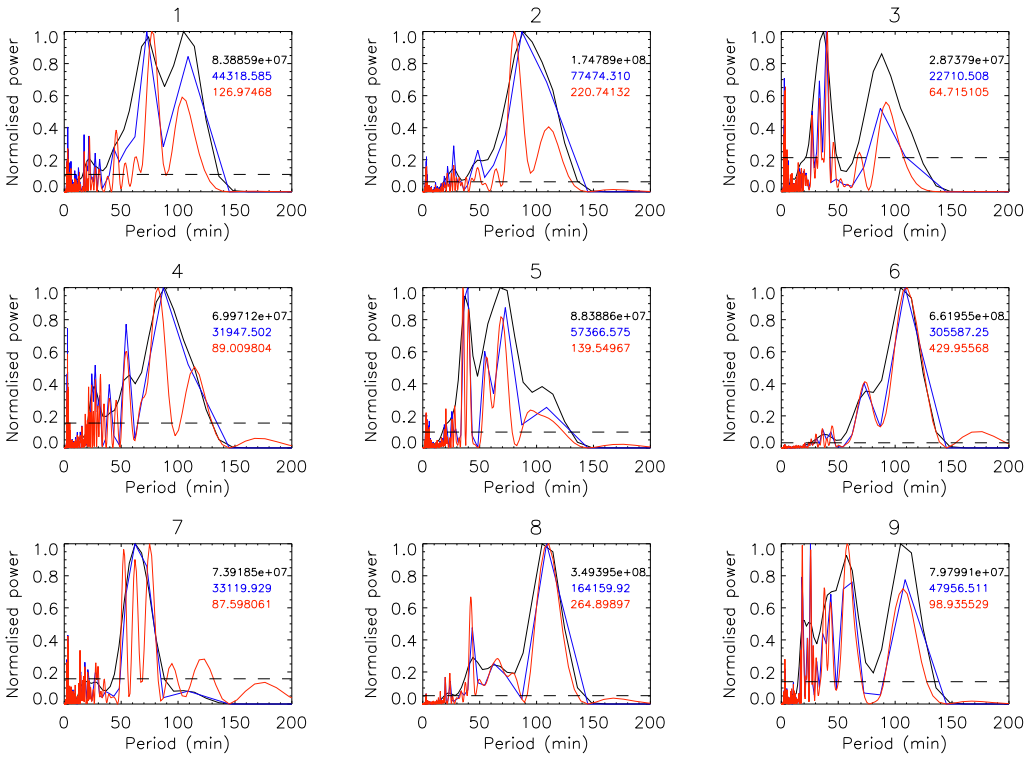

Figure 4.3: Normalised power spectra obtained for each of the 9 detrended signals, using the global wavelet (black), Lomb-Scargle periodogram (red) and Fast Fourier Transform (FFT, blue). Each spectrum has been normalised to its maximum amplitude. As in figure 4.2, the title for each signal gives its position in the sequence of the 9 days of observation. The dashed lines show the 99% significance level for the periodograms (normalised to the maximum value of the periodogram). The values in the top right of each plot show the maximum amplitude in each of the three spectra.

seen to behave in different ways over time and that there does not seem to be any long term stability in the phases over the entire course of the observations.

4.4 Discussion of the observational results

We have analysed nine 7.25 hour intervals of microwave emission at 17 GHz over NOAA AR10330, observed with the Nobeyama Radioheliograph. The main finding of this study is that long period oscillations ($P \geq 50$ min) are found to be present in each of the analysed time intervals and the dominant long period component appears to be stable over the observations. The apparent change in period between 13 April 2003 06:30 and 13 April 2003 22:45 (the interval between signals 7 and 8) is not due to changes in magnetic configuration in the region, which can be determined by examining magnetograms from SOHO/MDI. In addition, the spectral amplitude of 5 Fourier components in the range $P = 50$-150 min shows stability over the course of the observations, when the data are not influenced by changes in magnetic configuration or large flares (as on day 6). The large time gaps between the data sets, together with the noise in the signals do not allow us to draw any firm conclusions about the stability of the phases of the oscillations.

Such long periodicities can be associated, for example, with the global oscillations of the sunspots in terms of the shallow sunspot model that was described in section 1.6.3. However, the persistence of those oscillations requires the answer to an additional question: what is the physical mechanism that excites those modes in the quiet Sun and how are the oscillations maintained against the damping? It is not possible, from these observations, to determine the cause of the damping, as the mode of oscillation has not been determined. One possibility for the maintenance of the oscillations is the resonance between a certain driver and the natural frequency of the sunspot. Such a driver could be associated with the 3 minute oscillations of sunspots, which are known to be very persistent narrowband features. Usually, 3 min oscillations are seen to have a fine spectral structure, having multiple peaks (see, e.g. Shibasaki 2001; Gelfreikh et al. 1999). The average spacing between peaks in the 3 min cluster may be close to the low frequencies observed here and hence, it may be possible to create a resonance with the long period oscillations of a sunspot, exciting the long period oscillations and compensating for the damping. However, such a process is possible only in the presence of nonlinear effects.

To illustrate this possibility, we consider a driven simple harmonic oscillator

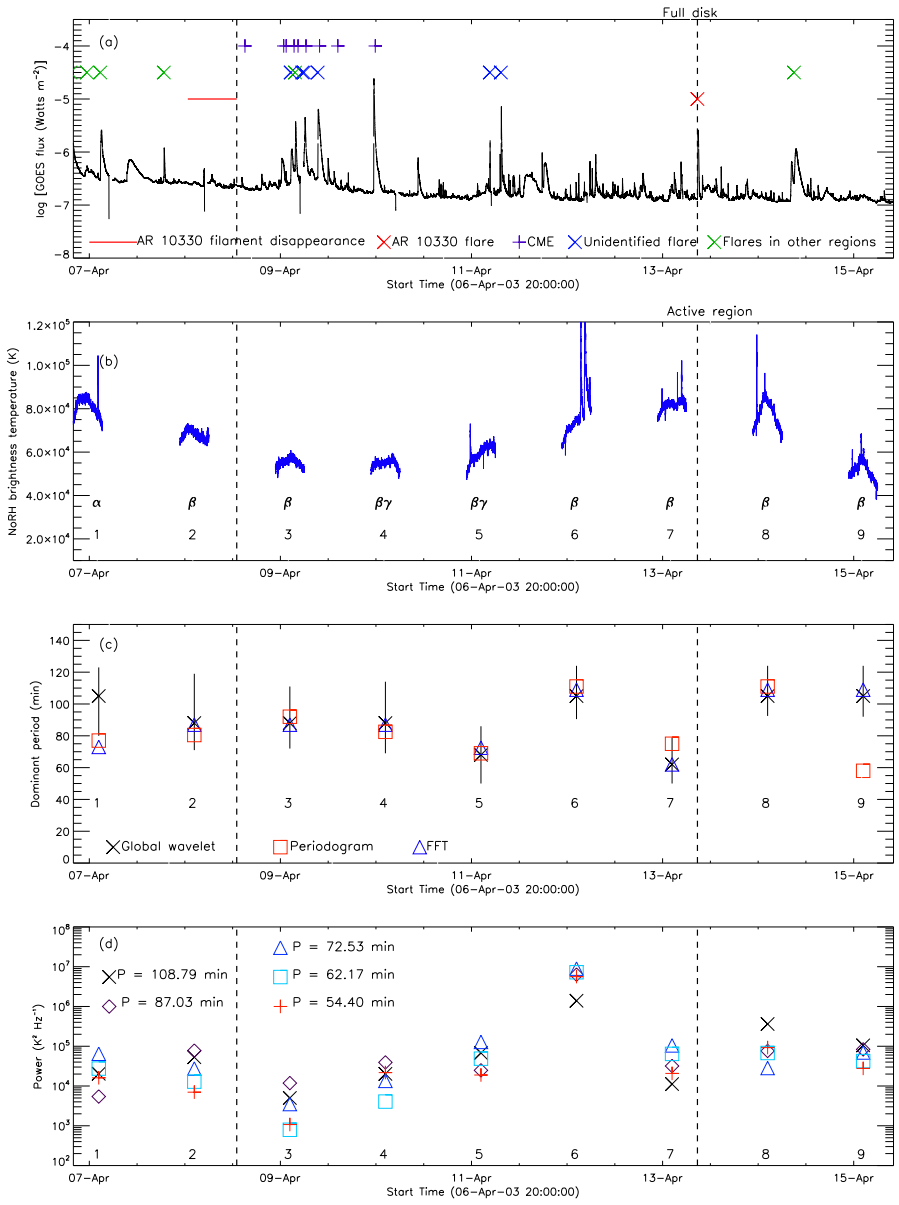

Figure 4.4: (a) The GOES X-ray flux during the period 06 April 2003 20:00 - 15 April 2003 10:00, showing events that occurred in AR10330 and elsewhere. (b) The original time series obtained from NoRH images. The Mt. Wilson classification for AR10330 is also shown. (c) The dominant periods in the range P = 50-120 min, obtained with all three of the methods for computing the power spectrum. The error bars on the global wavelet spectrum were obtained using the full width at half maximum (FWHM) of the corresponding spectral peak. (d) The power for each Fourier component in the range P = 50-150 min for each day. In panels (c) and (d), the points for each day have been plotted at the midpoint of each signal. The numbers in the latter 3 panels refer to the numbers in the sequence of days.

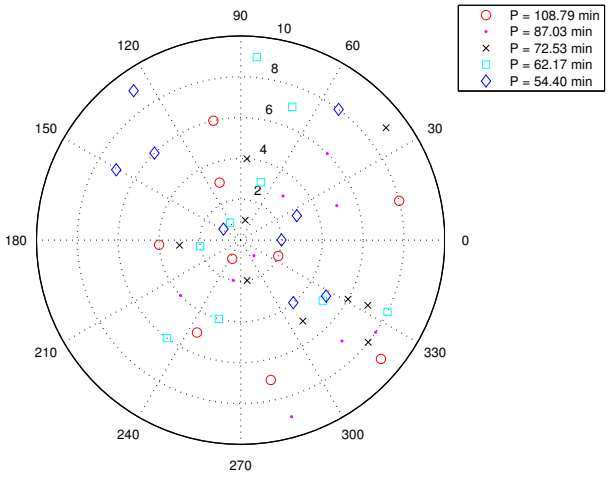

Figure 4.5: The phases for each Fourier component over the 9 days of observation after filtering the signals to contain only periods in the range P = 50-150 min. Phases are given in degrees and the points for each day lie on an annulus at $r = 1, 2, \ldots, 9$, corresponding to the day number (i.e. 1 for 06 April 2003, 2 for 07 April, etc).

in which the driver is nonlinear, e.g.

$$\frac{d^2I}{dt^2} + k\frac{dI}{dt} + \omega_0^2 I = \left[\sum_{i=1}^{m} A_i \cos(\omega_i t + \phi_i)\right]^2, \tag{4.2}$$

where k is the damping coefficient, ω_0 is the natural frequency of oscillation (corresponding to a period of $P \approx 100$ min), the A_i, ω_i and ϕ_i are the amplitudes, frequencies and phases of the driving oscillations and m is the number of driving oscillations, which represent individual peaks of 3 min oscillations. The nonlinearity represents some physical mechanism responsible for the coupling of 3 min and long period oscillations. For example, it can be the modification of characteristic speeds of long period oscillations by the 3 min oscillations.

We stress that equation 4.2 is an empirical model that reflects the observed properties of the oscillations. As such, we make no attempt to estimate the value of k, but only include damping in the model as we know it is a physical effect (due to, e.g. viscosity or leakage of the oscillations to the corona). In addition, ω_0 is related to the magnetic field strength, sunspot depth and mass density as given in Solov'ev & Kirichek (2008).

Expanding the expression on the right hand side of equation 4.2 leads to two kinds of terms, for $i \neq j$:

(i) $\cos^2 \omega_i t$, which can be expressed in terms of $\cos 2\omega_i t$;
(ii) $\cos \omega_i t \cos \omega_j t$, which can be expressed in terms of $\cos(\omega_i + \omega_j)\, t$ and $\cos(\omega_i - \omega_j)\, t$.

The first kind of term gives frequency doubling and we suggest that a broadband spectrum of solar 5 minute oscillations can contribute to the 3 minute oscillations. The second kind of term, in particular the $\omega_i - \omega_j$ kind, suggests that two frequencies close together will generate a low frequency oscillation. As explained above, we suggest that the 3 min part of the spectrum is responsible for this effect.

4.5 Inspecting the high frequency part of the spectrum

To further investigate the relationship between the 3 and 5 min oscillations and the long period ones, we took a closer look at the high frequency part of the Fourier power spectra for each of the nine days. For each spectrum, we first selected all peaks in the 3-5 min band (Δf = 2-8 mHz) whose spectral amplitude was greater or equal to 30% of the amplitude of the highest peak in that band. This threshold was chosen to minimise the number of noise components taken into account. Peaks were defined to be local maxima, meaning that the points either side of a peak had lower amplitudes than the peak. Then, for each pair of the selected peaks, we computed the difference in frequency and constructed the distribution of the frequency differences over ndf, where n is an integer and df is the frequency resolution of the power spectra. The positions of the peaks in the distributions were found and in figure 4.6, we show the periods corresponding to the positions of those peaks against period of the highest spectral peak. In addition, in figure 4.7, we show the total power ($P = \sum_i P_i df$) in the dominant long period peak, plotted against the total power in the 3-5 min band for each of the 9 days. The values have been normalised to the width of the band (ndf) for comparison, so they are in effect the average power per frequency bin. There is no clear trend in either plot (i.e. the points do not lie on a line) and thus, these results do not present us with evidence for a clear relationship between the high and low frequency oscillations.

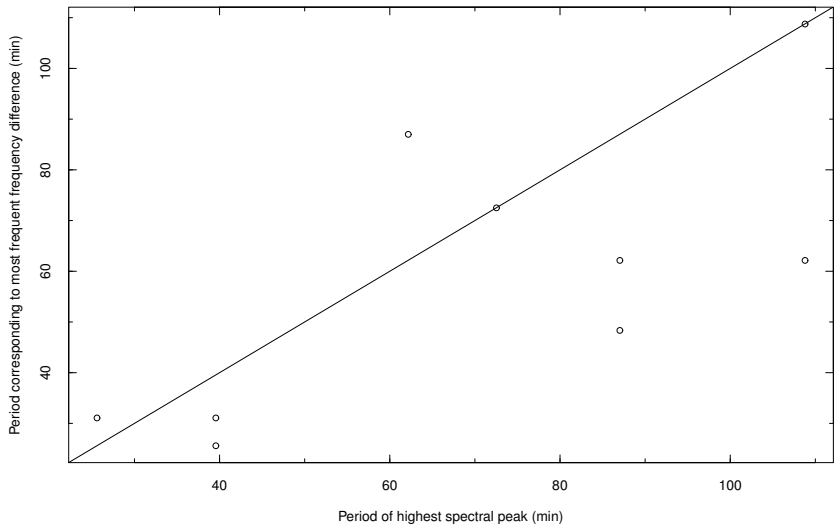

Figure 4.6: The period corresponding to the peak frequency difference in the distribution of pair frequency differences in the 3-5 min band of the Fourier power spectra, plotted against the corresponding global maxima in the spectra. The solid line shows the line $y = x$.

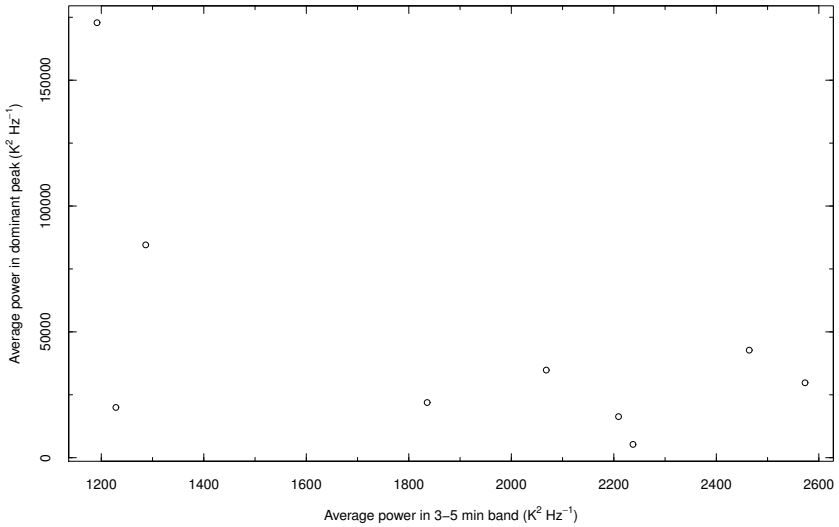

Figure 4.7: The average power in the dominant spectral peak in the Fourier power spectra of each of the 9 observational datasets, plotted against the corresponding average power in the 3-5 min band.

4.6 Numerical validation of the model

To investigate whether or not the mechanism proposed for the generation of the long period oscillations (driving by the 3 minute oscillations combined in a nonlinear fashion) was a viable one, we solved the model equation numerically. A realistic set of driving oscillations was used and these were taken from the signal from day 3 in the sequence of observations. The amplitudes, frequencies and phases for the oscillations on the right-hand side of equation 4.2 were taken for all spectral components in the frequency range Δf = 2-8 mHz, from the Fourier transform of the signal. This gave $m = 156$ driving oscillations.

The equation was solved numerically using MATLAB's `ode45` solver, which uses a Runge-Kutta algorithm. Since this is a method that solves first order ordinary differential equations (ODEs), the second order ODE was first written as two first order equations:

$$v = \frac{dI}{dt} \tag{4.3}$$

Table 4.1: Values of parameters that were common to each numerical study performed here.

Initial conditions	$I(0) = 0, v(0) = 0$
Time span	$t = 0 - 7.25$ hr
Time step	$dt = 10$ s
Natural period	$2\pi/\omega_0 = 90$ min

Table 4.2: Values of the damping coefficient (k), scale factor for the right-hand side (γ) and the form of the right-hand side (RHS) used for both the linear and nonlinear (NL) studies performed here. $F(t)$ is given by equation 4.5.

	Linear	NL, no damping	NL, varying γ	NL, with damping
RHS	$\sqrt{F(t)}$	$\gamma F(t)$	$\gamma F(t)$	$\gamma F(t)$
$\log k$	0	-	-	$-7, -6, \ldots, -3$
$\log \gamma$	-	-12	$-10, -8, -6$	-12

$$\frac{dv}{dt} = F(t) - \omega_0^2 I - kv, \tag{4.4}$$

where the driving term, $F(t)$ is given by

$$F(t) = \left[\sum_{i=1}^{m} A_i \cos(\omega_i t + \phi_i)\right]^2. \tag{4.5}$$

The driving term here is used solely to generate coupling between individual peaks of 3 min oscillations. The emphasis is placed on generating a coupling that can resonate with the natural frequency of the system and not on identifying the physics involved in these oscillations.

Several runs of the solver were performed. Values of parameters that were the same for all runs (the natural frequency of the oscillator, ω_0; the initial conditions, $I(0)$ and $v(0)$; the time step, dt and the time interval for the solution, t) are presented in table 4.1. The form of the right-hand side of equation 4.2, value of the damping coefficient and a scale factor for the right-hand side (described below) that varied between each of the runs described below are presented in table 4.2.

As a first test, the equation was solved with the driving oscillations combined in a linear fashion only and damping was included. The solution of the equation consists of two parts: the transient part (corresponding to the damped natural frequency oscillations) and the steady state part (corresponding to the driving fre-

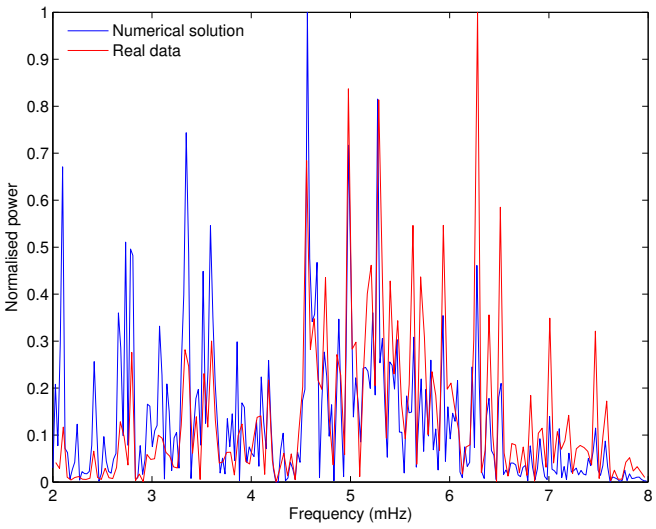

Figure 4.8: Power spectra for the observational data from day 3 and the numerical solution using the 3 and 5 min oscillations from that day as driving oscillations.

quency oscillations) and the strong damping ($k = 1$) was required so that the driving oscillations could be clearly seen. Figure 4.8 shows Fourier power spectra for both the observational data from day 3 and the numerical solution to the equation, using the high frequency oscillations as the driver. Only the high frequency part of the spectrum is shown, since the low frequency natural oscillations were strongly damped. There is a good agreement between the spectra, as is expected. Since there is no nonlinearity in the driver, the system should oscillate at the driving frequencies. However, it appears that some of the lower frequencies in the Δf = 2-8 mHz range have more power in the numerical solution than in the observational data.

The equation was then solved, considering the response of the system to the nonlinear driving (allowing for the appearance of the combined frequencies), but without damping. Since $\omega_0 = 2\pi f_0$ was of order 10^{-3} and to impose that the solution was of order 1, $F(t)$ was multiplied by a scale factor $\gamma = 10^{-12}$ to make both the driving and restoring force terms on the right hand side of equation 4.4 of the same order. With no damping, we have

$$\frac{dv}{dt} = F(t) - \omega_0^2 I \tag{4.6}$$

with ω_0^2 of order 10^{-6}. For I of order 1, $\omega_0^2 I$ is therefore of order 10^{-6} and $F(t)$

must also be of order 10^{-6}. However, since $F(t)$ is of order 10^6 we need

$$\gamma F(t) \sim 10^{-6} \Rightarrow \gamma \sim \frac{10^{-6}}{F(t)} \Rightarrow \gamma \sim \frac{10^{-6}}{10^6} \Rightarrow \gamma \sim 10^{-12}. \tag{4.7}$$

The numerical solution and the corresponding Fourier power spectrum are shown in figure 4.9 and it can be seen that an oscillation at the natural frequency is generated and that there are no peaks at the driving frequencies. To try and rectify this problem, the equation was again considered with no damping, but γ was varied, with values given in table 4.2. The only effect that this had was to increase the amplitude of the solution. In addition, γ was fixed and the damping coefficient was varied (again with values given in table 4.2). Figure 4.10 shows the solution and power spectrum for the case $k = 10^{-3}$ and $\gamma = 10^{-12}$, showing that the natural frequency peak is still present, but its amplitude has decreased. For $k \geq 10^{-3}$, the solution is dominated by a large scale trend, since the damping term means that the natural frequency oscillations are short lived. Since the driving term is always positive, the system is constantly moved away from equilibrium.

4.7 Conclusions

The results of the analysis performed in an attempt to uncover a link between the high and low frequency oscillations have shown, qualitatively, that the mechanism of combining high frequency oscillations in this way can indeed generate the natural frequency oscillations. The proposed model is undoubtedly too simple to account for the observations and as such, the results presented in this chapter demonstrate the need for the long-term study of long period oscillations in sunspots, their possible relationship with 3 min oscillations and theoretical modelling of these oscillations.

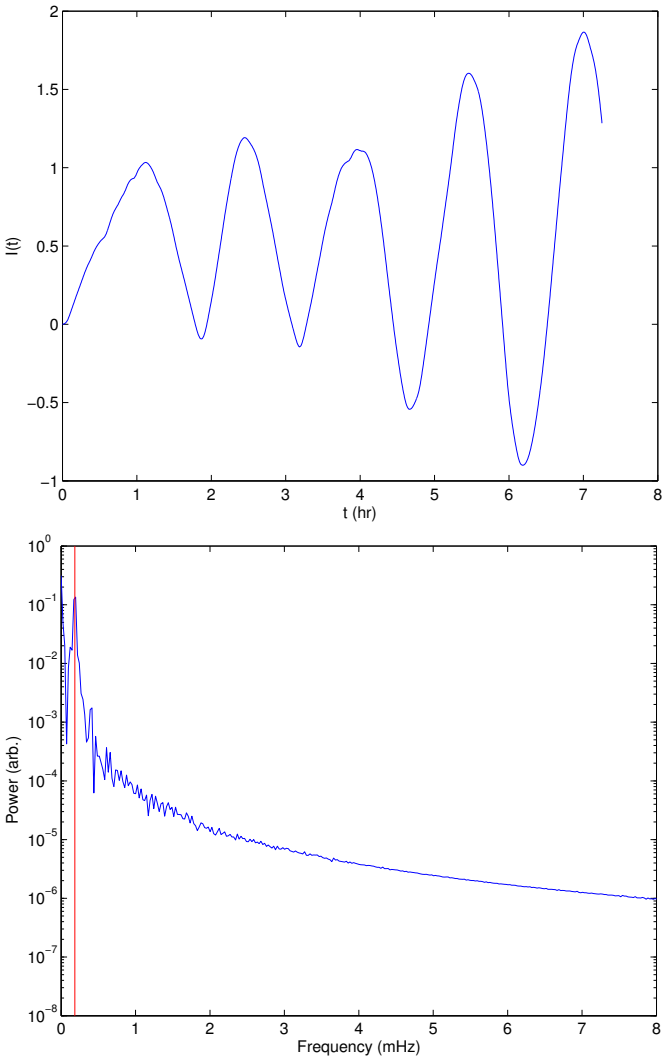

Figure 4.9: The numerical solution of the model equation, with $k = 0$ and $\gamma = 10^{-12}$ (top) and the corresponding power spectrum (bottom). The vertical line in the spectrum marks the natural frequency of the system.

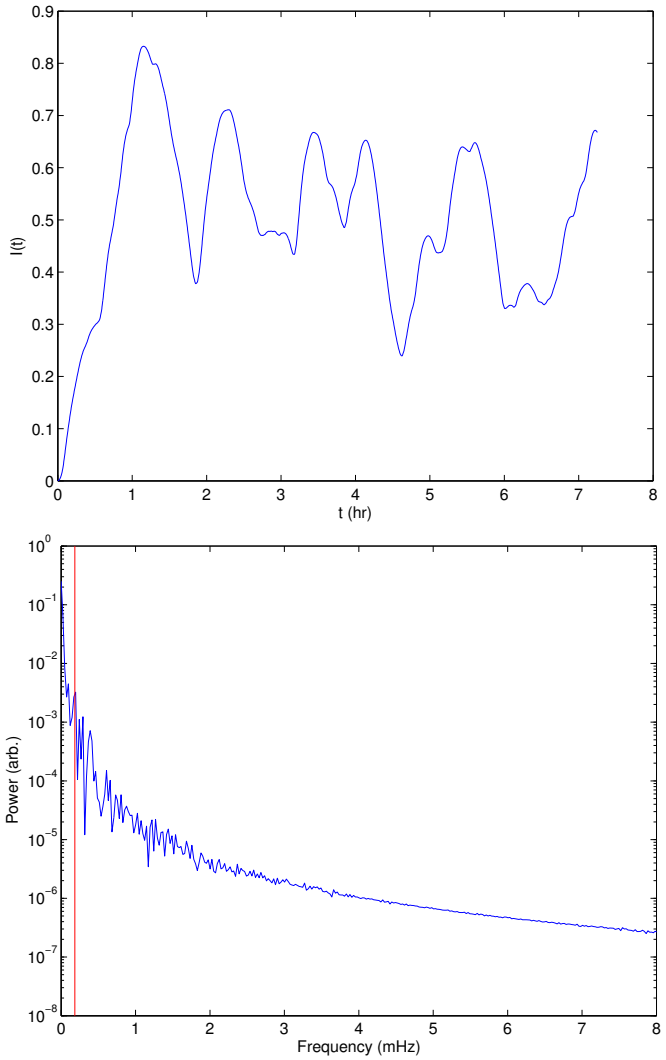

Figure 4.10: The numerical solution of the model equation, with $k = 10^{-3}$ and $\gamma = 10^{-12}$ (top) and the corresponding power spectrum (bottom). The vertical line in the spectrum marks the natural frequency of the system.

Chapter 5

The spatial structure and amplitude modulation of 3 minute oscillations

5.1 Introduction

The three minute chromospheric umbral oscillations are the most studied of all oscillations in sunspots and as was mentioned in section 1.6.3, they are thought to be manifestations of slow magnetoacoustic waves.

While most studies have concentrated on the temporal properties of the three minute oscillations, there have been few studies of their spatial structure. Rüedi et al. (1998) studied oscillations in the 3 and 5 min bands, in the magnetogram and Doppler velocity measurements from sunspot umbrae, observed with SOHO/MDI. They found that the oscillations in velocity were observed across the umbra, but those in the magnetogram were more localised. The authors suggested that the observed distribution of the magnetogram power could be a sign of the non-uniformity of the magnetic field in regions below the photosphere.

Norton et al. (1999) investigated the distribution of spectral power in SOHO/MDI magnetograms, continuum intensity and Doppler velocity observations from a sunspot in the 3, 5 and 20 min bands. Their analysis showed that the distribution of power in the magnetic data differed between the bands. The magnetic and velocity data were found to be 90° out of phase in both the 3 and 5 min bands. If the magnetic data are to be interpreted as indicators of the magnetic field strength, this is suggestive

of a compressible perturbation. Balthasar (1999) also observed oscillations in the magnetic field from a sunspot, using the Göttingen 2D-spectrometer on the Vacuum Tower Telescope. The author generated power maps for various period ranges and showed that for all of them, the power had a maximum in a penumbral pore (see figure 1 of Balthasar 1999). In addition, a ring of enhanced power was seen at the umbra-penumbra boundary.

Microwave observations have also been used to study the spatial distribution of sunspot oscillations. In particular, Nindos et al. (2002) studied spatially resolved oscillations in data from the Very Large Array, operating at frequencies of 5 and 8.5 GHz. The oscillation power peaked at frequencies corresponding to 3 min periods, in both observing frequencies and the distribution of the intensity variations was found to be inhomogeneous. It was suggested that such inhomogeneities may be linked with inhomogeneities in the sunspot atmosphere. Sych & Nakariakov (2008) developed a method known as pixelised wavelet filtering which they used to study oscillations in images of microwave emission above three sunspots observed with NoRH. Sources of 3 and 15 min periodicities were found to be located at the centre of the microwave regions and for one sunspot, the oscillations in each of these two bands were in phase over the region. Two patches of 5 min oscillation were also observed, located at the umbra-penumbra boundary and seen to oscillate in anti-phase with each other. We have seen in chapter 3 above the study of the spatial structure of long period oscillations in the microwave, using the techniques of period and correlation mapping.

Nagashima et al. (2007) used Hinode/SOT to investigate the distribution of spectral amplitude in a sunspot at both photospheric and chromospheric wavelengths. They found that all frequencies were suppressed in the umbra in the G-band but that oscillations were detected in the umbra in Ca II H and the dominant frequency was 5.5 mHz, corresponding to a period of 3 min. Socas-Navarro et al. (2009) also used Hinode/SOT, though their work studied the dynamics of the chromosphere above a sunspot at large, rather than specifically focusing on oscillations. Nonetheless, they observed that the umbra was segmented into small regions known as umbral cores and these had a similar dominant period (again, of about 3 min. See figure 6 of Socas-Navarro et al. 2009). The analyses of Nagashima et al. (2007) and Socas-Navarro et al. (2009) only focused on the spatial distribution of the spectral amplitude; neither group attempted a correlation analysis to determine the spatial coherency of the oscillations.

In this chapter, we again make use of period and correlation mapping to investigate the distribution of oscillation phase of the 3 min oscillations, using Hinode/SOT observations. Doing so may aid our understanding of sunspot structure and to the best of this author's knowledge, a similar study has not been conducted before. The work presented in this chapter therefore presents an original contribution to the field. In addition, we present a simple analysis of the amplitude modulation of the oscillations as a function of radial distance from sunspot centre.

This chapter is structured in the following way: section 5.2 describes the observations, section 5.3 details the analysis (in particular, sections 5.3.2 and 5.3.3 detail the spatial and amplitude modulation analyses, respectively) and in section 5.4, the results are discussed.

5.2 Observations

Two sunspots were observed with Hinode/SOT in Ca II H ($\lambda = 396.85$ nm, chromosphere). The first was the sunspot of AR10930, observed for an interval of about 1 hr, beginning on 14 December 2006 07:13 and ending at 08:12, with a mean cadence of 29.77 s. The other sunspot under consideration was that of AR10988, studied by Socas-Navarro et al. (2009). The observations for AR10988 began on 29 March 2008 at 11:50 and lasted 1 hr 4 min, with a mean cadence of 20 s. For both sunspots, the first image from the datacube is shown in figure 5.1. We restricted the field of view (FOV) as much as possible, in order to minimise the amount of quiet Sun present. The final datacubes were 954 $\times$ 594 pixels for AR10930 and 301 $\times$ 501 pixels for AR10988.

5.3 Analysis

5.3.1 Data preprocessing and preliminary analysis

Before attempting any spatial analysis, we generated time series from the sets of images for both sunspots by taking the mean pixel value for each image. Since we did not want any quiet Sun pixels to contaminate our results, we set thresholds on the maximum sunspot intensities in the first image and thus only computed the mean of the pixels below these thresholds. The thresholds used were: AR10930: 250 DN s^{-1} and AR10988: 1400 DN s^{-1}. There were several bad images in the dataset for AR10988, which appeared as large decreases in intensity in the time

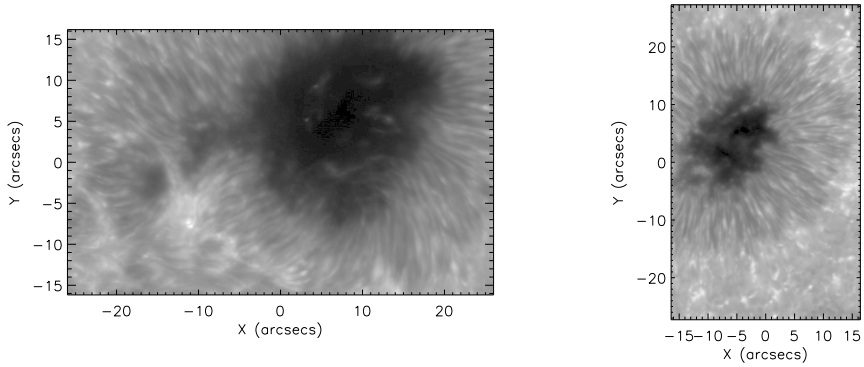

Figure 5.1: The sunspots observed with Hinode/SOT. Left: AR10930, right: AR10988.

series. These decreases were removed by interpolation with cubic splines. The time series are shown in figure 5.2. The large scale trends present were removed by fitting and subtracting a 4th order polynomial and the detrended time series are shown in figure 5.3. We then computed Lomb-Scargle periodograms (Scargle 1982) for the time series. This was repeated for only the umbral pixels, again using thresholds (AR10930: 100 DN s^{-1}, AR10988: 770 DN s^{-1}) to select the relevant pixels. Figure 5.4 shows the periodograms. In the umbral periodograms for both sunspots (black lines), significant peaks around $f \approx 6$ mHz ($P \approx 3$ min) can be seen. In the periodograms for the time series generated by averaging over the entire sunspots (red lines), clear peaks at periods near 5 min ($f \approx 3$ mHz) can be seen. In addition, in the sunspot periodogram for AR10930, a strong peak is seen at a period of approximately 10 min ($f \approx 1.67$ mHz).

5.3.2 Spatial analysis

The datacubes were interpolated so that the time cadence would be regular (30 s for AR10930 and 20 s for AR10988), so that we could use Fourier-based techniques for the subsequent analysis. Since we were only interested in the 3 minute oscillations, the data were then spectrally filtered to keep frequencies in the range f = 5-7 mHz, using a Gaussian function as the filter.

We then computed period and amplitude maps in order to show the distribu-

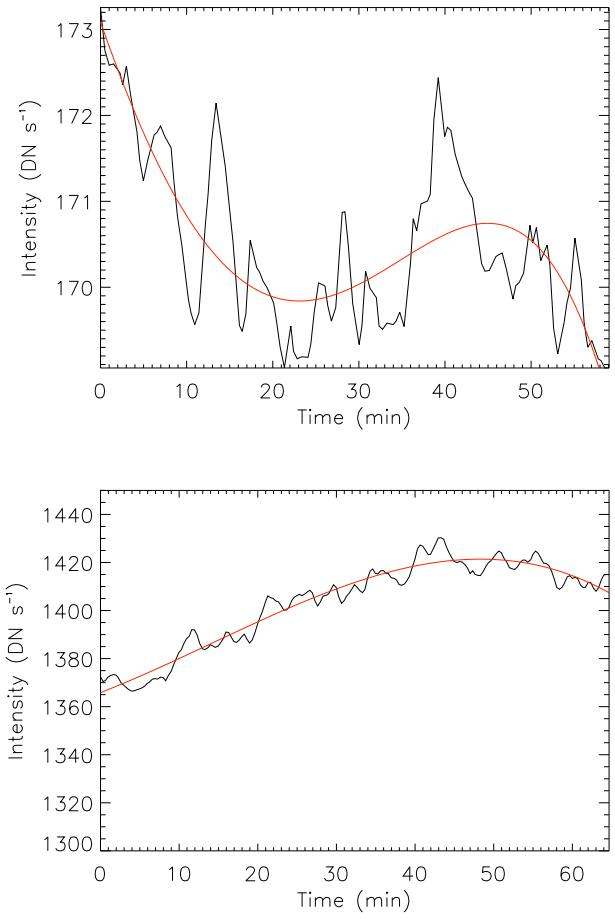

Figure 5.2: The original time series generated from Ca II images from Hinode/SOT for AR10930 (top) and AR10988 (bottom). The red lines show the polynomial fits used for detrending.

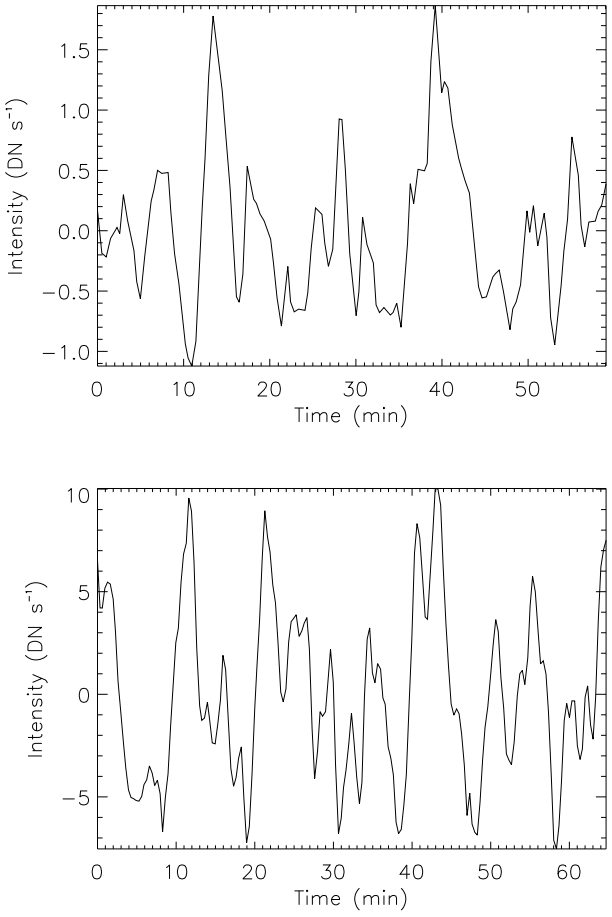

Figure 5.3: The time series used for the periodogram analysis, after trend removal. Top: AR10930, bottom: AR10988.

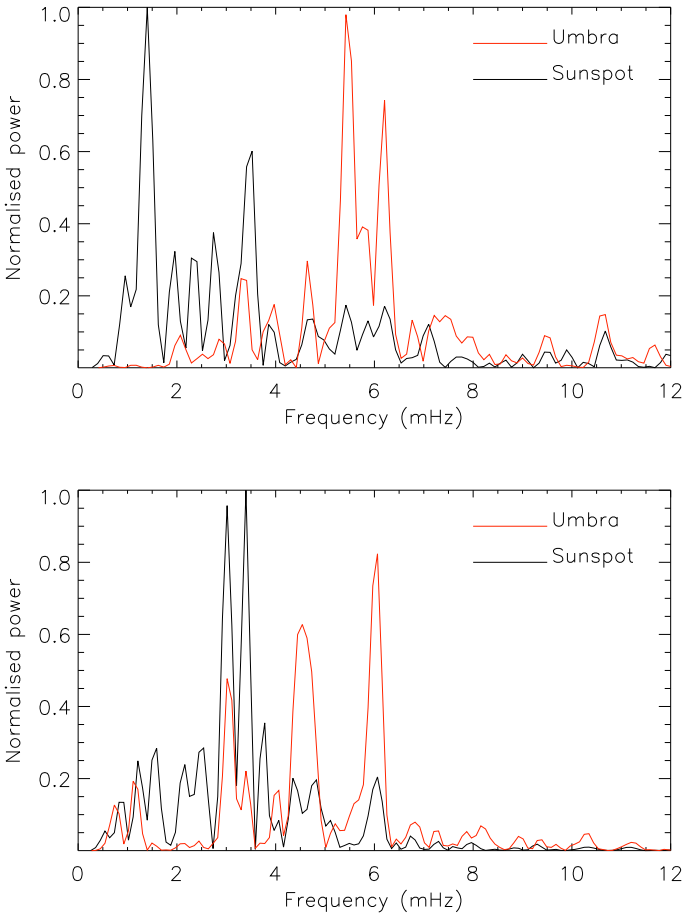

Figure 5.4: The Lomb-Scargle periodograms generated from the spatially integrated time series for AR10930 (top) and AR10988 (bottom). In each plot, the periodograms have been normalised to the maximum amplitude in the sunspot periodogram (AR10930: 14.61 DN^2 s^{-2} Hz^{-1}, AR10988: 22.93 DN^2 s^{-2} Hz^{-1}). Here, "sunspot" means that the signal has been integrated over both the umbra and penumbra.

tion of the dominant frequency and spectral amplitude over the sunspots. Figures 5.5 and 5.6 show the period and amplitude maps for the two sunspots, respectively. The periodmaps show that in both cases, the dominant frequency is near the centre of the prescribed frequency range and that in neither case is it uniform over the umbra. In the amplitude maps, we see that the spectral amplitude is not uniform over the sunspot umbrae either. For AR10930, there is a large region in the umbra where the 3 minute power appears to be suppressed.

Correlation and lag maps (as described in chapter 2 above) were then produced. As in chapter 3, we chose the master pixel for this analysis as the one with the maximum spectral amplitude in the umbra. The maximum correlation was found over the range of lags $[-\frac{1}{2}P, \frac{1}{2}P]$, where $P = 3$ min. The correlation and lag maps are shown in figures 5.7 and 5.8, respectively. The correlation maps show that the umbrae are segmented into regions of high correlation (this is more apparent in the correlation map for AR10988). In the lag maps, the maximum correlation does not occur at the same lag for all pixels. This is akin to saying that the oscillations in each pixel are not in phase and hence we conclude that there is not a strong spatial coherency of the 3 minute oscillations. This is the case for AR10988; for AR10930, the differences in phase between pixels is small.

To test whether the observed spatial properties of the 3 min oscillations were an artefact of processing the data, we employed several tests. These were to vary the filter used to select only the 3 min oscillations, as well as to vary the time interval of the observations under consideration. In addition to the $f = 5$-7 mHz Gaussian bandpass, we used a boxcar function with the same width, as well as narrower ($f =$ 5.5-6.5 mHz) and wider ($f = 4.5$-7.5 mHz) bandpasses. Intervals of 25, 30 and 45 min were used in addition to the original 1 hr interval. Qualitatively, changes in the filter used or the length of the observation interval had little effect on the results of the analysis.

5.3.3 Time-distance plots

To investigate the amplitude modulation of the 3 minute oscillations, using the same filtered data as for the spatial analysis ($f = 5$-7 mHz, with a Gaussian bandpass), we created time-distance plots for various slits across the sunspot of AR10930. We chose three horizontal slits ($y = 250$, 350, 450) and three vertical slits ($x = 450$, 600, 725) and created the time-distance plots for each one. To produce a time-distance plot, one takes the desired slit from the images at a range of times and places them

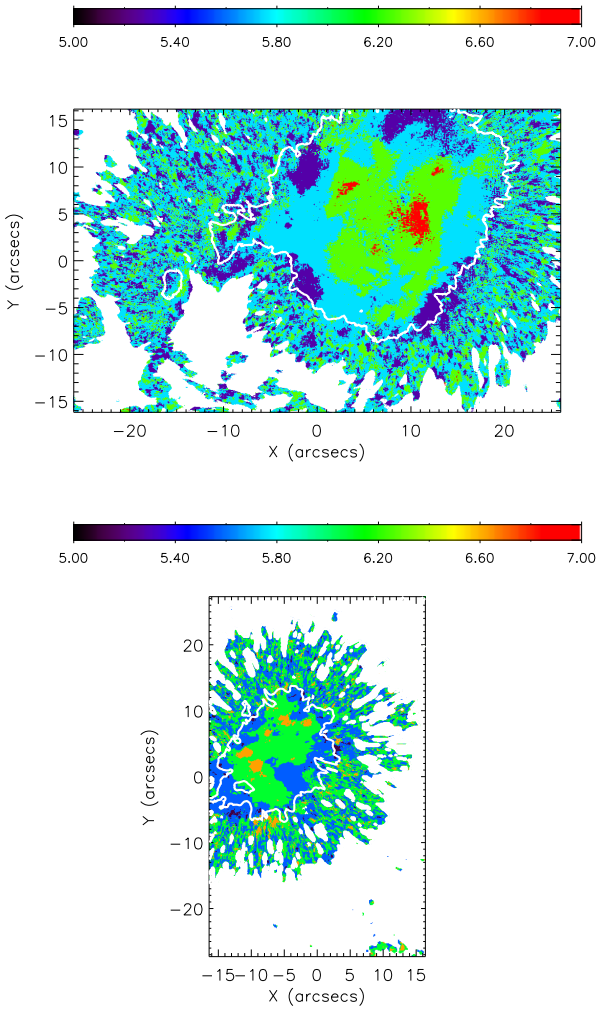

Figure 5.5: The periodmaps after narrowband filtering to keep 3 min oscillations (f = 5-7 mHz). Top: AR10930, bottom: AR10988. Frequencies are displayed in mHz and the inner rings in both plots mark the umbra-penumbra boundary.

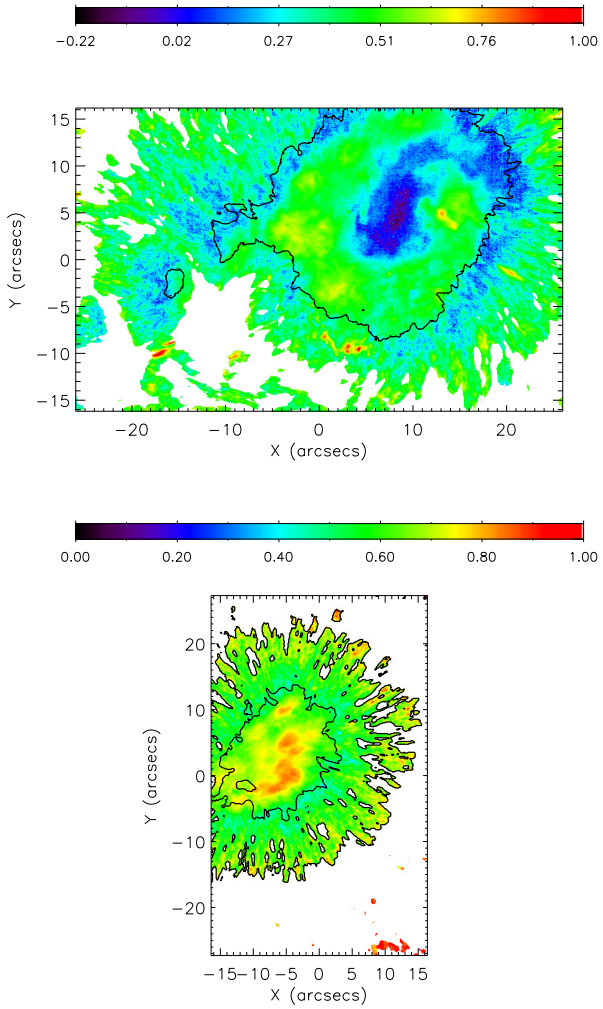

Figure 5.6: The amplitude maps after narrowband filtering to keep 3 min oscillations (f = 5-7 mHz). Top: AR10930, bottom: AR10988. Amplitudes have been normalised to the maximum amplitude in the map and the inner rings in both plots mark the umbra-penumbra boundary.

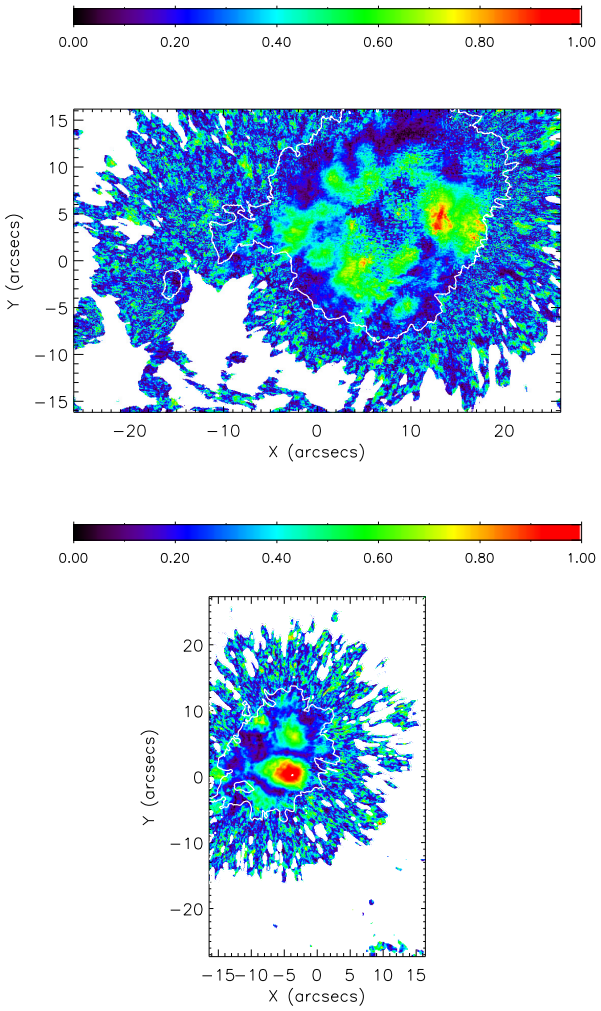

Figure 5.7: The correlation maps after narrowband filtering to keep 3 min oscillations (f = 5-7 mHz). Top: AR10930, bottom: AR10988. The inner rings in both plots mark the umbra-penumbra boundary.

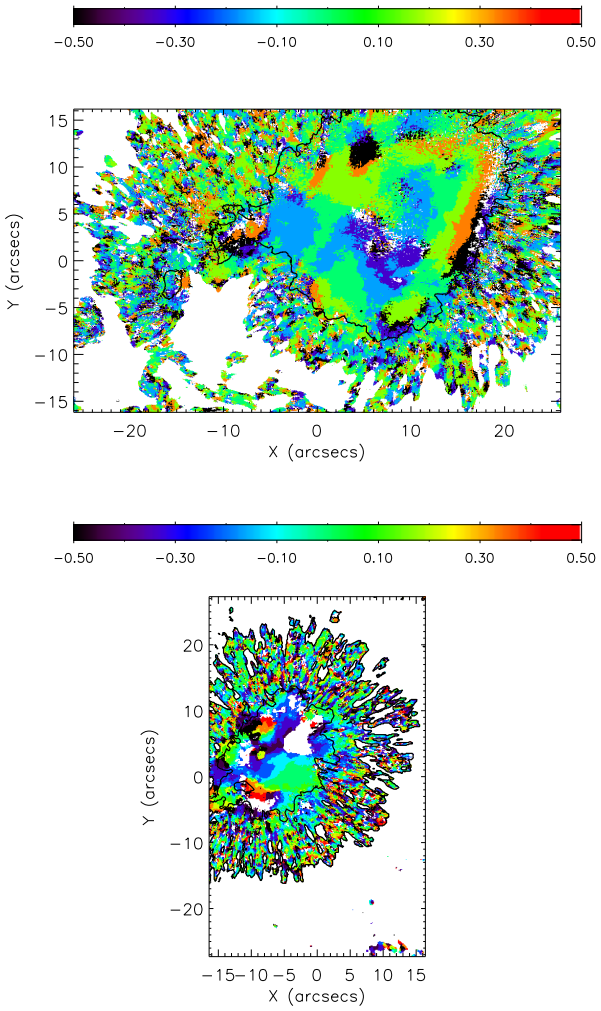

Figure 5.8: The lag maps after narrowband filtering to keep 3 min oscillations (f = 5-7 mHz). Top: AR10930, bottom: AR10988. Lags have been normalised to $P = 3$ min. The inner rings in both plots mark the umbra-penumbra boundary.

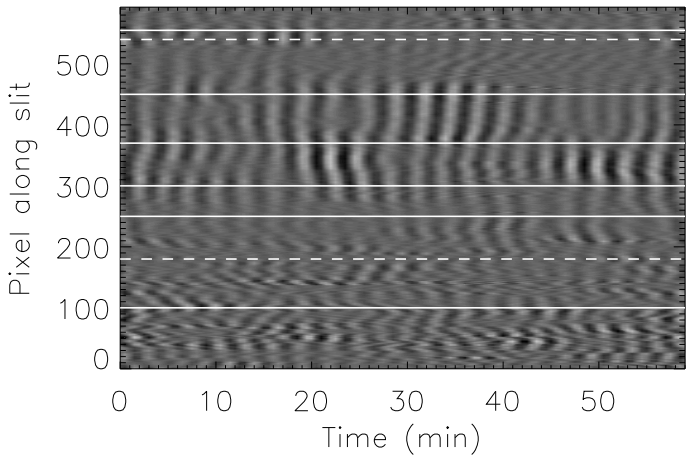

Figure 5.9: Time-distance plot for the 3 min-filtered datacube of AR10930, for the vertical slit at $x = 450$. The dashed lines mark the umbra-penumbra boundary and the solid lines mark the pixels whose time series were investigated for amplitude modulation.

alongside each other. In this way, the evolution of all pixels in the slit can be observed over a given time interval. Figure 5.9 shows an example of a time-distance plot, for the slit placed at pixel $x = 450$. In this slit, the 3 min oscillations are seen to be clearly visible over about 200 pixels (from $y = 300$ to $y = 500$), corresponding to a distance of about 7.85 Mm. Towards the edges of the umbra, the amplitude of the oscillations is seen to have decreased substantially. Outside the umbra and towards the bottom of the slit (pixels $y = 0$-100), the oscillations are not seen to be as coherent along the slit as they are inside the umbra.

For various pixels along each slit (such as those indicated in figure 5.9), the time series were plotted to determine whether there was a periodic amplitude modulating component. To determine the dominant period of the amplitude modulation, we extracted the envelope from the signal in the following way. Assume we have an amplitude modulated signal,

$$I(t) = a(t) \cos \omega t, \tag{5.1}$$

we can construct the "analytic associate" of $I(t)$,

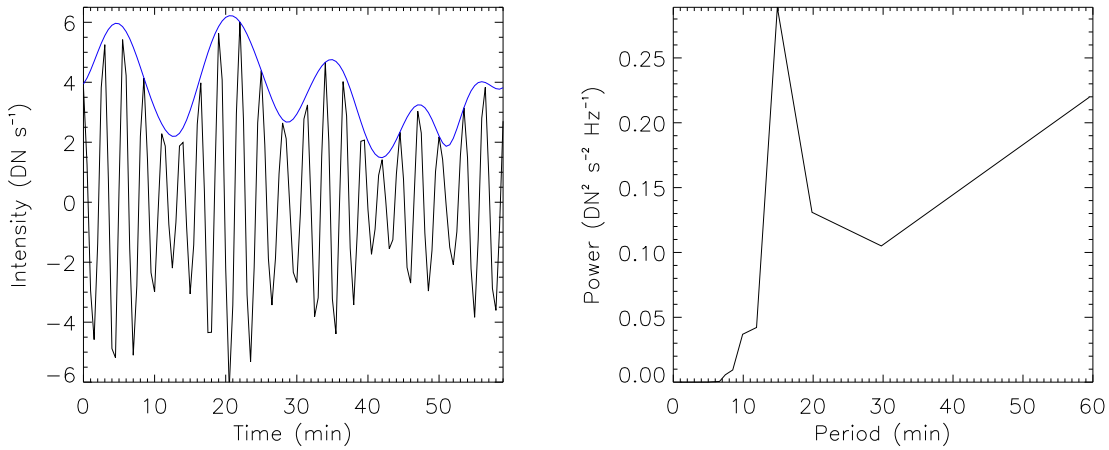

Figure 5.10: Left: the time series from pixel $y = 370$ in the time-distance plot shown in figure 5.9. The blue curve shows the envelope function determined using the Hilbert transform. Right: the power spectrum of the envelope function shown in the left panel.

$$z(t) = I(t) + i\mathcal{H}\left[I(t)\right], \tag{5.2}$$

where $\mathcal{H}\left[I(t)\right]$ is the Hilbert transform of $I(t)$, as described in section 2.1.4. The computation of $\mathcal{H}\left[I(t)\right]$ involves computing the Fourier transform of $I(t)$, phase shifting every component of the Fourier transform by $\frac{\pi}{2}$ and then computing the inverse transform. Taking the magnitude of $z(t)$ gives

$$\begin{aligned} |z(t)| &= \sqrt{I^2(t) + \mathcal{H}^2\left[I(t)\right]} \\ &= \sqrt{a^2(t)\cos^2\omega t + a^2(t)\sin^2\omega t} \\ &= a(t), \end{aligned} \tag{5.3}$$

where $\sin\omega t$ is the Hilbert transform of $\cos\omega t$, because the transform introduces a phase shift of $\frac{\pi}{2}$ for periodic signals. In addition, the Hilbert transform of $a(t)\cos\omega t$ is $a(t)\sin\omega t$ only if the variation of $a(t)$ occurs on a timescale much longer than that of $\cos\omega t$ (see, e.g. Boashash 2003). Once the envelope had been found, we computed its power spectrum and found the period of the dominant peak. Figure 5.10 shows

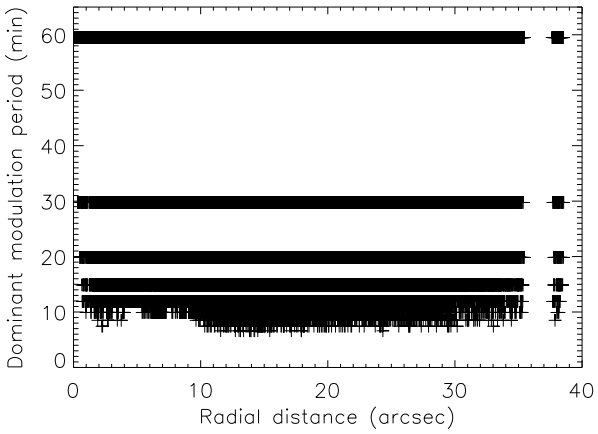

Figure 5.11: The dominant period of amplitude modulation as a function of radial distance from the centre of the sunspot of AR10930.

the time series from the pixel at $x = 450$ and $y = 370$, along with the envelope function computed using the Hilbert transform and its corresponding power spectrum. The envelope found in this way is seen to provide a good agreement with the envelope of the signal and the power spectrum for this example gave a modulation period of $P = 14.88$ min.

We then decided to investigate the dependence of the dominant modulation period on radial distance from the sunspot centre. The signals from all sunspot pixels were studied and these were selected by using the same threshold on maximum intensity as used in section 5.3.1. There were 430,498 pixels in total and figure 5.11 shows the dominant modulation period plotted against radial distance from the sunspot centre. It can be seen that there are several bands of constant modulation period, at approximately $P = 15$, 20, 30 and 60 min. In addition, we investigated the distribution of the dominant modulation periods. Since the Fourier transforms of the pixel time series were discrete, peaks could only appear at multiples of the frequency resolution, $df = 0.28$ mHz. Figure 5.12 shows the distribution of the dominant modulation frequency, normalised to df. The distribution has a peak at $2df$, corresponding to a period of $P = 29.75$ min.

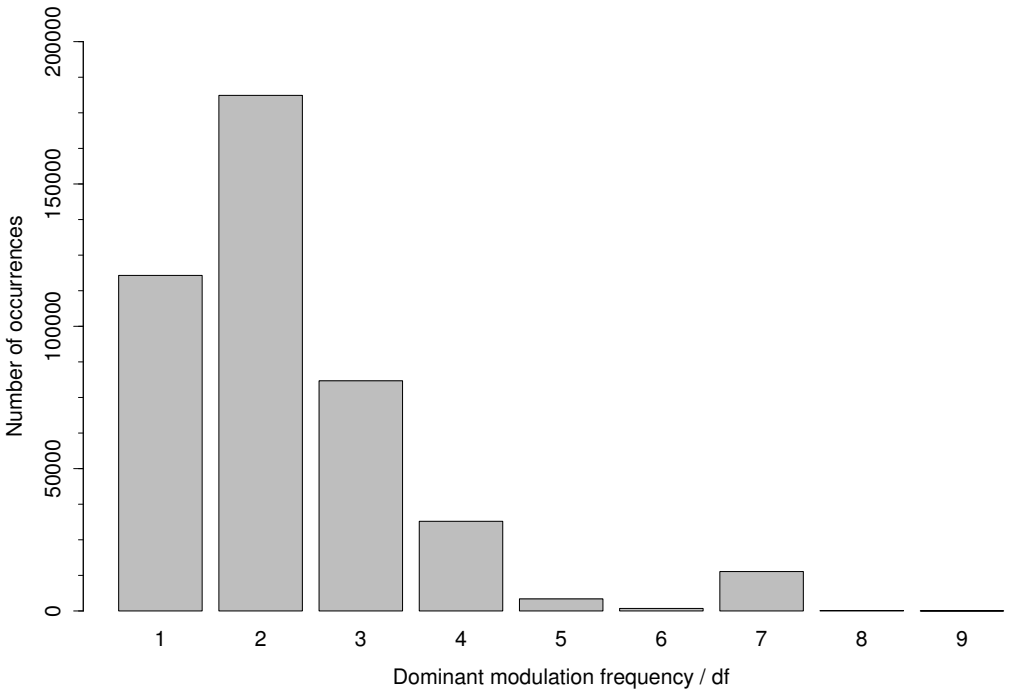

Figure 5.12: The distribution of dominant amplitude modulation frequency of the 3 minute oscillations for all pixels in the sunspot of AR10930. The frequencies have been normalised to the frequency resolution of the Fourier power spectrum, df = 0.28 mHz.

5.4 Discussion

In this chapter, we have analysed the spatial structure of 3 minute oscillations in two sunspots observed with Hinode/SOT for time intervals of about 1 hour. In addition, we have attempted an investigation of the amplitude modulation of those oscillations. The main findings of this study are as follows:

1. The distribution of spectral amplitude is not uniform over the sunspot umbrae. In AR10930, there is a large region of about $5''\times\ 8''$ in the umbra, in which the 3 min power is suppressed. In AR10988, the region of highest power lies in the central part of the umbra and is about $4''\times\ 9''$.

2. The maximum correlation is also not seen to be uniform over the umbrae.

Instead, small regions of high correlation ($C_{xy} \geq 0.6$) are seen.

3. The lags at which the maximum correlation values occur indicate that the 3 minute oscillations are slightly out of phase over the entire umbra for AR10930. For AR10988, regions oscillating in anti-phase with the master pixel are seen.

4. Several bands of constant modulation period with radial distance are seen, at periods of $P = 15$, 20, 30 and 60 min and the distribution of the dominant modulation periods has a peak at about 30 min.

The results showing that the 3 minute oscillations are not entirely in phase over the entire sunspot umbrae may be an indication of the inhomogeneity of physical quantities (e.g. density and magnetic field strength) in the structure. Measuring the speeds of the waves (with, e.g. observations in different wavelengths) may shed some light on this, since the 3 min oscillations are thought to be slow magnetoacoustic waves. In AR10988, larger phase shifts were seen than in AR10930. This could be artificial, as the data did contain bad images (and these were responsible for drops in mean intensity seen in the spatially integrated signal).

With regards to the amplitude modulation, the presence of several modulation periods independent of radial distance may provide some clue as to the nature of the modulating phenomenon. In addition, the fact that several of these periods are multiples of a common one may suggest the presence of harmonics of an oscillation.

Amplitude modulation can be produced by the superposition of two oscillations, either at close frequencies or ones that are far apart. Consider the signal

$$x(t) = \cos \omega_1 t + \cos \omega_2 t, \tag{5.4}$$

which can be rewritten as

$$x(t) = 2 \cos \left[\frac{(\omega_1 + \omega_2)t}{2} \right] \cos \left[\frac{(\omega_1 - \omega_2)t}{2} \right]. \tag{5.5}$$

In the case of two close frequencies, the difference between ω_1 and ω_2 is small and thus the second cosine in equation 5.5 provides the envelope of the modulation. Figure 5.13 shows the amplitude modulation produced by superposing two oscillations of two close frequencies and that resulting from two frequencies that are far apart.

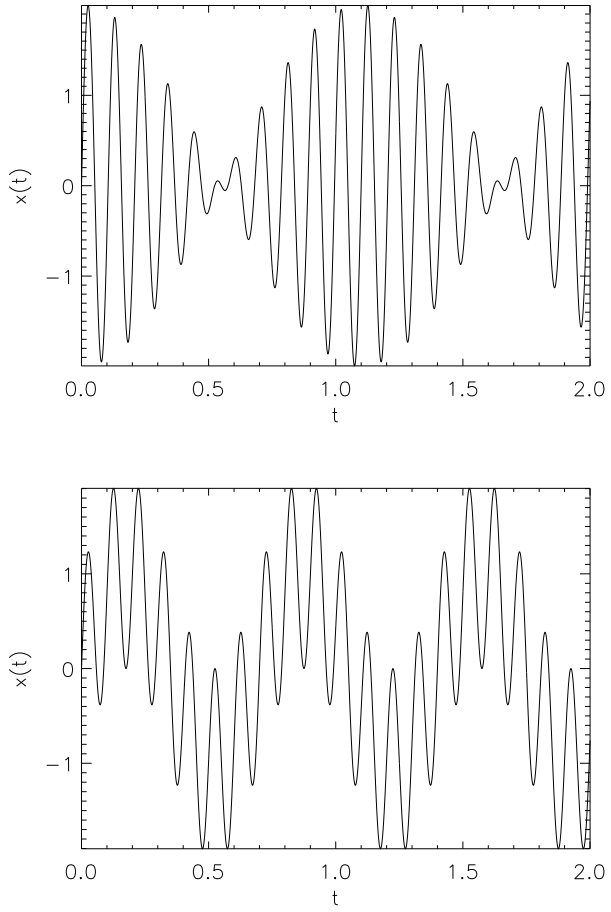

Figure 5.13: Amplitude modulation produced by the superposition of oscillations with two close frequencies, $\omega = \frac{2\pi}{T}$ (top) and two distant ones (bottom). The periods of the two oscillations used for the top panel were $T_1 = 0.1$ and $T_2 = 0.11$, while for the bottom, they were $T_1 = 0.1$ and $T_2 = 0.7$.

Chapter 6

Summary

The work in this thesis presents three original contributions to the field of observations of oscillations in sunspots. The first two of these add to the observational evidence for the presence of long period oscillations in sunspots, while the third contributes to our understanding of the 3 minute oscillations.

In chapter 3, long period oscillations in three sunspots were analysed in both time and space, using images from the Nobeyama Radioheliograph. The techniques of periodogram and wavelet analysis, coupled with significance testing allowed the detection of two long period spectral peaks for each sunspot under study, with periods in the range $P \approx$ 16-88 min. A relatively unused technique in the field of solar oscillations, empirical mode decomposition, was then used to remove the trend present in the time series and this combined with wavelet analysis confirmed that the presence of the long period oscillations was not due to an artefact of removing the trend by polynomial fitting. Spatial analysis was performed on the sets of images for two of the three sunspots studied, using the techniques of period and correlation mapping. The results of this analysis showed that the oscillation power was mainly concentrated over the umbral regions and that there were two regions of roughly equal size, that oscillated in anti-phase with each other.

In addition, long period oscillations in a single sunspot were studied in microwave and optical wavelengths, with NoRH and Hinode/SOT, respectively. Periods of 80 and 91 min were revealed in the time series from the optical data, but unfortunately, we could not prove the physical nature of these periodicities as they were close to the orbital period of the spacecraft. A period of 128 min was detected in the microwave intensity and we are not able to infer a link between the

periodicities in different parts of the atmosphere.

It was suggested that the long period oscillations could be related to the solar g-modes, which may leak from the solar interior. However, it is known that such waves have not been detected yet and we infer a link with the long period sunspot oscillations based solely on the predicted periods. Another candidate for the observed oscillations is the global natural oscillations of a shallow sunspot, proposed by Solov'ev & Kirichek (2008). The results of the spatial analysis may be an indication of the raft-like nature of the structure that oscillates due to being constantly struck by waves in the surrounding medium.

Chapter 4 extended the temporal part of the study presented in chapter 3, by studying the long period oscillations over a period of 9 days, again using NoRH. Periods in the range $P = 50$-120 min were found to be present in the signals for all 9 days, suggesting that such oscillations are long-lived. The spectral amplitudes for 5 Fourier components in the given period range were also seen to be stable over the observations, when no large flares were present in the signals. Unfortunately, the phases for the same 5 Fourier components showed no such stability.

To explain the persistence of the long period oscillations, a model was proposed, in which the system was a damped simple harmonic oscillator with a non-linear driving term. The motivation for this came from two properties of the 3 min oscillations: their persistence and that the spectrum is a cluster of peaks, which are separated by frequency differences corresponding to the observed long periods. In an attempt to investigate this mechanism, the distribution of frequency differences in the 3 and 5 min part of the spectrum was analysed for each day and the periods corresponding to the peak frequency difference were plotted against the corresponding dominant periods. There appeared to be no correlation between the two quantities and so this analysis was inconclusive. The equation describing the proposed model was solved numerically, using realistic driving oscillations. That is, amplitudes, frequencies and phases for the driving oscillations were taken from the Fourier transform of one of the 9 time series. While oscillations at the natural frequency of the system were generated, the spectrum of the numerical solution was devoid of the driving frequency oscillations. Due to time constraints, it was not possible to determine the cause of this issue.

In chapter 5, the focus shifted from long period oscillations to the 3 min oscillations. Using high resolution images from Hinode/SOT, the spatial structure of the short period oscillations was studied in two sunspots, by making use of the

same techniques used for spatial analysis in chapter 3. The results showed that the distribution of spectral power was not uniform across the sunspot umbrae and a correlation mapping analysis showed further that the entire umbrae did not oscillate in phase at the 3 min period. A possible reason for this was suggested to be the inhomogeneity of the plasma in the structure, but more detailed observations (of, e.g. magnetic field strength) are required to test this. Finally, a simple analysis of the amplitude modulation of the 3 min oscillations was presented for one sunspot, in terms of the relationship between modulation period and radial distance from the sunspot centre. This analysis showed the presence of several periods that were independent of radial distance, several of which were multiples of a fundamental period, possibly suggesting the presence of harmonics. Finally, the distribution of the modulation periods had a peak at around 30 min, but it was not clear how this value arose.

There are various open questions relating to the work presented in this thesis. With regards to the long period oscillations, it is still not clear how they are generated, or what link there is (if any) between such oscillations and the 3 min oscillations. Concerning the spatial structure of the long period oscillations studied in chapter 3, we have only studied a small number of sunspots and therefore do not know what the typical behaviour is. As such, an important study to be undertaken would be that of the spatial structure of long period oscillations in the microwave emission above a large sample of sunspots. Further, the detailed study of the variation of the spatial structure of long period oscillations with height has not been attempted. Such a study can now be performed with the recently launched Solar Dynamics Observatory (SDO) and a comparative study of such oscillations with both SDO and NoRH may be able to localise the height of the microwave emission. The study of the lifetimes of long period oscillations presented in chapter 4 was limited in usefulness by the long data gaps due to the ground-based nature of NoRH. If we are to use such oscillations to track changes in the sunspots and their associated active regions, as well as for forecasting of flares, it would be preferable to have continuous observations for as long as possible. Again, with SDO, such a study is now a possibility.

The theoretical work on long period oscillations has not been further developed. A study that could aid in the development of this field would be to consider the response of a shallow sunspot structure to perturbations by the high frequency waves present in the surrounding plasma. The idea would be to investigate the

kinds of global oscillations of the structure that were induced, to determine whether low frequency modes were produced. In addition, perhaps a "forward modelling" analysis could be attempted, to determine (for example) the expected structure of the microwave emission in the sunspot atmosphere.

Bibliography

Appourchaux, T., Belkacem, K., Broomhall, A.-M., et al. 2010, A&AR, 18, 197

Aschwanden, M. J. 2009, Physics of the Solar Corona: An introduction with problems and solutions (Praxis)

Balthasar, H. 1999, Sol. Phys., 187, 389

Beckers, J. M. & Tallant, P. E. 1969, Sol. Phys., 7, 351

Berton, R. & Rayrole, J. 1985, A&A, 152, 219

Bhatnagar, A. & Tanaka, K. 1972, Sol. Phys., 24, 87

Boashash, B., ed. 2003, Time frequency signal analysis and processing: a comprehensive reference, 1st edn. (Elsevier Science)

Bogdan, T. J. 2000, Sol. Phys., 192, 373

Bogdan, T. J. & Judge, P. G. 2006, Phil. Trans. R. Soc. A, 364, 313

Botha, G. J. J., Arber, T. D., Nakariakov, V. M., & Zhugzhda, Y. D. 2011, ApJ, 728, 84

Braun, D. C., Duvall, T. L., & LaBonte, B. J. 1987, ApJ, 319, L27

Brynildsen, N., Kjeldseth-Moe, O., & Maltby, P. 1999a, ApJ, 517, L159

Brynildsen, N., Leifsen, T., Kjeldseth-Moe, O., Maltby, P., & Wilhelm, K. 1999b, ApJ, 511, L121

Centeno, R., Collados, M., & Trujillo Bueno, J. 2006, ApJ, 640, 1153

De Moortel, I., Ireland, J., Hood, A. W., & Walsh, R. W. 2002, A&A, 387, L13

Druzhinin, S. A., Pevtsov, A. A., Levkovsky, V. L., & Nikonova, M. V. 1993, A&A, 277, 242

Edwin, P. M. & Roberts, B. 1983, Sol. Phys., 88, 179

Efremov, V. I., Parfinenko, L. D., & Solov'ev, A. A. 2007, Ast. Rep., 51, 401

Efremov, V. I., Parfinenko, L. D., & Solov'ev, A. A. 2009, Cosmic Research, 47, 279

Efremov, V. I., Parfinenko, L. D., & Solov'ev, A. A. 2010, Sol. Phys., 267, 279

Felipe, T., Khomenko, E., Collados, M., & Beck, C. 2010, ApJ, 722, 131

Ferraz-Mello, S. 1981, AJ, 86, 619

Foullon, C., Verwichte, E., & Nakariakov, V. M. 2004, A&A, 427, L5

Foullon, C., Verwichte, E., & Nakariakov, V. M. 2009, ApJ, 700, 1658

García, R. A., Jiménez, A., Mathur, S., et al. 2008, Astron. Nachr., 329, 476

Gary, G. A. 2001, Sol. Phys., 203, 71

Gelfreikh, G. B., Grechnev, V., Kosugi, T., & Shibasaki, K. 1999, Sol. Phys., 185, 177

Gelfreikh, G. B., Nagovitsyn, Y. A., & Nagovitsyna, E. Y. 2006, PASJ, 58, 29

Giovanelli, R. G. 1972, Sol. Phys., 27, 71

Gizon, L., Birch, A. C., & Spruit, H. C. 2010, Ann. Rev. Astro. Astrophys., 48, 289

Goldvarg, T. B., Nagovitsyn, Y. A., & Solov'ev, A. A. 2005, Ast. Lett., 31, 414

Gonzalez, R. C. & Woods, R. E. 2008, Digital Image Processing, 3rd edn. (Pearson Prentice Hall)

Goossens, M. 2003, An Introduction to Plasma Astrophysics and Magnetohydrodynamics (Kluwer)

Gopasyuk, O. S. 2004, in Multi-Wavelength Investigations of Solar Activity, Vol. 223, 249

Groth, E. J. 1975, ApJS, 29, 285

Högbom, J. A. 1974, A&AS, 15, 417

Horne, J. H. & Baliunas, S. L. 1986, ApJ, 302, 757

Huang, N. E., Shen, Z., Long, S. R., et al. 1998, Proc. R. Soc. Lond. A, 454, 903

Inglis, A. R., Nakariakov, V. M., & Melnikov, V. F. 2008, A&A, 487, 1147

Khomenko, E. & Collados, M. 2006, ApJ, 653, 739

Khomenko, E., Kosovichev, A., Collados, M., Parchevsky, K., & Olshevsky, V. 2009, ApJ, 694, 411

King, D. B., Nakariakov, V. M., Deluca, E. E., Golub, L., & McClements, K. G. 2003, A&A, 404, L1

Kobanov, N. I., Kolobov, D. Y., Chupin, S. A., & Nakariakov, V. M. 2011, A&A, 525, A41

Kobanov, N. I. & Makarchik, D. V. 2004, A&A, 424, 671

Kobrin, M. M. & Korshunov, A. I. 1972, Sol. Phys., 25, 339

Kochhar, R. K. 1991, Journal of the British Astronomical Association, 101, 95

Komm, R. W., Hill, F., & Howe, R. 2001, ApJ, 558, 428

Kopp, G. & Rabin, D. 1992, Sol. Phys., 141, 253

Koshiishi, H. 2003, A&A, 412, 893

Leka, K. D. & Skumanich, A. 1998, ApJ, 507, 454

Linnell Nemec, A. F. & Nemec, J. M. 1985, AJ, 90, 2317

McIntosh, P. S. 1990, Sol. Phys., 125, 251

Nagashima, K., Sekii, T., Kosovichev, A. G., et al. 2007, PASJ, 59, 631

Nagovitsyna, E. Y. & Nagovitsyn, Y. A. 2001, Ast. Lett., 27, 118

Nagovitsyna, E. Y. & Nagovitsyn, Y. A. 2002, Ast. Lett., 28, 121

Nakajima, H., Nishio, M., Enome, S., et al. 1994, IEEE Proceedings, 82, 705

Nakariakov, V. M., Inglis, A. R., Zimovets, I. V., et al. 2010, Plasma Physics and Controlled Fusion, 52, 124009

Nakariakov, V. M. & King, D. B. 2007, Sol. Phys., 241, 397

Nakariakov, V. M. & Ofman, L. 2001, A&A, 372, L53

Nakariakov, V. M. & Verwichte, E. 2005, Living Reviews in Solar Physics, 2

Nindos, A., Alissandrakis, C. E., Gelfreikh, G. B., Bogod, V. M., & Gontikakis, C. 2002, A&A, 386, 658

Norton, A. A., Ulrich, R. K., Bush, R. I., & Tarbell, T. D. 1999, ApJ, 518, L123

Otsu, N. 1979, IEEE Trans. Sys., Man., Cyber., 9, 62

Parchevsky, K. V. & Kosovichev, A. G. 2007, ApJ, 666, L53

Parker, E. N. 1975, Sol. Phys., 40, 291

Petrovay, K. & van Driel-Gesztelyi, L. 1997, Sol. Phys., 176, 249

Priest, E. R. 1982, Solar Magneto-hydrodynamics (Kluwer)

Robbrecht, E., Verwichte, E., Berghmans, D., et al. 2001, A&A, 370, 591

Rouppe van der Voort, L. H. M., Rutten, R. J., Sütterlin, P., Sloover, P. J., & Krijger, J. M. 2003, A&A, 403, 277

Rüedi, I., Solanki, S. K., Stenflo, J. O., Tarbell, T., & Scherrer, P. H. 1998, A&A, 335, L97

Sainz Dalda, A. & Martínez Pillet, V. 2005, ApJ, 632, 1176

Scargle, J. D. 1982, ApJ, 263, 835

Schlichenmaier, R., Rezaei, R., Bello González, N., & Waldmann, T. A. 2010, A&A, 512, L1

Schlichenmaier, R. & Schmidt, W. 2000, A&A, 358, 1122

Shibasaki, K. 2001, ApJ, 550, 1113

Shibasaki, K., Enome, S., Nakajima, H., et al. 1994, PASJ, 46, L17

Socas-Navarro, H., McIntosh, S. W., Centeno, R., de Wijn, A. G., & Lites, B. W. 2009, ApJ, 696, 1683

Solanki, S. K. 2003, Astron. Astrophys. Rev., 11, 153

Solov'ev, A. A. & Kirichek, E. A. 2008, Astrophysical Bulletin, 63, 169

Spruit, H. C. 1974, Sol. Phys., 34, 277

Spruit, H. C. & Bogdan, T. J. 1992, ApJ, 391, L109

Steer, D. G., Dewdney, P. E., & Ito, M. R. 1984, A&A, 137, 159

Strassmeier, K. G. 2009, Astron. Astrophys. Rev., 17, 251

Sych, R., Nakariakov, V. M., Karlicky, M., & Anfinogentov, S. 2009, A&A, 505, 791

Sych, R. A. & Nakariakov, V. M. 2008, Sol. Phys., 248, 395

Terradas, J., Oliver, R., & Ballester, J. L. 2004, ApJ, 614, 435

Thomas, J. H., Cram, L. E., & Nye, A. H. 1984, ApJ, 285, 368

Thomas, J. H. & Weiss, N. O. 2008, Sunspots and Starspots (Cambridge University Press)

Title, A. M., Frank, Z. A., Shine, R. A., et al. 1993, ApJ, 403, 780

Torrence, C. & Compo, G. P. 1998, Bull. Amer. Meteorolog. Soc., 79, 61

Tsuneta, S., Ichimoto, K., Katsukawa, Y., et al. 2008, Sol. Phys., 249, 167

Van Doorsselaere, T., Brady, C. S., Verwichte, E., & Nakariakov, V. M. 2008, A&A, 491, L9

Verwichte, E., Foullon, C., & Van Doorsselaere, T. 2010, ApJ, 717, 458

Vourlidas, A., Gray, D. E., & Shibasaki, K. 2006, PASJ, 58, 11

Vrabec, D. 1974, in IAU Symp., Vol. 56, Chromospheric Fine Structure, ed. R. G. Athay

Wang, T. J., Ofman, L., Davila, J. M., & Mariska, J. T. 2009, A&A, 503, L25

Weiss, N. O., Thomas, J. H., Brummell, N. H., & Tobias, S. M. 2004, ApJ, 600, 1073

Westendorp Plaza, C., del Toro Iniesta, J. C., Ruiz Cobo, B., et al. 1997, Nature, 389, 47

White, S. M. & Kundu, M. R. 1997, Sol. Phys., 174, 31

Zhang, J., Solanki, S. K., Woch, J., & Wang, J. 2007, A&A, 471, 1035

Zhao, J., Kosovichev, A. G., & Duvall, T. L. 2001, ApJ, 557, 384

Zhugzhda, Y. D. 2008, Sol. Phys., 251, 501

Zirin, H. & Stein, A. 1972, ApJ, 178, L85

Zwaan, C. 1978, Sol. Phys., 60, 213